

School of Earth and Planetary Sciences

Numerical and Theoretical Modelling of the
Chemo-Mechanical Responses of Solid Solutions

Santiago Peña Clavijo

This thesis is presented for the Degree of
Doctor of Philosophy
of
Curtin University

October, 2019

Declaration

To the best of my knowledge and belief, this thesis contains no material previously published by any other person except where due acknowledgment has been made.

This thesis contains no material, which has been accepted for the award of any other degree or diploma in any university.

Signature:

A handwritten signature in black ink that reads "Santiago P". The name "Santiago" is written in a cursive style, and the letter "P" is a large, stylized capital letter.

Date: 30/10/2019

Acknowledgment

This project was carried out at the School of Earth and Planetary Sciences. This research is supported by a Curtin International Postgraduate Research Scholarship (CIPRS).

I would like to express my sincerest gratitude to my supervisor, Professor Victor Calo, for his continuous guidance and support.

I would like to thank Professors Andrew Putnis and Bruce Hobbs for taking the time and effort to teach me how to think about problems in geoscience.

Special thanks to Dr Luis Espath. He taught me how to think about problems and spent countless hours doing so.

I would like to extend my appreciation to my colleagues, Quanling Deng, Roberto Cier, and Sergio Rojas for their continuous support.

Finally, I would like to thank Kelly Peña Carrasquilla – Mella – for being a source of inspiration and for teaching me never to give up.

Numerical and Theoretical Modelling of the Chemo-Mechanical Responses of Solid Solutions

Santiago Peña Clavijo

Abstract

Complex physical and chemical processes rule the evolution of solid solutions. Both high temperature and pressure allow for solid diffusion and chemical reactions between chemical constituents, which in turn, lead to phase transformations and induced deformation. The description and understanding of the physical and chemical responses of a solid solution under different conditions of temperature and pressure is an important challenge for several disciplines concerned with the solid state such as metallurgy, materials science, and Earth science. For instance, solid solutions in geomaterials are mineral solid solutions. Most importantly, coupled chemo-mechanical interactions rule the evolution of the mineral solid solution. Nonetheless, such an effort requires a comprehensive treatment that characterises the dynamic behaviour of the coupled chemo-mechanical interactions as the solution evolves. The purpose of this thesis is to derive a continuum theory for multicomponent systems undergoing mass transport, chemical reactions, deformation, and interfacial effects from a thermodynamic point of view in order to describe solid solutions. The theoretical foundations of the model rely on modern continuum mechanics, thermodynamics far from equilibrium, and phase-field models. To obtain a complete description of the evolution process, we derive a set of balance equations in the form of partial differential equations. These equations describe how mass, linear and angular momenta, internal energy and entropy vary in time as deformation and chemical processes take place. Using robust numerical procedures, we solve the resulting set of coupled chemo-mechanical equations and verify the underlying physics for the physical and chemical responses of solid solutions.

Contents

1	Introduction	13
1.1	Evidence and modelling of chemo-mechanical responses in mineral solid solutions	15
2	Phase field models	18
2.1	Introduction	18
2.2	The Cahn-Hilliard equation	19
2.2.1	Mathematical derivation	20
2.2.2	Physical derivation	21
3	Modelling the chemo-mechanical responses of mineral solids solutions far from equilibrium under heterogeneous stresses	25
3.1	Introduction	26
3.2	Interfacial interactions: The Ostwald ripening and Gibbs-Thomson effects	28
3.3	Crystalline structure and mass constraint	30
3.4	Elastic energy	31
3.5	Chemical energy	33
3.6	Helmholtz free energy, fundamental balance equations and thermodynamic pressure	35
4	Derivation of a multicomponent reactive Cahn-Hilliard equation	38
4.1	Introduction	39
4.2	Fundamental balances and thermodynamic laws	41
4.2.1	Balances of masses and microforces	41
4.2.2	Thermodynamics	42
4.2.3	Larché–Cahn derivatives	44
4.3	Constitutive equations	47
4.3.1	Thermodynamical constraints	47
4.3.2	Chemical reaction in ideal solutions	49

4.3.3	Chemical reaction in non-ideal solutions	50
4.4	Configurational fields	52
4.5	Dimensionless Cahn-Hilliard equations	56
4.6	An energetic variational approach for the multicomponent Cahn–Hilliard equations	57
4.6.1	Free energies	57
4.6.2	Chemical potentials	58
4.6.3	Generalized Fick’s law	59
5	Derivation of a coupled chemo-mechanical system	61
5.1	Introduction	62
5.2	Fundamental balances and thermodynamics laws	63
5.2.1	Kinematics of the motion	63
5.2.2	Fundamental balances	66
5.2.3	Thermodynamics laws and free energy inequality	69
5.3	Constitutive relations and Coleman-Noll procedure	72
5.4	Dimensionless analysis of the system of chemo-mechanical equations	76
6	Numerical simulation	78
6.1	Reaction-diffusion process of a four phases system	78
6.2	The merging of circular inclusions	87
6.3	The inhomogeneous thermodynamic pressure in solid solutions	96
6.4	Coupled chemo-mechanical responses of solid solutions	110
6.4.1	Reversible chemical reaction of random distributed phases	111
6.4.2	Ripening of spherical inclusions	129
A	Copyright clearance ”Reactive n-species Cahn–Hilliard system: A thermodynamically-consistent model for reversible chemical reaction”	147

List of Figures

2.1	represents the free energy as a function of absolute temperature. Values of ϑ above ϑ_c generates a single stable phase. On the other hand, values of ϑ below ϑ_c generates a double well potential	22
3.1	shows an idealized cubic crystalline structure. The atoms inside the crystalline structure are more energetically stable than the atoms located on the surface since they are bounded by more neighboring atoms.	28
3.2	(a) depicts an idealised configuration of a solid composed of two aggregates and matrix. The dynamics described by the Ostwald ripening effect will control the dissolution of the small aggregate and eventually its precipitation onto the surface of the larger aggregate once the solution gets supersaturated, moreover (b), (c) and (d) showcase the evolution under such mechanism. Moreover, as the concentration of the smaller inclusion is depleted, the stress field changes and such process drives the final shape of the large inclusion.	29
3.4	shows the elastic energy $\hat{\psi}^{el}$ as a function of the local concentration. The parametrisation shows the effect of the swelling parameter ω on the elastic energy $\hat{\psi}^e$	33
3.5	shows the microstructure of a solid solution composed of two phases. The concentration of the phases A and B correspond to φ_A^{eq} and φ_B^{eq} , respectively. The interface, where the concentration varies between φ_A^{eq} and φ_B^{eq} , embraces the chemical properties of both the phase A and B.	34

3.6	(a) represents the free energy potential of the homogeneous system. The double well potential function allows for phase separation where the local minimum value of each well accounts for the concentration at equilibrium of each phase, and (b) sketches the chemical potential as a function of the concentration. By definition, for the multicomponent system, the chemical potentials are the variational derivative of the Helmholtz free energy with respect to the phase concentrations.	35
5.1	The deformation field χ defines the kinematics of the motion of the particles in the body from a configuration \mathbf{B} onto another configuration \mathcal{B}_t	64
6.1	Temporal evolution of the concentration for species φ^1 , φ^2 , φ^3 , and φ^4 , respectively	81
6.2	Temporal evolution of interfacial energies and masses for φ^1 - φ^2 , φ^1 - φ^3 , and φ^1 - φ^4 , respectively	84
6.3	Temporal evolution of interfacial energies and masses for φ^2 - φ^3 , φ^2 - φ^4 , and φ^3 - φ^4 , respectively	85
6.4	Temporal evolution of free energy.	86
6.5	Phase-field evolution before the merging. Left: φ^1 ; Middle: φ^2 ; Right: φ^3	91
6.6	Phase-field evolution after the merging. Left: φ^1 ; Middle: φ^2 ; Right: φ^3	92
6.7	Streamlines of the relative configurational traction $\mathbf{C}_\sigma \nu^\alpha$, level curve \mathcal{L}_0^α (black) upon which $\varphi^\alpha = 0$	93
6.8	Streamlines of the relative configurational traction $\mathbf{C}_\sigma \nu^\alpha$, level curve \mathcal{L}_0^α (black) upon which $\varphi^\alpha = 0$	94
6.9	Streamlines of the relative configurational traction $\mathbf{C}_\sigma \nu^\alpha$, level curve \mathcal{L}_0^α (black) upon which $\varphi^\alpha = 0$	95
6.10	Streamlines of the relative configurational traction $\mathbf{C}_\sigma \nu^\alpha$, level curve \mathcal{L}_0^α (black) upon which $\varphi^\alpha = 0$	96
6.11	represents the spatial distribution of the initial concentrations for both φ^1 and φ^2 . Regions colored by red and blue represent the species φ^1 and φ^2 , respectively. As the chemical and mechanical processes evolve, the system favours generating a new species φ^3 which contributes to the volumetric stress formation in the solid as it nucleates and grows.	98

6.12	depicts the behaviour of the three phases system at the early stages. According to the evolution, the system is mostly controlled by the interleaving of phase separation and coarsening. Therefore, the volume changes and subsequent stress generation result from the diffusion process itself leading to the inhomogeneous pressure distribution	103
6.13	portraits the dynamics of the system as it follows the Ostwald ripening effect. The unstable particles on the surface dissolve and go into the solution, and once the solution gets supersaturated, these particles tend to precipitate onto the surface of the more stable structures. Consequently, the larger structure in the system grows.	104
6.14	shows the reaction between the species φ^1 and φ^2 to produce a new phase C along their boundary. The evolution favours to consume in a greater proportion the phase φ^1 than the phase φ^2 . The simulation results show how the nucleation and growth of phases induce volumetric stresses which in turn contribute to generate the inhomogeneous pressure distribution.	105
6.15	suggests that the chemical reaction acts as either a source or sink of energy. In this particular case, it contributes to increasing the free energy of the system. Once the chemical process ceases, the system minimizes its free energy solely by mass transport leading to the steady state at $t > 9.33 \times 10^4$. Finally, the thermodynamic pressure at $t > 9.33 \times 10^4$, which results from the contribution of both chemical and mechanical responses of the solid, defines the equilibrium of the metamorphic system.	106
6.16	depicts that when a system undergoes a chemical process, either mass transport or chemical reaction, the dynamics favours to either produce or destroy the interface between the species. Thus, the interfacial energy must change according to this evolution process.	107
6.17	shows the free energy evolution and marks the beginning of processes such as phase separation and coarsening, Ostwald ripening effect, the chemical reaction and steady state.	108
6.18	depicts the elastic energy of a neo-Hookean solid model. Since no deformation is induced across the solid boundaries, the variation of the elastic energy entirely results from the volumetric stresses associated with the variations in local composition.	108

6.19	represents the spatial distribution of the initial concentrations for ϕ^1 , ϕ^2 , and ϕ^3 together with the initial displacements. Top left: ϕ^1 ; Top middle: ϕ^2 ; Top right: ϕ^3 ; Bottom left: u_x ; Bottom right: u_y . The phases ϕ^1 and ϕ^2 react to form ϕ^3 which in turn decomposes into ϕ^1 , and ϕ^2 as a result of the backward chemical reaction. The formation of ϕ^3 and concomitant decomposition into ϕ^1 and ϕ^2 favour to generate volumetric stresses.	112
6.20	shows the beginning of the phase separation process. Top left: ϕ^1 ; Top middle: ϕ^2 ; Top right: ϕ^3 ; Bottom left: u_x ; Bottom right: u_y .	115
6.21	shows the evolution at $t = 9.03 \times 10^{-6}$. Top left: ϕ^1 ; Top middle: ϕ^2 ; Top right: ϕ^3 ; Bottom left: u_x ; Bottom right: u_y	119
6.22	shows the evolution at $t = 1.26 \times 10^{-5}$. Top left: ϕ^1 ; Top middle: ϕ^2 ; Top right: ϕ^3 ; Bottom left: u_x ; Bottom right: u_y	120
6.23	shows the evolution at $t = 5.64 \times 10^{-5}$. Top left: ϕ^1 ; Top middle: ϕ^2 ; Top right: ϕ^3 ; Bottom left: u_x ; Bottom right: u_y	121
6.24	shows the evolution at $t = 4.26 \times 10^{-4}$. Top left: ϕ^1 ; Top middle: ϕ^2 ; Top right: ϕ^3 ; Bottom left: u_x ; Bottom right: u_y	122
6.25	shows the evolution at $t = 5.72 \times 10^{-4}$. Top left: ϕ^1 ; Top middle: ϕ^2 ; Top right: ϕ^3 ; Bottom left: u_x ; Bottom right: u_y	123
6.26	shows the evolution at $t = 1.28 \times 10^{-3}$. Top left: ϕ^1 ; Top middle: ϕ^2 ; Top right: ϕ^3 ; Bottom left: u_x ; Bottom right: u_y	124
6.27	shows the evolution at $t = 1.84 \times 10^{-3}$. Top left: ϕ^1 ; Top middle: ϕ^2 ; Top right: ϕ^3 ; Bottom left: u_x ; Bottom right: u_y	125
6.28	shows the evolution at $t = 2.17 \times 10^{-3}$. Top left: ϕ^1 ; Top middle: ϕ^2 ; Top right: ϕ^3 ; Bottom left: u_x ; Bottom right: u_y	126
6.29	shows the steady state reached at $t = 1.74 \times 10^{-1}$. Top left: ϕ^1 ; Top middle: ϕ^2 ; Top right: ϕ^3 ; Bottom left: u_x ; Bottom right: u_y . . .	127
6.30	Interfacial energies for phases ϕ^1 , ϕ^2 , and ϕ^3 along with their masses	128
6.31	depicts the free energy evolution. During the whole evolution, the free energy is monotonically-decreasing.	129
6.32	represents the spatial distribution of the initial concentrations for ϕ^1 , ϕ^2 , and ϕ^3 . Left: ϕ^1 ; Middle: ϕ^2 ; Right: ϕ^3 . The inclusions differ in size which drives the ripening process.	131

6.33	portraits the initial displacements in the solid. The initial state corresponds to a undeformed solid, therefore the displacements are zero. The deformation will result from the mass transport of the phases as the smaller inclusions go into the solution and deposit in the surface of the larger inclusions. Left: u_x ; Middle: u_y ; Right: u_z	131
6.34	represents the spatial distribution of the concentrations for $\hat{\varphi}^1$, $\hat{\varphi}^2$, and $\hat{\varphi}^3$ at $t = 2.79 \times 10^{-6}$. Left: $\hat{\varphi}^1$; Middle: $\hat{\varphi}^2$; Right: $\hat{\varphi}^3$.	133
6.35	portraits the displacements in the solid at $t = 2.79 \times 10^{-6}$. Left: u_x ; Middle: u_y ; Right: u_z .	133
6.36	represents the spatial distribution of the concentrations for $\hat{\varphi}^1$, $\hat{\varphi}^2$, and $\hat{\varphi}^3$ at $t = 5.476 \times 10^{-6}$. Left: $\hat{\varphi}^1$; Middle: $\hat{\varphi}^2$; Right: $\hat{\varphi}^3$.	133
6.37	portraits the displacements in the solid at $t = 5.476 \times 10^{-6}$. Left: u_x ; Middle: u_y ; Right: u_z .	134
6.38	represents the spatial distribution of the concentrations for $\hat{\varphi}^1$, $\hat{\varphi}^2$, and $\hat{\varphi}^3$ at $t = 5.626 \times 10^{-3}$. Left: $\hat{\varphi}^1$; Middle: $\hat{\varphi}^2$; Right: $\hat{\varphi}^3$.	134
6.39	portraits the displacements in the solid at $t = 5.626 \times 10^{-3}$. Left: u_x ; Middle: u_y ; Right: u_z .	134
6.40	represents the spatial distribution of the concentrations for $\hat{\varphi}^1$, $\hat{\varphi}^2$, and $\hat{\varphi}^3$ at steady state. Left: $\hat{\varphi}^1$; Middle: $\hat{\varphi}^2$; Right: $\hat{\varphi}^3$.	135
6.41	portraits the displacements in the solid at steady state. Left: u_x ; Middle: u_y ; Right: u_z .	135
A.1	Copyright clearance from Journal of Computational and Applied Mathematics	148
A.2	Copyright clearance from Journal of Computational and Applied Mathematics	149
A.3	Copyright clearance from Dr Luis Espath	149
A.4	Copyright clearance from Dr Adel Sarmiento	150
A.5	Copyright clearance from Dr Lisandro Dalcin	150
A.6	Copyright clearance from Dr Adriano Cortes	151
A.7	Copyright clearance from Prof Victor Calo	151

List of Tables

5.1	Physical parameters for the multicomponent system	74
6.1	Chemical and physical parameters for the three phases system . .	88
6.2	Chemical and physical parameters to calculate the thermodynamic pressure	99
6.3	Chemical and physical parameters that control the spinodal de- composition process	113

Chapter 1

Introduction

Complex physical and chemical processes rule the evolution of metamorphic minerals. Deep in the Earth, both high temperature and pressure allow for solid diffusion and chemical reactions between rock minerals, which in turn, lead to phase transformations and induced deformation. Furthermore, the transport of chemical constituents, particularly during uphill diffusion, induces phase separation processes as a result of the geothermal gradient in the crust. When considering a deformable medium, such as the metamorphic rock complexes in the lithosphere, mineral reactions may affect the rock strength and its mechanical properties. Analogously, high mechanical strength may suppress either the volumetric shrinkage or swelling associated with the local volume changes caused by the chemical processes [1]. Thereby, the chemical processes, associated with diffusion and chemical reactions, induce volume changes that lead to stresses around the reaction site. Milke et al. [2] define that positive volume changes involve the creation of space by moving out mass from the reaction site, and thus, the reaction products can grow and accommodate. On the contrary, negative volume changes induce mass transport into the reaction site by consuming the reactant phases. Hence, there exists an essential interaction between the chemo-mechanical processes of metamorphic rocks which eventually control the dynamics of their microstructural evolution and properties. Metamorphic rocks are complex systems composed of fractures, several mineral, and grain-boundaries where the chemical and mechanical properties may vary in each direction. Without loss of generality, this theoretical and numerical work only focuses on the description of single minerals as solid solutions with the purpose of understanding complex processes such as coupled chemo-mechanical responses during metamorphism.

The purpose of this thesis is to develop a thermodynamically consistent model to describe common processes for solid solutions such as coupled reaction-diffusion, interfacial effects, and deformation based on the framework of modern continuum mechanics, thermodynamics far from equilibrium, and phase field models. We apply the aforementioned framework to understand these processes in metamorphic minerals modelled as solid solutions composed of several phases. Consequently, we derive a set of coupled reactive-chemo-mechanical equations for solid solutions. In this effort, we derive a multicomponent reaction-diffusion system which takes into account interfacial effects, namely the phases have an interface of non-zero thickness where physical and chemical properties vary smoothly. As a result of the interfaces, the mass transport process is driven by changes in the chemical potentials which depend on the phases concentrations and the interface curvature. Mathematically speaking, the chemical potential is a function of both the concentrations and their laplacians. This process is commonly called non-Fickian diffusion.

Our derivation corresponds to the multicomponent version of the Cahn–Hilliard model which is coupled with a general law of mass action to describe possible chemical reactions between the phases. We also assume that phases in the solid solution follow a mass constraint imposed by the crystalline lattice. In particular, we consider a saturated system. Namely, the summation of the phases concentrations must always equal one. We review the mathematical properties and concomitant physical meaning of the system of partial equations which emerge from the underlying balance laws and constitutive behaviour. By doing so, we propose a novel constitutive behaviour for the interfacial energy tensor which, opposite to the classical definition, i.e., a diagonal and positive definite tensor, suggests that negative interfacial interactions are also possible as long as the constrained system leads to a positive definite tensor. This implies a positive definite diffusion tensor and a physically sound diffusion process. To capture the elastic behaviour of the solid solution, in particular the impact of the chemical processes towards stress-generation, we couple the aforementioned reactive multicomponent Cahn–Hilliard system with a neo-Hookean solid model. This allows us to study the mechanical behaviour of the solid solution when mass transport and chemical reactions take place. In this introduction, we review the evidence of the chemo-mechanical interactions of solid solutions in geological processes to justify the choice of deriving a fully-coupled thermodynamically consistent model.

The chapter is structured as follows: In section §1.1, we provide the evidence of

chemo-mechanical interactions in metamorphic rocks. In particular, we point out that the pressure of these systems must have contributions from both the chemical and mechanical responses of the solid and it corresponds to the thermodynamic pressure. Moreover, we show phase separation processes in ternary feldspars during cooling.

1.1 Evidence and modelling of chemo-mechanical responses in mineral solid solutions

Recent studies on metamorphic petrology and microstructural observations suggest the influence of mechanical effects upon chemically active metamorphic rocks [1–7]. An example of this coupling is the grain-scale pressure variations in high-temperature metamorphic rocks. As pointed out by Tajčmanová et al. [1], the effects of an inhomogeneous pressure distribution can be maintained even in the microscale at ambient conditions. The study of minerals under residual pressure can be carried out by advanced observational techniques. Howell et al. [8] use an analytical model that relates geometric features of both the host rock and the inclusion together with a quantitative birefringence analysis to study the residual stress of graphite inclusion in diamond. Their measurements show the distribution of internal inhomogeneous pressure around the graphite inclusion caused by the residual stresses.

Conventionally, at a given depth, the pressure is assumed spatially homogeneous and equal to the lithostatic value given by Archimedes' formula. Nevertheless, the formation of ultrahigh-pressure rocks suggests that pressure does not always translate into depth [4]. The understanding of the nature of such deviations is crucial since pressure provides, for instance, a constraint for the description of the dynamics of orogens as well as an indirect measurement of the depth history of the sample. The source of such discrepancies is the complex chemo-mechanical interactions as the metamorphic rock complexes evolve towards equilibrium, and most importantly, that both processes are strongly interdependent. Moulas et al. [4] provide a comprehensive review of the evidence that metamorphic rocks maintain and record significant pressure deviations from the lithostatic values. During prograde metamorphism, high pressure and temperature conditions induce the formation of garnet porphyroblasts that harbor quartz and coesite inclusions. As

the inclusions grow, the metamorphic system endures large volumetric stresses associated with the expansion of the inclusions in the relaxed host matrix. Eventually, the metamorphic system exhibits chemical zonation where each aggregate has different chemical and mechanical properties. Such heterogeneity generates spatial variations in pressure. The effect of the inhomogeneous pressure seems to be critical and will allow us to calibrate geodynamics models as well as to describe the evolution of fabrics and microstructures.

To date, a few modeling attempts of these physical and chemical interactions, were made. For instance, Tajčmanová et al. [1] study the effect of inhomogeneous pressure distributions by using a chemo-mechanical model. They formulate three cases that showcase the impact of mass fluxes and external loading to achieve equilibrium while taking into account both pressure gradients and constant pressure. As a consequence, their results suggest that a rock composed of two minerals with different mechanical properties will evolve in such a way that favours mechanically maintained inhomogeneous pressure distributions. Powell et al. [9] describe non-hydrostatically-stressed metamorphic systems as well as equilibrium conditions at grain-boundaries. In their setting, a non-hydrostatically-stressed solid accounts for a solid under inhomogeneous stress distribution. Essentially, their formulation follows the ideas behind the Larché-Cahn's model for multicomponent solids where due to the lattice constrain imposed by the crystalline structure the chemical potentials of the multicomponent system are calculated through the Larché-Cahn derivative [10–12]. This derivative leads to the definition of a relative chemical potential. Thus, their proposal leads to a thermodynamic equilibrium for metamorphic systems that accommodates spatial variations in the pressure. The possibility of describing evolution scenarios for metamorphic rocks with spatial inhomogeneous pressure distributions collides with the classical description of the evolution of metamorphic rocks. The classical interpretations assume thermodynamic equilibrium to explain metamorphic mineral assemblages via thermobarometry techniques and phase diagrams. Therefore, the evolution processes that induce heterogeneous pressure distributions imply that these techniques may not be robust to characterize metamorphic systems. That is, these inhomogeneous pressure conditions contradict the foundational assumptions of uniform pressure and temperature distributions. Thus, the nature of the pressure distribution that defines the equilibrium of metamorphic rocks and especially how to calculate and define this quantity are still open questions in our opinion. As pointed out by Hobbs and Ord [3] (and references therein), the thermody-

dynamic equilibrium is entirely characterized by the thermodynamic pressure. This pressure can be calculated as the partial derivative of the Helmholtz energy with respect to specific volume or when considering Gibbs free energy, the partial derivative has to be taken with respect to the volume. We believe that heretofore, in the geosciences literature, the lithostatic pressure has erroneously been used to describe the state of equilibrium of the metamorphic rocks. And recently, works on inhomogeneous pressure distributions use the mean stress to characterize equilibrium conditions [1, 13]. Such pressure definitions only make sense from a thermodynamic point of view when the solid behaves elastically without ongoing chemical processes [3]. Solids under either viscoelastic, diffusional creep, or plastic behavior as well as ongoing chemical reactions between the constituent phases relate dissipative processes which lead to additional contributions to the definition of thermodynamic pressure [3]. As a consequence, we seek to identify and define the pressure that properly describes the chemical equilibrium conditions for metamorphic systems. Hobbs and Ord have carried out an extensive review on the subject [3, 14] (see also e.g [15] and references therein). The phases that compose these mineral solid solutions diffuse at different rates, and when considering changes in temperature as a result of uphill diffusion, for instance during cooling, phase separation processes such as spinodal decomposition may occur. Ternary feldspars formed by orthoclase, anorthite, and albite show spinodal decomposition during cooling. Such process controls the coarsening kinetics of the exsolution microstructure [16, 17].

We derive the model following the framework of modern continuum mechanics and thermodynamics far from equilibrium. Modern continuum mechanics deals with the mechanical and chemical behaviour of bodies. The body, which for the purpose of this dissertation corresponds to a solid composed of several phases, is treated as a continuum medium rather than a set of discrete particles. The mathematical structure of this framework relies on the description of scalar, vector, tensor fields, and their relations. Along this thesis, we use classical definitions such as Reynolds transport, divergence theorem, and localisation theorem as well as the laws of thermodynamics. This allows to build up a system of coupled chemo-mechanical equations constrained by the entropy inequality (Clausius-Duhem inequality). We use phase field models to describe the evolution of interfaces by following the multicomponent Cahn–Hilliard model.

Chapter 2

Phase field models

We derive the binary version of the Cahn-Hilliard phase field model from a mathematical and physical standpoint. We show some properties of the equation and how it allows to model interfacial phenomena. In particular, we show the equations capture interface diffusion.

2.1 Introduction

The modelling of interfacial phenomena emerges as a promising tool to understand the dynamics of different processes which occur along a small region between the phases called the interface. Within the interface, the chemical and mechanical properties of each phase change from one bulk phase to the other. Interfacial modelling is then important in a variety of engineering processes. Particularly in geosciences, interfacial interactions are responsible for driving the Ostwald ripening effect in garnets which allows the smaller aggregates to gather and form bigger ones as well as spinodal decomposition in multicomponent mineral solutions during exsolution processes [18–21]. The later examples are non-trivial to study experimentally. At the most fundamental level, comprehensive theoretical and numerical modelling of such mechanisms helps to understand the underlying processes and their dynamics. An important aspect of interfacial modelling is to track the evolution of the interfaces. The latter controls the microstructure of the material and allows to study the chemical and physical responses under different conditions of pressure and temperature. To date, many models have

been published to track the evolution of interfaces. From explicit to implicit models, their common aim is to characterize how the interfaces diffuse through the material domain and their final configuration. Herein, we focus on models where the interfaces are tracked implicitly. In this effort, the phase field method provides a robust framework. The method relies on an order parameter which describes the tempo-spatial distribution of the phases. Opposite to the explicit methods, the interface evolution is given by the solution of a temporal partial differential equation of the order parameter. Such framework successfully models phase separation, fracture formation, solidification, and viscous fingering processes [22–25]. The ideas behind the phase field method were formerly proposed by Van der Waals [26]. Van der Waals’ brilliant idea was to include a region of non-zero thickness between the phases where chemical and physical properties vary smoothly. The interfaces are implicitly represented by a scalar-value field where a partial differential equation characterises its evolution. For the purpose of this thesis, we model the interfacial effects using the Cahn-Hilliard equation. By doing so, we manage to capture mass transport processes coupled with interface diffusion. A wide extent of this thesis will be dedicated to the multicomponent version of this equation as well as its physical and numerical properties. Furthermore, when coupling the Cahn-Hilliard equation with deformation and chemical reactions, we manage to model complex solid solutions undergoing non-Fickian reaction-diffusion processes coupled with elasticity. In this chapter, we derive the numerical and physical version of the binary Cahn-Hilliard.

The chapter is structured as follows: In section §2.2.1, we study the Cahn-Hilliard model from a mathematical point of view. In this effort, we show the strong form of the system together with the boundary conditions, followed by section §2.2.2 where we consider the physical derivation of the equation. Hence, we show the derivation of the Ginzburg-Landau free energy.

2.2 The Cahn-Hilliard equation

The Cahn-Hilliard equation is a fourth-order, nonlinear partial differential equation. Cahn and Hilliard originally introduced the so-called Cahn-Hilliard equation to model phase separation processes [27]. Changes in temperature drive the phase separation which eventually form fully separated phases. The model has been widely used to capture the underlying physics of biological entities such as

wound healing and tumor growth [28, 29], solidification [30], and phase separation of binary systems [31].

2.2.1 Mathematical derivation

Let \mathcal{B} denote a fixed region of a three dimensional point space \mathcal{E} and \mathcal{P} an arbitrarily fixed subregion of \mathcal{B} with boundary $\mathcal{S} = \partial\mathcal{P}$ oriented by an outward unit normal \mathbf{n} . The boundary is composed of two parts $\partial\mathcal{P}_g$ and $\partial\mathcal{P}_h$. Therefore, $\partial\mathcal{P} = \overline{\partial\mathcal{P}_g} \cup \overline{\partial\mathcal{P}_h}$. The underlying aim of the phase field model is to find fields in \mathcal{P} that minimises a particular energy potential that describes the evolution of the system. Particularly, for the Cahn–Hilliard model, this energy functional corresponds to the Ginzburg-Landau free energy, i.e.,

$$\mathcal{F}_{\text{CH}}[\varphi(\mathbf{x}, t)] = \int_{\mathcal{P}} \Psi(\varphi) + \frac{\Gamma}{2} |\nabla\varphi|^2 \, dv, \quad (2.1)$$

where the order parameter φ represents the concentration of one component in the solution varying in space \mathbf{x} and time t , and Γ accounts for the interfacial energy resulting from interfacial interactions. This energy functional is composed of two terms $\Psi(\varphi)$, and $\frac{\Gamma}{2} |\nabla\varphi|^2$ to model the bulk and interfacial contributions, respectively. In addition, $\sqrt{\Gamma}$ represents the length scale of the system associated with interface thickness between the two species. In the Ginzburg-Landau free energy, $\Psi(\varphi)$ encompasses entropic effects and is given by

$$\Psi(\varphi) = (\varphi \ln(\varphi) + (1 - \varphi) \ln(1 - \varphi)) + \bar{\vartheta}_c 2\varphi(1 - \varphi). \quad (2.2)$$

The dimensionless number $\bar{\vartheta}_c$ relates the critical temperature between the phases and the absolute temperature. The definition of the bulk free energy (2.2) makes sure that the values of the order parameter φ keep in the range of $[0, 1]$. Furthermore, the potential (2.2) represents a double well function with minima at the well points. The strong form of the governing equation along with the boundary conditions for the Cahn-Hilliard system can be stated as follows

$$\begin{aligned} \dot{\varphi} - \nabla \cdot (M_\varphi \nabla(\Psi'(\varphi) - \Gamma \Delta\varphi)) &= 0 & \text{in } \mathcal{P} \times (0, T), \\ \varphi &= g & \text{on } \partial\mathcal{P}_g \times (0, T), \\ M_\varphi \nabla(\Psi'(\varphi) - \Gamma \Delta\varphi) \cdot \mathbf{n} &= h & \text{on } \partial\mathcal{P}_h \times (0, T), \\ M_\varphi \Gamma \nabla\varphi \cdot \mathbf{n} &= 0 & \text{on } \partial\mathcal{P} \times (0, T), \\ \varphi(\mathbf{x}, 0) &= \varphi_0(\mathbf{x}) & \text{in } \overline{\mathcal{P}}, \end{aligned}$$

where $\varphi_0(\mathbf{x})$ accounts for the initial distribution of the concentration, M_φ is a degenerate mobility, and $\Psi'(\varphi)$ is given by $\Psi'(\varphi) = \partial_\varphi \Psi(\varphi)$. The definition of the degenerate mobility is

$$M_\varphi = D\varphi(1 - \varphi), \quad (2.3)$$

where D accounts for a positive diffusion coefficient. On the other hand, the chemical potential reads

$$\Psi'(\varphi) = \ln \frac{\varphi}{1 - \varphi} + 2\bar{\vartheta}_c(1 - 2\varphi) - \bar{\sigma}\bar{\ell}\Delta\varphi. \quad (2.4)$$

The Cahn-Hilliard equation for multicomponent systems will be derived in subsequent chapters which allow to model complex system undergoing spinodal decomposition.

2.2.2 Physical derivation

In the sequel, we derive an expression for the Ginzburg-Landau free energy from a physical point of view [32]. Such a potential characterises the free energy of a system embodied in an isotropic control volume \mathcal{P} which has non-uniform spatial distributions in concentration. As outlined above, the Ginzburg-Landau potential reads

$$F(\varphi) = \int_{\mathcal{P}} V(\varphi) + \frac{\Gamma}{2} |\nabla\varphi|^2 dv. \quad (2.5)$$

$V(\varphi)$ represents the free energy of the homogeneous system, Γ is the interfacial energy as a function of the interface thickness, and $\nabla\varphi$ is the composition gradient resulting from the spatial distributions in concentration. Essentially, this free energy is composed of a homogeneous contribution $V(\varphi)$, namely the energy that the system would have as it were a homogeneous solution together with a gradient energy $\frac{\Gamma}{2} |\nabla\varphi|^2$ as a result of the local changes in composition.

The Ginzburg-Landau free energy potential (2.5) results as follows: Let us consider a binary fluid mixture composed of A and B particles when diffusion is the primary controlling mechanism. The phase field $\phi = 0$ corresponds to the species constituted of particles A. Analogously, the phase field $\phi = 1$ represents the species constituted of particles B. Moreover, assume a linear interpolation between the two particles which characterises the species composed of both particles. For the binary mixture A-B, the interactions between A-A and B-B molecules are favourable. On the contrary, interactions between A-B molecules

are unfavourable. The energy potential (2.5) takes into account such unfavourable interactions via $\nabla\phi$. In the free energy (2.5), $V(\phi, \vartheta)$ represents a potential energy landscape which accounts for the variation in energy from a random to a ordered phase as the temperature decreases. Using regular solution theory of binary systems and their description via mean field theory, the potential $V(\phi, \vartheta)$ is given by

$$V(\varphi, \vartheta) = k_B \left(2\vartheta_c \phi(1 - \phi) + \vartheta(\phi \ln(\phi) + (1 - \phi) \ln(1 - \phi)) \right) \quad (2.6)$$

where k_B , ϑ_c , and ϑ are the Boltzmann constant, the critical temperature between molecules A and B, and the absolute temperature, respectively. Figure 2.1 shows the behaviour of (2.6) as we vary the absolute temperature ϑ . Figure 2.1 shows a single stable phase when the absolute temperature $\vartheta > \vartheta_c$ together with a double well function, $\vartheta < \vartheta_c$, where two stable phases emerge. We use the double-tangent construction of coexisting phases to find the equilibrium position ϕ_{eq} of the double well functional, i.e.,

$$\left. \frac{\partial V}{\partial \phi} \right|_{\phi_{eq}} = 0 \quad (2.7)$$

which leads to

$$\phi_{eq} - \frac{1}{2} = \frac{1}{4} \frac{\vartheta}{\vartheta_c} \ln \left(\frac{\phi_{eq}}{1 - \phi_{eq}} \right). \quad (2.8)$$

The equation (2.8) has two solutions, ϕ_1 and ϕ_2 , which corresponds to the values at the wells (see Figure 2.1). Therefore, we have that for values of $\vartheta < \vartheta_c$, two

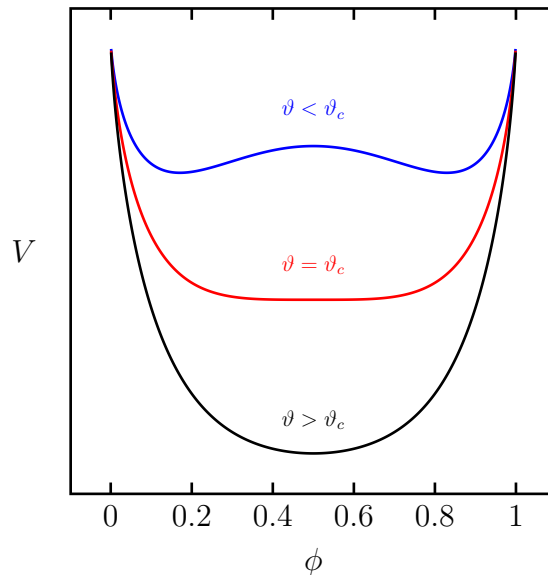


Figure 2.1 represents the free energy as a function of absolute temperature. Values of ϑ above ϑ_c generates a single stable phase. On the other hand, values of ϑ below ϑ_c generates a double well potential

states emerge continuously from one as a result of phase separation. On the other hand, the free energy of the system embodied in an isotropic control volume \mathcal{P} is given by

$$F(\phi) = N_v \int_{\mathcal{P}} h \, dv \quad (2.9)$$

where N_v is the number of molecules and h is the local free energy of a non-uniform composition such that $h = h(\phi, \nabla\phi, \Delta\phi, \dots)$. We expand the local free energy of the non-uniform composition system h about $\phi_0 = (\phi, 0, 0, \dots)$ using multivariate Taylor series. Following Cahn and Hilliard [32], we drop the terms higher than two. In addition, we assume an isotropic medium and invariance to rotations and reflection. Thereby, one can prove that

$$h(\phi, \nabla\phi, \Delta\phi, \dots) = V(\phi) + k_1\Delta\phi + \frac{k_2}{2}|\nabla\phi|^2 + \dots \quad (2.10)$$

where

$$k_1 = \frac{\partial h(\phi_0)}{\partial \phi_{ii}} \quad i = 1, 2, 3 \quad (2.11)$$

and

$$k_2 = \frac{\partial^2 h(\phi_0)}{\partial \phi_i^2} \quad i = 1, 2, 3. \quad (2.12)$$

In (2.10), $V(\phi)$ corresponds to the Helmholtz free energy. Hence, the total free energy of the control volume \mathcal{P} reads

$$F(\phi) = N_v \int_{\mathcal{P}} h \, dv \quad (2.13)$$

$$= N_v \int_{\mathcal{P}} \left(V(\phi) + k_1\Delta\phi + \frac{k_2}{2}|\nabla\phi|^2 + \dots \right) \, dv. \quad (2.14)$$

Following Cahn and Hilliard [32], we carry out an integration by parts of the term $k_1\Delta\phi$ where we assume the term $\partial_n\phi$ vanishes at the boundary. As a consequence, we obtain

$$\int_{\mathcal{P}} (k_1\Delta\phi) \, dv = - \int_{\mathcal{P}} \left(\frac{\partial k_1}{\partial \phi} \right) \, dv \quad (2.15)$$

By inserting (2.15) into (2.13), we get

$$\frac{F(\phi)}{N_v} = \int_{\mathcal{P}} \left(V(\phi) + k_1\Delta\phi + \frac{k_2}{2}|\nabla\phi|^2 + \dots \right) \, dv \quad (2.16)$$

$$= \int_{\mathcal{P}} \left(V(\phi) + \left(-\frac{\partial k_1}{\partial \phi} + \frac{k_2}{2} \right) |\nabla\phi|^2 + \dots \right) \, dv \quad (2.17)$$

$$= \int_{\mathcal{P}} \left(V(\phi) + \frac{\Gamma}{2} |\nabla\phi|^2 + \dots \right) \, dv \quad (2.18)$$

where

$$\Gamma = 2 \left(-\frac{\partial k_1}{\partial \phi} + \frac{k_2}{2} \right). \quad (2.19)$$

We drop higher order terms in (2.16) and insert the definition (2.6) in (2.16). Thus, the free energy of the phase field ϕ as a function of space and time reads

$$\mathcal{F}^* = \int_{\mathcal{P}} \left[(\phi \ln(\phi) + (1 - \phi) \ln(1 - \phi)) + \bar{\vartheta}_c 2\phi(1 - \phi) - \frac{\bar{\sigma}\bar{\ell}}{2} |\nabla\phi|^2 \right] dv \quad (2.20)$$

where $\mathcal{F}^* = \frac{\mathcal{F}[\phi(\mathbf{x},t)]}{N_v k_B \theta}$, and $\bar{\vartheta}_c$, $\bar{\sigma}$, $\bar{\ell}$ are dimensionless numbers which depend on the critical temperature and interfacial energy. These numbers will be shown in subsequent chapters. In general, \mathcal{F}^* quantifies the free energy of a tempo-spatial distribution of ϕ . Consequently, the variation of this energy with respect to those distribution is the chemical potential. Thus, given the definitions for \mathcal{F}^* and ϕ , we can calculate the chemical potential μ , such that

$$\mu = \frac{\delta\mathcal{F}^*}{\delta\phi} \quad (2.21)$$

where the variational derivative reads

$$\frac{\delta}{\delta\phi} = \frac{\partial}{\partial\phi} - \nabla \cdot \frac{\partial}{\partial\nabla\phi} + \Delta \frac{\partial}{\partial\Delta\phi}. \quad (2.22)$$

In (2.22), $\nabla \cdot$, ∇ , and Δ are the divergence, gradient, and laplacian operators. Fick's law states that the mass flux is proportional to the chemical potential gradient, such that

$$\mathbf{j} = -\mathbf{M}\nabla\mu \quad (2.23)$$

where \mathbf{M} is the mobility tensor. In subsequent chapters, we will show a de-generated multicomponent version of the mobility as a function of the species concentrations. In the binary mixture, we have that

$$\mathbf{M} = D\phi(1 - \phi) \quad (2.24)$$

The phase field ϕ is conservative. Therefore, its evolution can be recasted by the mass balance

$$\dot{\phi} + \nabla \cdot \mathbf{j} = 0. \quad (2.25)$$

On the other hand, the chemical potential in (2.23) is

$$\mu = \frac{\delta\mathcal{F}^*}{\delta\phi} = \ln \frac{\phi}{1 - \phi} + \bar{\vartheta}_c 2\phi(1 - 2\phi) - \bar{\sigma}\bar{\ell}\Delta\phi \quad (2.26)$$

where we apply the variational derivative definition (2.22). Finally, the evolution of the phase field ϕ can be described by

$$\dot{\phi} = \nabla \cdot \left(\mathbf{M}\nabla \left(\ln \frac{\phi}{1 - \phi} + \bar{\vartheta}_c 2\phi(1 - 2\phi) - \bar{\sigma}\bar{\ell}\Delta\phi \right) \right) \quad (2.27)$$

Chapter 3

Modelling the chemo-mechanical responses of mineral solid solutions far from equilibrium under heterogeneous stresses

We study chemically active solid solutions subject to mechanical effects due to heterogeneous stress distributions. We present a fully coupled thermodynamically-consistent model for the chemo-mechanical responses of the solid solution. We introduce the theoretical foundations of different interfacial effects and describe their relation with the chemo-mechanical behaviour of the solid solution. We describe the Helmholtz free energy of a multicomponent deformable solid undergoing both mass transport and chemical reactions. Moreover, the constitutive equations describe the evolution of the system towards equilibrium and satisfy the second law of thermodynamics by construction. Although the constitutive assumption of the elastic energy allows for deformation induced across the solid boundaries, in this section we emphasise the behaviour of systems where the stress generation process is driven solely by the volume changes associated with the chemical processes. Therefore, we do not take into account deformation across the solid boundaries. This chapter serves as a theoretical introduction to subsequent chapters where a mathematical treatment of chemo-mechanical interactions of solid solutions is given. This chapter relies on modern continuum mechanics and thermodynamics far from equilibrium to explain the physical and chemical interactions of solid solutions. An important feature is the definition of the

thermodynamic pressure and its relation with characterisation of metamorphic minerals.

3.1 Introduction

In this chapter, we describe how interactions between interfacial effects, elasticity, diffusion, and chemical reactions engender inhomogeneous stresses distributions in solid solutions. By doing so, we seek to understand the chemo-mechanical behaviour of metamorphic minerals.

The design of the Helmholtz free energy functional accounts for the contributions from the mechanical and chemical responses of the system. With regards to the chemical energy, we use a potential that characterises the dynamics of a solid system which undergoes diffusion together with phase separation in solid state. Interfacial interactions between the phases drive the phase separation process. Accounting for interfacial effects is a choice since not always metamorphic minerals exhibit such a process. Therefore, the chemical energy can be set such that interfacial effects are not taken into account. Analogously, we describe the solid as a compressible neo-Hookean elastic material. We treat the solid as a continuum body with motion described by a deformation field. The kinematics of the motion of the particles in the body define the deformation field. The solid is composed by several phases. In the continuum mechanics literature, such systems are commonly called solid-species solutions. Henceforth, we adopt this denomination.

We derive a set of balance equations in the form of partial differential equations which define how the mass, linear and angular momenta, internal energy and entropy of the solid solution vary in time as the deformation and chemical processes take place (see e.g §4 and §5). As suggested in [33–36], three primary fields govern the coupled chemo-mechanical responses of a solid-species solution: the deformation field, the species concentration, and the chemical potentials. Our description of a solid-species solution builds on the Larché-Cahn model of solids [10, 12, 37, 38]. This model defines the relative chemical potential as a result of the Larché-Cahn derivative [10, 33] (see e.g §4.2.3). The relative chemical potential expresses that two different species may share the same lattice site in the crystalline structure of the solid. The relative chemical potential characterizes the

energy exchange caused by species transport and transformation. This chemical potential describes how the energy changes when one species increases its concentration while simultaneously reducing another one and keeping all other species concentrations fixed. The relative chemical potential expresses the constraints imposed on the diffusion processes by the lattice of the crystalline structure. That is, the diffusion process is only feasible if the variation of the local composition of one species induces a complementary change in another species concentration.

The chapter is structured as follows: in section §3.2, we explain how interfacial mechanisms such as the Ostwald ripening and the Gibbs-Thomson effects result from the interfacial interactions between the phases due the existence of interfaces at their boundaries. These mechanisms play a significant role in the chemo-mechanical behaviour of metamorphic minerals as they are involved, for example, during exsolution processes, mineral crystallisation and recrystallisation. Section §3.3 embodies the definition of a crystalline structure for coherent solid solution. We consider saturated system which imposes a mass constraint in the system. In general, this mass constraint is related to the crystalline structure and the spatial distribution of their atoms. Section §3.4 covers the elastic energy of a neo-Hookean solid solution. In particular, the design of this potential allow deformation resulting from forces applied across the solid boundaries and volume changes as a result of chemical processes. The stress-assisted volume changes contribution is scaled by a swelling parameter which controls the impact of the variation of the phases concentrations towards stress generation. In section §3.5, we introduce the chemical energy as its relation with the phases interfaces. In particular, this setting allows for modelling phase separation processes such spinodal decomposition. However, the chemical energy can be set such that no phase separation takes place. In other words, our design of the chemical energy can also capture conventional mass transport processes such Fickian diffusion. We conclude with §3.6 where the definition of the Helmholtz free energy is considered. This section also embodies the definition of the thermodynamic pressure, an important physical quantity in subsequent chapters.

3.2 Interfacial interactions: The Ostwald ripening and Gibbs-Thomson effects

Our formulation involves non-Fickian diffusion processes as it also relates interfacial diffusion. These interfacial interactions are important since, for example, spontaneous phase separation processes, and the Ostwald ripening and Gibbs-Thomson effects are governed by this mechanism. The interfacial interactions

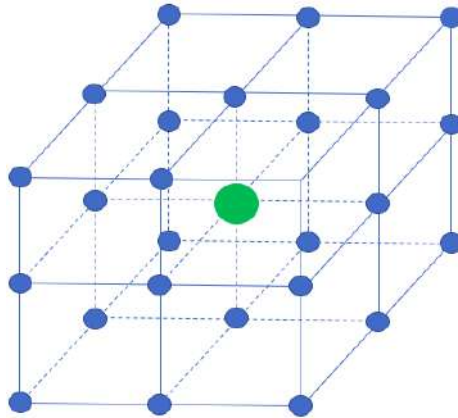


Figure 3.1 shows an idealized cubic crystalline structure. The atoms inside the crystalline structure are more energetically stable than the atoms located on the surface since they are bounded by more neighboring atoms.

explain the Ostwald ripening and Gibbs-Thomson effect which has been reported during the textural evolution of metamorphic rocks [18–20, 39]. The Ostwald ripening effect is a thermodynamically-driven spontaneous process in spatially heterogeneous solutions, with small and large aggregates, as the thermodynamic system moves to a lower energy state by minimizing the interface length. The small aggregates dissolve into the solution and precipitate onto the surface of the larger aggregates since the smaller aggregates are less energetically favoured. To illustrate the latter description and without loss of generality, let us consider a solid solution with a cubic crystalline structure as depicted in Figure 3.1. The green atom is the most energetically stable atom in the crystalline structure due to its six neighboring atoms. Meanwhile, the blue atoms on the surface are less energetically stable since they are only bounded by five or fewer neighboring atoms. The aggregates compose of more green (interior) atoms are energetically favoured and therefore, more stable. Thus, the most stable structures in the solution are the larger aggregates as they contain more energetically stable atoms. Consequently, as the system tries to minimize its free energy, the less stable

structures, namely the smaller aggregates, tend to dissolve into the solution and precipitate on the surface of the most stable structures. This mechanism shrinks the smaller aggregates and grows the larger ones, a process that increases the overall aggregate size on average in solution. For instance, Figure 3.2 (a) shows an idealised representation of two aggregates and matrix where the small aggregate of the red phase is subject to Ostwald ripening. Eventually, the smaller red aggregate completely dissolves and precipitates leading to the growth of the larger aggregate. Figure 3.2 (b)-(c) portrait the intermediate and final stages of such process, respectively. On the other hand, the Gibbs-Thomson effect relates the changes in the chemical potential associated with the curvature of the interfaces which strongly impact the rates at which the diffusion processes take place (see e.g (4.42) and (5.65)).

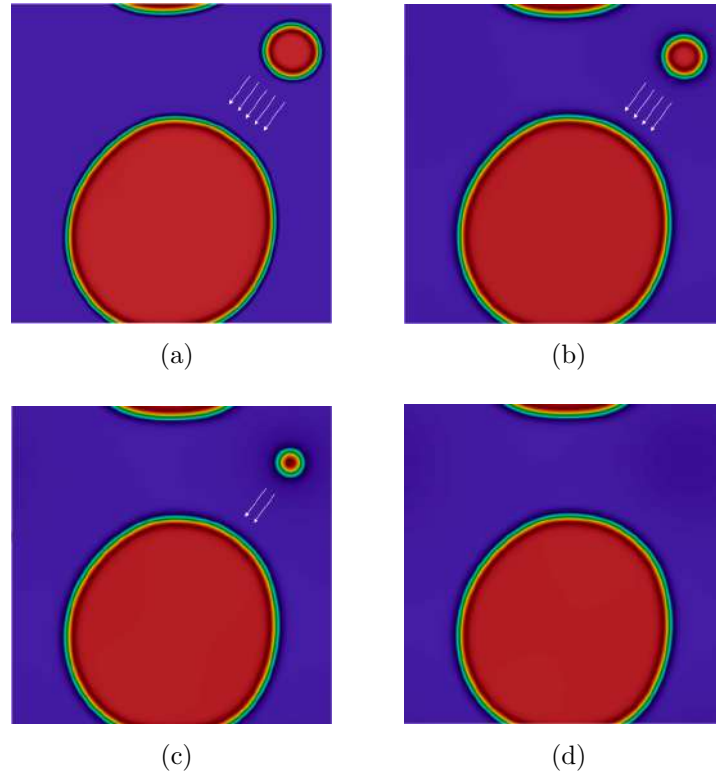


Figure 3.2 (a) depicts an idealised configuration of a solid composed of two aggregates and matrix. The dynamics described by the Ostwald ripening effect will control the dissolution of the small aggregate and eventually its precipitation onto the surface of the larger aggregate once the solution gets supersaturated, moreover (b), (c) and (d) showcase the evolution under such mechanism. Moreover, as the concentration of the smaller inclusion is depleted, the stress field changes and such process drives the final shape of the large inclusion.

3.3 Crystalline structure and mass constraint

To understand the impact of the mechanical and chemical processes on solids requires the description of the nature of solidity and its properties. Gibbs in his pioneering work "On the equilibrium of heterogeneous substances" introduced a theory for the equilibrium thermodynamics of solids under non-hydrostatic conditions where dissolution and accretion at the solid-fluid interfaces is possible [40]. As a particular example, Gibbs's model describes a non-hydrostatic stress distribution at the contact point of a solid with more than one fluid. This pressure induces a different fluid pressure, p^{fluid} , at the solid-fluid interface. The latter implies that the chemical potential of the dissolved solid in each fluid is also different. Nonetheless, the Gibbs's theory does not quantify the internal adjustment in the solid lattice caused by the compositional changes as the concept of solid state diffusion did not exist during Gibbs's time [12, 40, 41]. We now model elastic solids that allow for changes in composition while remaining in the solid state. Consequently, we adopt the network model proposed by Larché and Cahn [12]. This model relies on the idea of a network embedded in the structure of the solid which allows for the definition of a displacement field, and therefore a strain of the solid [10, 33, 35]. As a result, the strain quantifies the network deformation with regard to a undeformed state in the solid. In several natural and engineering materials, such as minerals, polymers, and metals, a solid network can be identified. For instance, the unit cell of the crystalline structure of minerals, which arranges the atoms in a systematic and repeating pattern, acts as a network. We focus on saturated systems, such that

$$\sum_{\alpha=1}^n \varphi^{\alpha} = 1 \quad (3.1)$$

where the order parameter φ^{α} accounts for the concentration of the α -th species (see also (4.6)). When the solid is solely composed of the diffusing species the mass constraint given by (3.1) must hold. Figure 3.3 depicts the crystalline structure of a solid composed of two different species (drawn as the red and blue circles), and it corresponds to the case where adjacent phases have coherent transitions, namely the orientation of their crystalline structure coincides. When a new species grows and nucleates the solid network must account for the lattice misalignment between the phases. According to Larché and Cahn [10, 12, 37, 38], the growth and nucleation of new phases require describing non-coherent phase transitions by defining a crystalline structure and proper orientations of the mechanical properties for each phase. In our framework, the mass transport

and the nucleation and growth of new species induced by chemical reactions generate elastic strains. In Figure 3.3, for instance, the transport of the red atom from the lattice site (1) to (2) must contribute to distort the crystalline structure and therefore, to generate elastic strains. Henceforth, we denote such mechanism is denoted as stress-assisted volume changes. The transport of the red atom from the lattice site (1) to (2) requires the movement of other atoms towards the lattice site (1) since the mass constraint given by (3.1) must always hold. Thus, we restrict ourself to systems where mass transport by vacancies is not feasible.

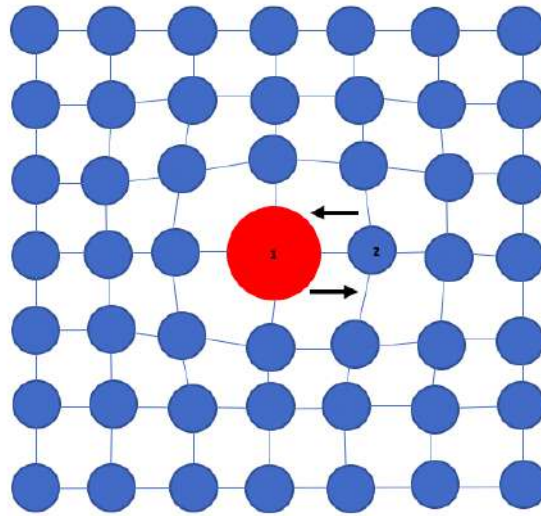


Figure 3.3 depicts the Larché and Cahn representation of the network embedded in the crystalline structure of a solid. The solid is composed of two species sketched as red and blue circles. The figure shows a coherent transition between the phases together with the stress-assisted volume changes mechanism. The transport of the red atom from the lattice site 1 to the lattice site 2 induces volumetric stresses.

3.4 Elastic energy

The elastic energy of a solid defines the potential energy stored in the solid material as work is performed to deform either its volume or shape. External forces applied through the solid boundaries, body forces due to gravity, electric and magnetic fields, thermal swelling/shrinkage, and internal adjustment caused by compositional changes transfer elastic energy to the solid.

The minerals that compose rocks accommodate these processes along their

evolution. Shear zones and overburden are typical examples of external loading applied to a rock. The chemical interactions caused by diffusion and reaction, where atoms arrange to form a material with a crystal structure, are examples of internal adjustment caused by compositional changes. Exhumation of deep crustal metamorphic rocks involves thermal swelling and shrinkage due to the temperature gradient in the crust.

All elastic responses allow the solid to recover its original configuration, namely shape and volume, which implies that the material does not dissipate energy during its mechanical distortion. In our framework, the variations in local species concentration are scaled by a swelling parameter ω which measures the impact of a change in local species concentration on the generation of volumetric stresses. The parameter ω is related to the crystalline structure of the solid and its mechanical properties.

Figure 3.4 depicts the elastic energy $\hat{\psi}^{el}$ as a function of the local species concentration parametrised by the swelling parameter ω for a two phases system. The solid boundaries are fixed, thus the stress variations are only due to the changes of the species concentration. As we can see in Figure 3.4, the elastic energy increases as the swelling parameter becomes larger. Therefore, as long as the local species concentrations change with respect to the initial distribution, the solid undergoes elastic deformation. The interaction between diffusion and deformation change the rates of both processes.

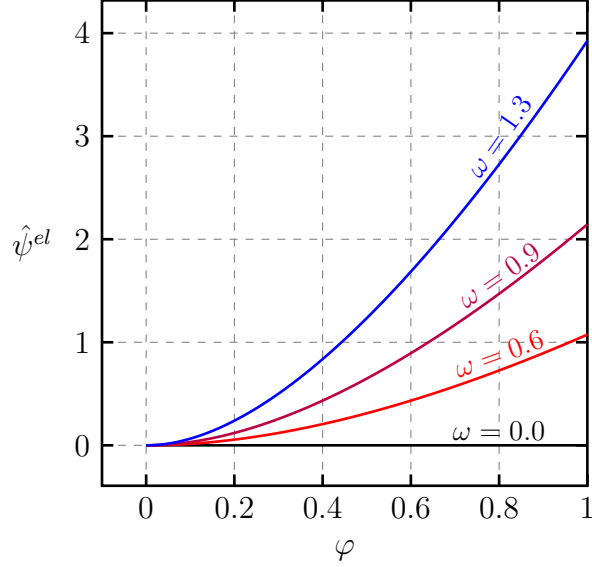


Figure 3.4 shows the elastic energy $\hat{\psi}^{el}$ as a function of the local concentration. The parametrisation shows the effect of the swelling parameter ω on the elastic energy $\hat{\psi}^e$.

3.5 Chemical energy

Solid solutions are complex systems composed of several phases. The phase interfaces may be of non-zero thickness where the physical and chemical properties vary from one phase to another. That is, the transition from one phase to another is not sharp. Figure 3.5 represents two phases A and B, in equilibrium, sketched by the colors blue and red, respectively. The concentration φ of A and B corresponds to φ_A^{eq} and φ_B^{eq} , respectively, and there exists a thin region (color gradient) where the concentration φ varies gradually between φ_A^{eq} and φ_B^{eq} . This region is the interface between the phases A and B. In our formulation of the chemical energy $\hat{\psi}^{ch}$, we allow for microstructure evolution of a system undergoing phase separation processes. The phase separation describes a spontaneous phenomena that occurs at temperatures below the critical one. As a consequence, the system favours the formation of spatial domains rich in either phase. Nevertheless, this chemical energy can also set such that no phase separation processes as a result of interfacial interactions occur. Spinodal decomposition processes can occur in plagioclase feldspars and the binary system magnetite-ulvospinel [42–44]

Conventionally, the chemical energy can be written as $\hat{\psi}^{ch} = \hat{\psi}^\varphi + \hat{\psi}^s$ where $\hat{\psi}^\varphi$ represents the chemical free energy of the homogeneous system and $\hat{\psi}^s$ stands

for an interfacial potential which relates the concentration gradients. Herein, we use the definition of $\hat{\psi}^{ch}$ outlined in [45]. This functional corresponds to an extension towards a multicomponent approach of the classical free energy potential used in the Cahn-Hilliard model [32, 46]. The multicomponent version of the Cahn-Hilliard equation models the microstructure evolution of the solid solution. Figure 3.6 (a) depicts the homogeneous free energy $\hat{\psi}^\varphi$ for three absolute temperature values $T > T_c$, $T = T_c$, and $T < T_c$, respectively. This potential corresponds to the case where two phases compose the solid, for instance, A and B as depicted by Figure 3.5. When the absolute temperature is greater than the critical one (i.e., $T > T_c$), the potential $\hat{\psi}^\varphi$ becomes a convex-downward function of φ which renders a homogeneous mix, as there only exists a single stable state located at the minimum value of $\hat{\psi}^\varphi$. Therefore, for all possible values of concentration, the homogeneous free energy is stable with respect to phase separation. Alternatively, when the absolute temperatures is below the critical temperature $T < T_c$, the homogeneous free energy functional becomes a double-well convex upward function from which two stable coexistent phases emerge where the local minimum value of each well represents the concentration at equilibrium of each phase. Thus, the system favours phase separation. Figure 3.6 (b) showcases the behaviour of the chemical potential calculated as the variational derivative of the free energy $\hat{\psi}^\varphi$ with respect to the phase concentrations φ .

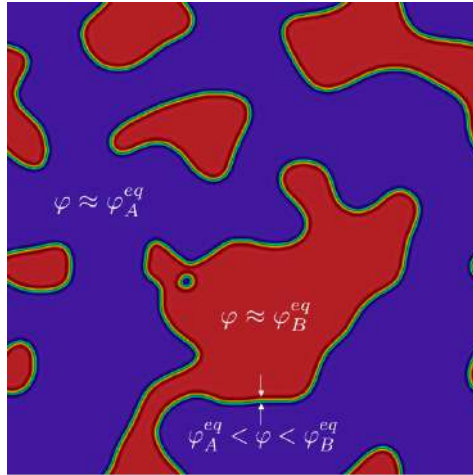


Figure 3.5 shows the microstructure of a solid solution composed of two phases. The concentration of the phases A and B correspond to φ_A^{eq} and φ_B^{eq} , respectively. The interface, where the concentration varies between φ_A^{eq} and φ_B^{eq} , embraces the chemical properties of both the phase A and B.

3.6 Helmholtz free energy, fundamental balance equations and thermodynamic pressure

The evolution of an elastic solid undergoing chemical processes can be characterized by the total free energy of the system. This energy potential accounts for the elastic and chemical energy contributions outlined in Sections 3.4 and 3.5. Hence, the total free energy of the system reads

$$\hat{\Psi} = \hat{\psi}^{ch} + \hat{\psi}^{el}. \quad (3.2)$$

The Helmholtz free energy results from applying the Legendre transform to the internal energy while replacing the entropy of the system by the temperature as an independent variable. To describe the evolution of the solid, we derive a coupled set of chemo-mechanical equations. These equations describe the balances of mass, and linear and angular momenta, for the solid-species solution. Moreover, we describe the dynamics of a non-linear elastic solid undergoing phase separation and chemical reaction by subordinating the constitutive relationships

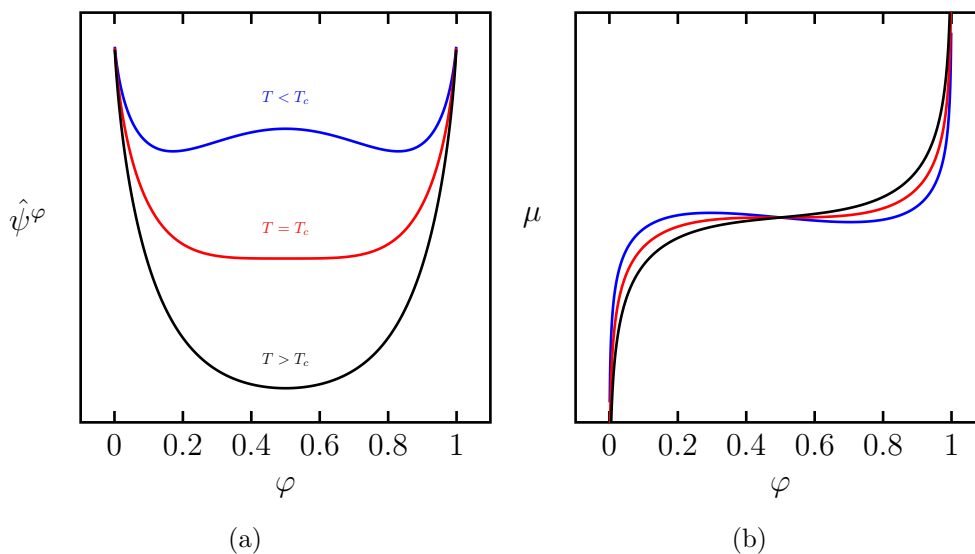


Figure 3.6 (a) represents the free energy potential of the homogeneous system. The double well potential function allows for phase separation where the local minimum value of each well accounts for the concentration at equilibrium of each phase, and (b) sketches the chemical potential as a function of the concentration. By definition, for the multicomponent system, the chemical potentials are the variational derivative of the Helmholtz free energy with respect to the phase concentrations.

to the Helmholtz free energy following the brilliant arguments of Coleman and Noll [47]. We use the aforementioned thermodynamical framework to calculate the chemo-mechanical effects acting on the solid solution and especially to define the thermodynamic pressure that characterizes the thermodynamic equilibrium.

A spike of recent interest in the geosciences literature is the proper definition of the thermodynamic equilibrium in the discussion of the characterization of metamorphic systems. As outlined in chapter §1.1, the thermodynamic pressure can have spatio-temporal inhomogeneities. Recent studies of metamorphic petrology provide the evidence of pressure deviations from the lithostatic values as well as spatially inhomogeneous distributions. Such discrepancies arise from the complex chemomechanical interactions between the minerals which take place deep in the Earth. Conventionally, we assume that the pressure takes the Archimedes's value (directly proportional to the depth). Nevertheless, when considering deforming rocks together with mineral reactions, stresses emerge from both volume changes due to reactions and the overburden which lead to inhomogeneous pressure distributions. Thus, in general, the Archimedes's formula is inaccurate for these systems. For instance, the formation of ultrahigh-pressure rocks suggests that pressure does not always translate into depth [4]. The understanding of the nature of such deviations is crucial since pressure provides, for instance, a constraint for the description of the dynamics of orogens as well as an indirect measurement of the depth history of the sample. The source of such discrepancies is the complex chemo-mechanical interactions as the metamorphic rock complexes evolve towards equilibrium, and most importantly, that both processes are strongly interdependent. Moulas et al. [4] provide a comprehensive review of the evidence that metamorphic rocks maintain and record significant pressure deviations from the lithostatic values. During prograde metamorphism, high pressure and temperature conditions induce the formation of garnet porphyroblasts that harbour quartz and coesite inclusions. As the inclusions grow, the metamorphic system endures large volumetric stresses associated with the expansion of the inclusions in the relaxed host matrix. Eventually, the metamorphic system exhibits chemical zonation where each aggregate has different chemical and mechanical properties. Such heterogeneity generates spatial variations in pressure. The effect of the inhomogeneous pressure seems to be critical and will allow us to calibrate geodynamics models as well as to describe the evolution of fabrics and microstructures.

Previous studies of metamorphic rocks separated the chemical and the me-

chanical actions on the mineral assemblages. This splitting is inappropriate as the volume changes, induced by chemical interactions between minerals, strongly influence the inhomogeneous pressure distribution. Thus, an appropriate description of the deformation process requires a comprehensive treatment of the coupled chemo-mechanical interactions.

As mentioned above, the thermodynamic pressure is defined as the partial derivative of the Helmholtz free energy with respect to the specific volume while keeping the local concentration and deformation constant. This physical quantity defines the chemical equilibrium when all dissipative processes, which produce entropy and therefore variations in local composition, cease [14]. Thereby, the thermodynamic pressure defines the steady state where the free energy potential $\hat{\psi}$ becomes constant [14, 40].

Chapter 4

Derivation of a multicomponent reactive Cahn-Hilliard equation

We derive a thermodynamically consistent continuum theory for the multicomponent Cahn–Hilliard equations following the ideas introduced by Fried & Gurtin [48–50] and accounting for multiple chemical reactions as introduced by Gurtin & Vargas [51]. To this end, we construct our theory by considering multiple balances of microforces augmented by multiple mass balance equations within an extended Larché–Cahn framework. We also remark how to proceed to derive our theory by postulating the principle of virtual power. As for the Larché–Cahn framework, we incorporate into the theory the Larché–Cahn derivatives with respect to the phase fields and their gradients. We also show the implications of constraining the gradients of the phase fields into the gradient energy coefficients. Moreover, we derive the configurational balance with all the associated configurational fields which are also in agreement with the Larché–Cahn framework. Particularly, we study solutions whose microstructural evolution depends upon the reaction-diffusion interactions and analyze the underlying configurational fields. We introduce how interleaving between the reaction and diffusion processes and their relation with the configurational tractions drive the motion of interfaces.

4.1 Introduction

The Cahn and Hilliard phase field framework captures the dynamics of spontaneous phase separation as the temperature of the system goes below the critical temperature. After the separation process, the dynamics forms spatial domains of fully separated components. This phase field successfully models cancerous tumour growth [29, 52–54], viscous fingering [55], alloys [56], and image inpainting [57].

Multicomponent systems are ubiquitous in nature, from rocks composed of several minerals to biological mixtures such as the cytosol [58, 59]. Diffusive models are commonly used to describe multicomponent systems driven by phase segregation [60–64]. The theoretical foundations of the multicomponent Cahn–Hilliard framework can be traced back to Morral & Cahn [65] in the study of the dynamics of ternary alloys. Shortly after, de Fontaine [66] analyzed the kinetics of clustering and ordering in multi-phase solid solutions. In particular, de Fontaine [66] uses the same gradient energy as the one introduced by Morral & Cahn [65]. In alloy manufacturing, the multicomponent Cahn–Hilliard framework has been used to understand the microstructural evolution of primary alloys where their microstructures are composed of multiple phases [56, 67–69].

Thus, the multicomponent Cahn-Hilliard model emerged as a promising tool to study the kinetics of multi-phase systems undergoing phase separation processes. In particular, the strength of the model relies on an order parameter which implicitly tracks the microstructure evolution of the phases. The latter allows, for example, to enhance material properties (see e.g. [45] and references therein). Nevertheless, the aforementioned framework has significant drawbacks regarding the solution of the resulting system of equations, which in turns makes it also attractive for computational scientists. For instance, Boyanova & Neytcheva [70] design preconditioners to solve the n-components algebraic system using a quasi-Newton method for the multicomponent Cahn–Hilliard equations. Honjo & Saito [56] carry out numerical simulations to investigate the microstructural evolution of Fe–Cr–Mo ternary alloys. Clavijo et al. [45] coupled the multicomponent Cahn–Hilliard model with a general law of mass action to study the interleaving between spinodal decomposition processes and chemical reactions. Clavijo et al. [45] models the phase separation process of a four phases system as a reversible chemical reaction between the phases takes place.

Elliott & Garke [46] approached the underlying physical system by employing the balance of masses and the thermodynamical definition of chemical potential as did Conti et al. [71] and Clavijo et al. [45]. Conversely, Fried & Gurtin [49] and Miranville & Schimperna [72] employed multiple balances of microforces; however, the Larché–Cahn derivatives were not considered. To describe the underlying physics of this problem, we consider n -phase fields representing the concentration of conserved species and use a set of coupled Cahn–Hilliard equations to model these phenomena. This leads to a system of n degenerate nonlinear fourth-order parabolic partial differential equations. The degeneracy comes from a nonlinear mobility tensor depending on the phase fields, which can vanish depending on the values of the phase fields. We assume that there exist n balances of microforces, as proposed by Fried & Gurtin [48, 49], and n mass balances accounting for chemical reactions. We then build an extended Larché–Cahn framework to account for the interdependence between the conserved species. Given the set $\varphi = \{\varphi^1, \dots, \varphi^n\}$ of species, where $n \in \mathbb{N}$, we consider $\tilde{\varphi} = \varphi \setminus \{\varphi^\sigma\}$ to redefine a generic conserved species by constraining it, $\varphi^\sigma := \mathcal{M}_0(\tilde{\varphi})$ as well as its gradient, $\text{grad}\varphi^\sigma := \mathcal{M}_1(\text{grad}\tilde{\varphi})$. A key aspect of this theory is that in computing partial derivatives with respect to φ^α and $\text{grad}\varphi^\alpha$, the mappings $\mathcal{M}_0: \tilde{\varphi} \mapsto \varphi^\sigma$ and $\mathcal{M}_1: \text{grad}\tilde{\varphi} \mapsto \text{grad}\varphi^\sigma$ must be taken into account. We then use the definition of the partial derivative of generic functions $\mathcal{F}(\varphi)$ and $\mathcal{G}(\text{grad}\varphi)$ where φ^σ is constrained to derive the multicomponent Cahn–Hilliard equations. Moreover, in defining these partial derivatives, we arrive at a *constrained* inner product on a constrained space to appropriately define the gradient energy coefficients $\Gamma^{\alpha\beta}$.

The outline of this chapter is structured as follows. In section §4.2, we introduce the balances of microforces augmented by the mass balances, and later, we postulate the principle of virtual powers as an equivalent way of obtaining the balances of microforces. We complement the system of equations by deriving the first and second law of thermodynamics. We also present the concept of the Larché–Cahn derivative, including functions depending not only on the phase fields but also on their gradients, and show the implications of constraining the gradients of the phase fields into the gradient energy coefficients. In §4.3, we impose the thermodynamical constraints to obtain the constitutive equations related to every kinematic process. We conclude this section by defining how the chemical reactions in ideal and non ideal solutions contribute as an internal mass supply. In section §4.4, we derive the configurational set of forces that drive the evolution of the interfaces and its configurational balance. In section §4.5, we

non-dimensionalize the equations. Finally, in section §4.6, we propose a energetic variational approach to derive the multicomponent Cahn–Hilliard system.

4.2 Fundamental balances and thermodynamic laws

4.2.1 Balances of masses and microforces

Herein, \mathcal{B} represents a three-dimensional point space \mathcal{E} of a fixed region and \mathcal{P} is an arbitrarily fixed subregion of \mathcal{B} with boundary $\mathcal{S} = \partial\mathcal{P}$ oriented by an outward unit normal \mathbf{n} .

Let φ^α be the order parameter of the α -th species in a system of n components. The order parameter represents the concentration

$$\varphi^\alpha := \varrho^\alpha / \varrho, \quad (4.1)$$

where ϱ^α is the density of the α -th species while ϱ is the total density. We restrict attention to the case where the phase field represents the concentration of a conserved species with a mass flux \mathbf{j}^α endowed of a mass supply s^α . The mass supply is composed by two terms, an external contribution due to external agents and an internal contributions due to chemical reactions. Thus,

$$s^\alpha := s_{\text{int}}^\alpha + s_{\text{ext}}^\alpha. \quad (4.2)$$

The partwise species balances are given by

$$\overline{\int_{\mathcal{P}} \varphi^\alpha dv} = \int_{\mathcal{P}} s^\alpha dv - \int_{\mathcal{S}} \mathbf{j}^\alpha \cdot \mathbf{n} da, \quad (4.3)$$

and by localizing it, we arrive at the pointwise version of the the temporal evolution of the mass conservation of the α -th species

$$\dot{\varphi}^\alpha = s^\alpha - \text{div} \mathbf{j}^\alpha. \quad (4.4)$$

By construction (4.1), the sum of all concentrations equals one,

$$\sum_{\alpha=1}^n \varphi^\alpha = 1, \quad (4.5)$$

which yields the following kinematical relations after computing the time and spatial derivatives,

$$\sum_{\alpha=1}^n \dot{\varphi}^\alpha = 0, \quad \wedge \quad \sum_{\alpha=1}^n \text{grad } \varphi^\alpha = 0. \quad (4.6)$$

Moreover, to conserve mass, from the sum of all balances (4.3), the additional kinematical constraint are obtained

$$\sum_{\alpha=1}^n \mathbf{j}^\alpha = 0, \quad \wedge \quad \sum_{\alpha=1}^n s^\alpha = 0. \quad (4.7)$$

To define appropriately the concept of partial derivatives, we take into account (4.5) and (4.6) to derive this theory.

We then augment the species balances (4.3) and (4.4) by a microforce balance for each species. To do so, let $\boldsymbol{\xi}^\alpha$ be the α -th microstress, and π^α (γ^α) field is the α -th internal (external) microforce [50]. Thus, the microforce balances in their partwise form are

$$\int_{\mathcal{S}} \boldsymbol{\xi}^\alpha \cdot \mathbf{n} \, da + \int_{\mathcal{P}} (\pi^\alpha + \gamma^\alpha) \, dv = 0, \quad (4.8)$$

where its pointwise version is obtained by localizing (4.8) to arrive at

$$\text{div } \boldsymbol{\xi}^\alpha + \pi^\alpha + \gamma^\alpha = 0. \quad (4.9)$$

4.2.2 Thermodynamics

We follow Gurtin & Fried [50, 73–75] and separate conservation statements from constitutive equations.

To describe the thermodynamics of this system, we introduce the power expenditure \mathcal{W}_{ext} externally to \mathcal{P} done by the external microforces on \mathcal{P} and microtractions on \mathcal{S}

$$\mathcal{W}_{\text{ext}}(\mathcal{P}) := \sum_{\alpha=1}^n \left\{ \int_{\mathcal{P}} \gamma^\alpha \dot{\varphi}^\alpha \, dv + \int_{\mathcal{S}} \xi_{\mathcal{S}}^\alpha \dot{\varphi}^\alpha \, da \right\}, \quad (4.10)$$

where n stands for the total number of species and $\xi_{\mathcal{S}}^\alpha = \boldsymbol{\xi}^\alpha \cdot \mathbf{n}$ is the α -th microtraction.

The first law of thermodynamics balances the internal energy of the system and the power expenditure of chemical energy resulting from the reaction-

diffusion process. Conversely, the mechanical version of the second law of thermodynamics describes the irreversibility of the process. We then present these two laws as

$$\left. \begin{aligned} \overline{\int_{\mathcal{P}} \varepsilon \, dv} &= \mathcal{W}_{\text{ext}}(\mathcal{P}) - \int_S \mathbf{q} \cdot \mathbf{n} \, da + \int_{\mathcal{P}} r \, dv \\ &+ \sum_{\alpha=1}^n \left\{ - \int_S \mu^\alpha \mathbf{j}^\alpha \cdot \mathbf{n} \, da + \int_{\mathcal{P}} \mu^\alpha s_{\text{ext}}^\alpha \, dv \right\}, \\ \overline{\int_{\mathcal{P}} \eta \, dv} &\geq - \int_S \frac{\mathbf{q}}{\vartheta} \cdot \mathbf{n} \, da + \int_{\mathcal{P}} \frac{r}{\vartheta} \, dv, \end{aligned} \right\} \quad (4.11)$$

where ε and η represent the internal-energy density and entropy density, \mathbf{q} is the heat flux, r is the heat supply, and $\vartheta > 0$ is the absolute temperature. Note that there is no contribution of s_{int}^α to the energy balance (4.11).

Using the external power expenditure (4.10), the microforce balance (4.9), the mass balance (4.3), and the mass supply definition (4.2), the thermodynamic laws (4.11) are localized

$$\left. \begin{aligned} \dot{\varepsilon} &= \sum_{\alpha=1}^n \left\{ -\pi^\alpha \dot{\varphi}^\alpha + \boldsymbol{\xi}^\alpha \cdot \text{grad } \dot{\varphi}^\alpha - \mathbf{j}^\alpha \cdot \text{grad } \mu^\alpha - \mu^\alpha s_{\text{int}}^\alpha \right\} - \text{div } \mathbf{q} + r, \\ \dot{\eta} &\geq -\text{div } \frac{\mathbf{q}}{\vartheta} + \frac{r}{\vartheta}. \end{aligned} \right\} \quad (4.12)$$

Rewriting (4.12)₂, we obtain

$$\dot{\eta} \geq -\frac{1}{\vartheta} \text{div } \mathbf{q} + \frac{1}{\vartheta^2} \mathbf{q} \cdot \text{grad } \vartheta + \frac{r}{\vartheta}. \quad (4.13)$$

With the definition of the free-energy density as

$$\psi := \varepsilon - \vartheta \eta, \quad (4.14)$$

and after multiplying (4.13) by ϑ and subtracting it from (4.12)₁, we arrive at the pointwise free-energy imbalance as

$$\begin{aligned} \dot{\psi} + \dot{\vartheta} \eta + \sum_{\alpha=1}^n \left\{ (\pi^\alpha - \mu^\alpha) \dot{\varphi}^\alpha - \boldsymbol{\xi}^\alpha \cdot \text{grad } \dot{\varphi}^\alpha + \mathbf{j}^\alpha \cdot \text{grad } \mu^\alpha + \mu^\alpha s_{\text{int}}^\alpha \right\} \\ + \frac{1}{\vartheta} \mathbf{q} \cdot \text{grad } \vartheta \leq 0. \end{aligned} \quad (4.15)$$

Remark 1 (Alternative derivation—Principle of virtual powers). *The virtual power expenditure definition encompasses, internally to \mathcal{P} , the power done by*

internal microforces and the microstresses on \mathcal{P} , whereas, externally to \mathcal{P} , the power done by external microforces on \mathcal{P} and microtractions on \mathcal{S} , implying

$$\mathcal{V}_{\text{int}}(\mathcal{P}, \chi^\alpha) = \mathcal{V}_{\text{ext}}(\mathcal{P}; \chi^\alpha) \quad (4.16)$$

where the internal and external virtual powers are given by

$$\mathcal{V}_{\text{int}}(\mathcal{P}; \chi^\alpha) := \sum_{\alpha=1}^n \left\{ \int_{\mathcal{P}} (-\pi^\alpha \chi^\alpha + \boldsymbol{\xi}^\alpha \cdot \text{grad } \chi^\alpha) dv \right\}, \quad (4.17)$$

and

$$\mathcal{V}_{\text{ext}}(\mathcal{P}; \chi^\alpha) := \sum_{\alpha=1}^n \left\{ \int_{\mathcal{P}} \gamma^\alpha \chi^\alpha dv + \int_{\mathcal{S}} \xi_S^\alpha \chi^\alpha da \right\}, \quad (4.18)$$

where $\{\chi^\alpha\}$ is a set of n kinematically admissible fields.

Finally, we apply the divergence theorem to (4.16) and by means of the variational arguments, we get the local balance of microforces (4.9).

4.2.3 Larché–Cahn derivatives

We adopt the notation suggested by Gurtin *et al.* [33, 50] for the Larché–Cahn derivatives in a multicomponent constrained framework. Thus, Let

$$\boldsymbol{\varphi} = \{\varphi^1, \dots, \varphi^n\} \quad (4.19)$$

be a list of the species concentrations. Moreover, assume that the function \mathcal{F} depends on $\boldsymbol{\varphi}$ such that

$$\mathcal{F}(\boldsymbol{\varphi}) = \mathcal{F}(\varphi^1, \dots, \varphi^n). \quad (4.20)$$

The constraint given by (4.5) implies that the set of concentrations $\boldsymbol{\varphi}$ must be admissible; namely, $0 < \varphi^\alpha < 1$. Hence, since varying one of the concentrations φ^α when holding the others fixed violates the constrain (4.5), conventional partial differential operations are not well-defined on functions such as f . Larché and Cahn [38] overcame this issue by defining the following operation

$$\frac{\partial^{(\sigma)} \mathcal{F}(\boldsymbol{\varphi})}{\partial \varphi^\alpha} = \left. \frac{d}{d\epsilon} \mathcal{F}(\varphi^1, \dots, \varphi^\alpha + \epsilon, \dots, \varphi^\sigma - \epsilon, \dots, \varphi^n) \right|_{\epsilon=0}. \quad (4.21)$$

As shown in (4.21), Larché and Cahn chose two reference concentrations φ^α and φ^σ in the set of variables. An infinitesimal change ϵ in φ^α has to induce the

same infinitesimal variation ϵ onto φ^σ when holding the others unchanged. As a consequence of (4.5), the concentration φ^σ , in general, is expressed by

$$\varphi^\sigma = 1 - \sum_{\substack{\alpha=1 \\ \alpha \neq \sigma}}^n \varphi^\alpha. \quad (4.22)$$

The operation given by (4.21) implies the variation of $\mathcal{F}(\boldsymbol{\varphi})$ caused by an increase in the concentration of the α -th species which in turn generates a decrease in the σ -th species concentration. Due to (4.21), we find the following relations

$$\frac{\partial^{(\sigma)} \mathcal{F}(\boldsymbol{\varphi})}{\partial \varphi^\sigma} = 0, \quad (4.23)$$

and the skew-symmetric relation

$$\frac{\partial^{(\sigma)} \mathcal{F}(\boldsymbol{\varphi})}{\partial \varphi^\alpha} = - \frac{\partial^{(\alpha)} \mathcal{F}(\boldsymbol{\varphi})}{\partial \varphi^\sigma}. \quad (4.24)$$

Following the same process, taking the gradient of (4.22) we arrive at

$$\text{grad } \varphi^\sigma = - \sum_{\substack{\alpha=1 \\ \alpha \neq \sigma}}^n \text{grad } \varphi^\alpha. \quad (4.25)$$

We thus define the function

$$\mathcal{G}(\text{grad } \boldsymbol{\varphi}) = \mathcal{G}(\text{grad } \varphi^1, \dots, \text{grad } \varphi^n), \quad (4.26)$$

and its Larché–Cahn derivative

$$\begin{aligned} \frac{\partial^{(\sigma)} \mathcal{G}(\text{grad } \boldsymbol{\varphi})}{\partial (\text{grad } \varphi^\alpha)} = \\ \frac{d}{d\boldsymbol{\epsilon}} \mathcal{G}(\text{grad } \varphi^1, \dots, \text{grad } \varphi^\alpha + \boldsymbol{\epsilon}, \dots, \text{grad } \varphi^\sigma - \boldsymbol{\epsilon}, \dots, \text{grad } \varphi^n) \Big|_{\boldsymbol{\epsilon}=\mathbf{0}}, \end{aligned} \quad (4.27)$$

where the relations (4.23) and (4.24) specialize to

$$\frac{\partial^{(\sigma)} \mathcal{G}(\text{grad } \boldsymbol{\varphi})}{\partial (\text{grad } \varphi^\sigma)} = 0 \quad \wedge \quad \frac{\partial^{(\sigma)} \mathcal{G}(\text{grad } \boldsymbol{\varphi})}{\partial (\text{grad } \varphi^\alpha)} = - \frac{\partial^{(\alpha)} \mathcal{G}(\text{grad } \boldsymbol{\varphi})}{\partial (\text{grad } \varphi^\sigma)}. \quad (4.28)$$

In Cahn–Hilliard systems of multicomponents, we incorporate gradient energy coefficients $\Gamma^{\alpha\beta}$ into the free-energy definition, and obtain a free-energy density in the following form

$$\hat{\psi}(\boldsymbol{\varphi}, \text{grad } \boldsymbol{\varphi}) := f(\boldsymbol{\varphi}) + \sum_{\alpha=1}^n \sum_{\beta=1}^n \Gamma^{\alpha\beta} \text{grad } \varphi^\alpha \cdot \text{grad } \varphi^\beta. \quad (4.29)$$

Elliott & Garcke in [46] prove that for multicomponent systems to be well-posed, it is sufficient to ensure the positive definiteness of $\Gamma^{\alpha\beta}$. We show that this condition is, in fact, sufficient but not necessary.

To do so, we define a *special* inner product on a constrained space. Consider a set vectors $\{\mathbf{p}^\alpha\}$ constrained by

$$\sum_{\alpha=1}^n \mathbf{p}^\alpha = \mathbf{0}, \quad (4.30)$$

with the inner product

$$\sum_{\alpha=1}^n \sum_{\beta=1}^n \Gamma^{\alpha\beta} \mathbf{p}^\alpha \cdot \mathbf{p}^\beta. \quad (4.31)$$

We now consider the following points:

1. Let each $\Lambda^{\alpha\beta}$ be a matrix populated with the same entry κ . Thus, $\{\mathbf{p}^\alpha\}$ is the null space of $\Lambda^{\alpha\beta}$ given the constraint (4.30), i.e., $\text{Null}(\Lambda^{\alpha\beta}) = \{\mathbf{p}^\alpha\}$. Moreover, if the rows of $\Lambda^{\alpha\beta}$ are populated with the same entry κ^β , we arrive at the same conclusion. For any of these cases, we have that

$$\sum_{\alpha=1}^n \sum_{\beta=1}^n \Gamma^{\alpha\beta} \mathbf{p}^\alpha \cdot \mathbf{p}^\beta = \sum_{\alpha=1}^n \sum_{\beta=1}^n (\Gamma^{\alpha\beta} + \Lambda^{\alpha\beta}) \mathbf{p}^\alpha \cdot \mathbf{p}^\beta. \quad (4.32)$$

Moreover, if we use the mass constraint (4.30) with the σ -th species as the dependent species and quadratic form (4.31), we arrive at

$$\sum_{\alpha=1}^n \sum_{\beta=1}^n \Gamma^{\alpha\beta} \mathbf{p}^\alpha \cdot \mathbf{p}^\beta = \sum_{\substack{\alpha=1 \\ \alpha \neq \sigma}}^n \sum_{\substack{\beta=1 \\ \beta \neq \sigma}}^n \underbrace{(\Gamma^{\alpha\beta} + \Gamma^{\sigma\sigma} - \Gamma^{\alpha\sigma} - \Gamma^{\sigma\beta})}_{\Gamma_\sigma^{\alpha\beta}} \mathbf{p}^\alpha \cdot \mathbf{p}^\beta. \quad (4.33)$$

Finally, we obtain a dimension $n - 1$ unconstrained space with the *non-invertible mapping* $\mathcal{H} : \Gamma^{\alpha\beta} \mapsto \Gamma_\sigma^{\alpha\beta}$ given by

$$\Gamma_\sigma^{\alpha\beta} := \Gamma^{\alpha\beta} + \Gamma^{\sigma\sigma} - \Gamma^{\alpha\sigma} - \Gamma^{\sigma\beta}. \quad (4.34)$$

We thus postulate that the problem is well-posed if $\Gamma_\sigma^{\alpha\beta}$ is positive-definite. Moreover, $\Gamma^{\alpha\beta}$ can be negative-definite without compromising the well posedness of the problem.

2. Let \mathbf{e}^α be the standard canonical basis in dimension n and $\Gamma^{\alpha\beta}$ be a diagonal matrix such that

$$\Gamma^{\alpha\beta} = \kappa \mathbf{e}^\alpha \cdot \mathbf{e}^\beta. \quad (4.35)$$

It follows from point 1 that $\Gamma^{\alpha\beta}$ can be rewritten as

$$\Gamma^{\alpha\beta} = -\kappa(1 - \mathbf{e}^\alpha \cdot \mathbf{e}^\beta). \quad (4.36)$$

The null-diagonal matrix maps all vector in a similar fashion than the diagonal matrix (4.35) which captures the mass constraint (4.30).

3. $\Gamma^{\alpha\beta} \text{grad} \varphi^\alpha \cdot \text{grad} \varphi^\beta$ describes the interfacial energy for the α -th and β -th species, therefore it is meaningless to consider the interaction term $\Gamma^{\alpha\alpha} |\text{grad} \varphi^\alpha|^2$ as non-zero. By assuming $\Gamma^{\alpha\beta}$ diagonal, we specify the interfacial interactions of a certain phase with itself as well as that all the interactions between any two phases is the same.

Through what follows in this chapter, we denote relative quantities with a subscript, for vector-like $(\cdot)_\sigma^\alpha := (\cdot)^\alpha - (\cdot)^\sigma$ and tensor-like $(\cdot)_\sigma^{\alpha\beta} := (\cdot)^{\alpha\beta} - (\cdot)^\sigma$ quantities. Additionally, to avoid confusion, we do not use Einstein's summation when two indices are contracted.

4.3 Constitutive equations

4.3.1 Thermodynamical constraints

Throughout the derivation of the constitutive relations for the multicomponent Cahn–Hilliard system, we make use of the Larché–Cahn derivative expressed by (4.21) and (4.27). We now use the Coleman–Noll procedure [76] to find the sufficient conditions to ensure the inequality (4.15) by arbitrary fields. Thus, a set of constitutive equations emerges as a pair of each kinematic process. We assume the following constitutive dependency of the free energy ψ within the context of isothermal processes

$$\psi := \hat{\psi}(\boldsymbol{\varphi}, \text{grad} \boldsymbol{\varphi}). \quad (4.37)$$

We thus rewrite the free-energy (4.15) as follows

$$\begin{aligned} & \sum_{\alpha=1}^n \left\{ \mu^\alpha - \pi^\alpha - \frac{\partial^{(\sigma)} \hat{\psi}}{\partial \varphi^\alpha} \right\} \dot{\varphi}^\alpha + \sum_{\alpha=1}^n \left\{ \boldsymbol{\xi}^\alpha - \frac{\partial^{(\sigma)} \hat{\psi}}{\partial (\text{grad} \varphi^\alpha)} \right\} \cdot \text{grad} \dot{\varphi}^\alpha \\ & - \sum_{\alpha=1}^n \{ \boldsymbol{j}^\alpha \cdot \text{grad} \mu^\alpha + \mu^\alpha s_{\text{int}}^\alpha \} \leq 0. \end{aligned} \quad (4.38)$$

The free-energy imbalance (4.38) must hold for any arbitrary $\dot{\varphi}^\alpha$, $\text{grad } \dot{\varphi}^\alpha$, and $\text{grad } \mu^\alpha$ fields at a given time and position. Thus, the following relations must hold

$$\pi_\sigma^\alpha = \mu_\sigma^\alpha - \frac{\partial^{(\sigma)} \hat{\psi}}{\partial \varphi^\alpha}, \quad (4.39a)$$

$$\boldsymbol{\xi}_\sigma^\alpha = \frac{\partial^{(\sigma)} \hat{\psi}}{\partial (\text{grad } \varphi^\alpha)}, \quad (4.39b)$$

$$\boldsymbol{j}_\sigma^\alpha = - \sum_{\beta=1}^n \boldsymbol{M}^{\alpha\beta} \text{grad } \mu_\sigma^\beta, \quad (4.39c)$$

where \boldsymbol{M} is the mobility tensor, which must be positive definite, $\sum_{\alpha=1}^n \sum_{\beta=1}^n \boldsymbol{p}^\alpha \cdot \boldsymbol{M}^{\alpha\beta} \boldsymbol{p}^\beta$ holding $\forall \boldsymbol{p}$. Aside from the fact that (4.38) expresses the possible thermodynamically consistent choices, the terms $\pi^\alpha := \pi_\sigma^\alpha$, $\mu^\alpha := \mu_\sigma^\alpha$, and $\boldsymbol{\xi}^\alpha := \boldsymbol{\xi}_\sigma^\alpha$ are written in the Larché–Cahn sense given their explicit dependence on the Larché–Cahn derivatives. As a byproduct, we also write the mass flux, $\boldsymbol{j}^\alpha := \boldsymbol{j}_\sigma^\alpha(\mathbf{x}, t; \text{grad } \mu_\sigma^\alpha)$, and the surface microtraction, $\xi_s^\alpha := \xi_{s\sigma}^\alpha(\mathbf{x}, t; \boldsymbol{\xi}_\sigma^\alpha)$ in the Larché–Cahn sense. Finally, all these quantities are relative to the σ -th species.

An essential consequence of (4.5) is the definition of the relative chemical potential $\mu_\sigma^\alpha = \mu^\alpha - \mu^\sigma$. According to Larché–Cahn [38], the relative chemical potential expresses the chemical potential of α -th species measured relatively to the chemical potential of σ -th species. This construction is then extended to define the relative fields: π_σ^α , $\boldsymbol{j}_\sigma^\alpha$, $\boldsymbol{\xi}_\sigma^\alpha$, and $\xi_{s\sigma}^\alpha$.

Using guidance from the original Cahn–Hilliard equation [32], the Ginzburg–Landau potential governs spontaneous phase separation processes such as spinodal decomposition. In a multicomponent framework, to determine the constitutive relations in (4.39), the Ginzburg–Landau potential is expressed as

$$\begin{aligned} \hat{\psi}(\boldsymbol{\varphi}, \text{grad } \boldsymbol{\varphi}) &= N_v k_B \vartheta \left(\sum_{\alpha=1}^n \varphi^\alpha \ln \varphi^\alpha \right) + N_v \sum_{\alpha=1}^n \sum_{\beta=1}^n \Omega^{\alpha\beta} \varphi^\alpha \varphi^\beta \\ &+ \frac{1}{2} \sum_{\alpha=1}^n \sum_{\beta=1}^n \Gamma^{\alpha\beta} \text{grad } \varphi^\alpha \cdot \text{grad } \varphi^\beta, \end{aligned} \quad (4.40)$$

where N_v is the amount of molecules stored in the system per unit volume, $\Omega^{\alpha\beta}$ describes the reciprocal interaction energy between the α -th and β -th species, and k_B is the Boltzmann constant. Since the interaction energy between the α -th and β -th species is reciprocal, $\Omega^{\alpha\beta}$ has to be a symmetric tensor. Furthermore, the interaction energy is a positive-definite tensor which is expressed as a function

of the critical temperature between the α -th and the β -th species, $\vartheta_c^{\alpha\beta}$. We assume a non-energetic interaction when $\alpha = \beta$ which entails that $\Omega^{\alpha\beta} = 0$. On the contrary, for different species $\alpha \neq \beta$, we adopt that $\Omega^{\alpha\beta} = 2k_B\vartheta_c^{\alpha\beta}$ [32, 46, 77]. We express $\Gamma^{\alpha\beta} = \sigma^{\alpha\beta}\ell^{\alpha\beta}$ (no Einstein notation) as the interfacial energy magnitud between the α -th and β -th species where $\sigma^{\alpha\beta}$ and $\ell^{\alpha\beta}$ represent the interfacial tension and the interfacial thickness ¹ between the α -th and the β -th species, respectively. Cahn and Hilliard express the interfacial energy force as $\Gamma^{\alpha\beta} = N_v\Omega^{\alpha\beta}(\ell^{\alpha\beta})^2$ [32].

By combining the expression (4.39a) in conjunction with the balance of conservation of microforces (4.9) and given the constitutive relation for the free energy (4.40), the relative chemical potential of the α -th species in the Larcé–Cahn sense can be expressed as

$$\mu_\sigma^\alpha = \frac{\partial^{(\sigma)}\hat{\psi}}{\partial\varphi^\alpha} - \operatorname{div} \frac{\partial^{(\sigma)}\hat{\psi}}{\partial(\operatorname{grad}\varphi^\alpha)} - (\gamma^\alpha + \gamma^\sigma), \quad (4.41)$$

and therefore (4.41) with (4.40) specializes to

$$\begin{aligned} \mu_\sigma^\alpha &= N_vk_B\vartheta \left(\ln \frac{\varphi^\alpha}{\varphi^\sigma} \right) + 2N_v \sum_{\beta=1}^n (\Omega^{\alpha\beta} - \Omega^{\sigma\beta})\varphi^\beta \\ &\quad - \sum_{\beta=1}^n (\Gamma^{\alpha\beta} - \Gamma^{\sigma\beta}) \operatorname{div} \operatorname{grad} \varphi^\beta - (\gamma^\alpha + \gamma^\sigma). \end{aligned} \quad (4.42)$$

In the following, we use the Onsager reciprocal relations of an isotropic symmetric mobility tensor $\mathbf{M}^{\alpha\beta} = M^{\alpha\beta} \mathbf{1}$ (off-diagonals terms). We calculate the mobility coefficients as a function of the species concentration. Particularly, we calculate such a dependency as $M^{\alpha\beta} := M_0^{\alpha\beta} \varphi^\alpha (\delta^{\alpha\beta} - \varphi^\beta)$ where $\delta^{\alpha\beta}$ is the Kronecker delta of dimension n and $M_0^{\alpha\beta}$ is the mobility between the α and β species (no sum on α and β). The dimensions of $\mathbf{M}^{\alpha\beta}$ are length⁴ per unit force and time [46]. Thus, (4.7)₁ implies the following relation

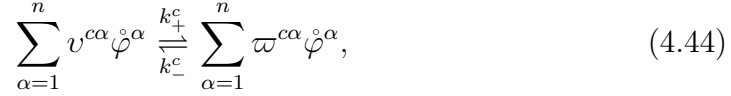
$$\sum_{\beta=1}^n M^{\alpha\beta} = 0, \quad \forall \alpha. \quad (4.43)$$

4.3.2 Chemical reaction in ideal solutions

In this section, we restrict our attention to ideal solutions and recall the rigorous treatment by Bowen [78]. Denoting the species $\dot{\varphi}$ related to the concentration φ ,

¹Cahn and Hilliard suggested that this relation is the root mean square effective interaction distance [32].

such that $\varphi := [\dot{\varphi}]$, we express the c -th chemical reaction in a set of n_s chemical reactions, $n_s \in \mathbb{N}$, as



where $v^{c\alpha}$ and $\varpi^{c\alpha}$ are the stoichiometry coefficients corresponding to the α -th species reacting in the c -th chemical reaction. The c -th forward reaction rate is denoted by k_+^c , while the c -th backward one is k_-^c . Furthermore, the c -th velocities of both the forward and backward reactions read

$$r_+^c := k_+^c \prod_{\alpha=1}^n (\varphi^\alpha)^{v^{c\alpha}}, \quad (4.45)$$

$$r_-^c := k_-^c \prod_{\alpha=1}^n (\varphi^\alpha)^{\varpi^{c\alpha}}. \quad (4.46)$$

Finally, the internal rate of mass supply term for all n_s chemical reactions that enters in (4.4) of an ideal solution is given by

$$s_{\text{int}}^\alpha := - \sum_{c=1}^{n_s} (v^{c\alpha} - \varpi^{c\alpha}) (r_+^c - r_-^c). \quad (4.47)$$

Rigorously, the total number m of possible chemical reactions, where $m \geq n_s \in \mathbb{N}$, is not arbitrary. To fit our framework in Bowen's treatment [78], we recall the indestructibility of the atomic substances postulate

$$\sum_{\alpha=1}^n \frac{t^{\alpha\iota} s^\alpha}{m^\alpha} = 0, \quad \text{no sum on } \iota \text{ and } 1 \leq \iota \leq n_a, \quad (4.48)$$

where $n_a \in \mathbb{N}$ is the number of atomic substances making up all the components $\dot{\varphi}$, m^α is the molecular weight of the α -th component, and $t^{\alpha\iota}$ is a non-negative integer expressing the number of atoms of the ι -th atomic substance present in the α -th component. This postulate assumes that the atomic substance are indestructible. Moreover, usually $t^{\alpha\iota}$ is not a square matrix and $\text{rank}(t^{\alpha\iota}) = \min(n, n_a)$. Finally, the total number of chemical reactions is obtained from

$$m := n - \text{rank}(t^{\alpha\iota}). \quad (4.49)$$

4.3.3 Chemical reaction in non-ideal solutions

In thermodynamics, the chemical activity accounts for the deviations from ideal behaviour of a mixture of chemical substances [79]. Herein, we briefly explain

how to accommodate such deviations from ideality by introducing the chemical activities, accounting for the effective concentration of each species in the mixture. The adjustments that we make in the free energy potential and reaction terms require the introduction of activity terms, which are a function of the activity coefficients and species concentration. The activity is a function of the activity coefficients and species concentrations through

$$A^\alpha := \zeta^\alpha \varphi^\alpha \quad (4.50)$$

Essentially, non-ideality means that the solution cannot be defined by either Raoult's law or Henry's law [80]. For example, Raoult's law states that the pressure p of an ideal system follows the relation

$$p := \sum_{\alpha=1}^n \varphi^\alpha p_{\text{sat}}^\alpha \quad (4.51)$$

where p_{sat} represents the vapor pressure. Those laws assume that the interaction between molecules is the same regardless the molecule composition. In a binary solution $A-B$, the interactions between A and B molecules are the same as those $A-A$ or $B-B$ molecules. In other words, there is no enthalpy of mixing in a ideal solution as there are no forces acting between the components of different nature. Non-ideal solutions can occur in the following scenarios: 1) The intermolecular forces between molecules of the same nature; namely the same type of molecules, are stronger than the forces acting between solute and solvent molecules, and 2) the intermolecular forces between similar molecules are weaker than those of different molecules [81]. The pressure of non-ideal solutions uses the activity coefficients such that

$$p := \sum_{\alpha=1}^n A^\alpha p_{\text{sat}}^\alpha = \sum_{\alpha=1}^n \zeta^\alpha \varphi^\alpha p_{\text{sat}}^\alpha, \quad (4.52)$$

to account for such deviation from ideality caused by molecular interactions between species [82, 83]. A mixture of carbon disulfide and acetone can be considered as a non-ideal solution. The non-polar dipole moment of the carbon disulfide generates intermolecular forces are weaker than the polar dipole moment of the acetone which leads to a dipole-induced dipole mixture. Powney et al. [84] reports a positive deviation form the Raoult's law for the carbon disulfide-acetone solution.

We define a new free-energy for a non-ideal solution accounting the activity

coefficients as

$$\hat{\psi}(\boldsymbol{\varphi}, \text{grad } \boldsymbol{\varphi}) = \frac{1}{2} N_v k_B \vartheta \left(\sum_{\alpha=1}^n \varphi^\alpha \ln(\varphi^\alpha A^\alpha) \right) + N_v \sum_{\alpha=1}^n \sum_{\beta=1}^n \Omega^{\alpha\beta} \varphi^\alpha \varphi^\beta \quad (4.53)$$

$$+ \frac{1}{2} \sum_{\alpha=1}^n \sum_{\beta=1}^n \Gamma^{\alpha\beta} \text{grad } \varphi^\alpha \cdot \text{grad } \varphi^\beta, \quad (4.54)$$

which renders the following chemical potential

$$\begin{aligned} \mu_\sigma^\alpha &= \frac{1}{2} N_v k_B \vartheta \left(2 \ln \frac{\varphi^\alpha}{\varphi^\sigma} + \ln \frac{\zeta^\alpha}{\zeta^\sigma} \right) + 2 N_v \sum_{\beta=1}^n (\Omega^{\alpha\beta} - \Omega^{\sigma\beta}) \varphi^\beta \\ &\quad - \sum_{\beta=1}^n (\Gamma^{\alpha\beta} - \Gamma^{\sigma\beta}) \text{div grad } \varphi^\beta - (\gamma^\alpha + \gamma^\sigma). \end{aligned} \quad (4.55)$$

We use the definition of activity (4.50) in (4.55). For systems undergoing several non-ideal chemical reactions, the velocities of both the forward and backward reactions read

$$r_+^c := k_+^c \prod_{\alpha=1}^n (A^\alpha)^{v^{\alpha c}} = k_+^c \prod_{\alpha=1}^n (\zeta^\alpha \varphi^\alpha)^{v^{\alpha c}}, \quad (4.56)$$

$$r_-^c := k_-^c \prod_{\alpha=1}^n (A^\alpha)^{\varpi^{\alpha c}} = k_-^c \prod_{\alpha=1}^n (\zeta^\alpha \varphi^\alpha)^{\varpi^{\alpha c}}. \quad (4.57)$$

4.4 Configurational fields

To describe the evolution of interfaces and its thermodynamics, we profit on the configurational forces proposed by Gurtin [85]. These forces are related to the integrity of the material and the movement of defects. As for the thermodynamical interpretation, configurational forces expend power associated to the transfer of matter. Recalling the configurational balance for a part \mathcal{P} by Fried [86], we have

$$\int_S \mathbf{C} \mathbf{n} \, da + \int_{\mathcal{P}} (\mathbf{f} + \mathbf{e}) \, dv = \mathbf{0}, \quad (4.58)$$

which renders, after localizing it,

$$\text{div } \mathbf{C} + \mathbf{f} + \mathbf{e} = \mathbf{0}, \quad (4.59)$$

where \mathbf{C} is the configurational stress tensor, \mathbf{f} is the internal force, and \mathbf{e} the external force.

Our goal is to determine the configurational stress, the internal, and external forces arising from multicomponent systems. We first establish how configurational forces expend power in a migrating control volume \mathcal{P}' , where \mathbf{q} is the

migrating boundary velocity defined on \mathcal{S}' , letting \mathbf{n}' denote the outward unit normal.

For a migrating volume \mathcal{P}' the mass balance (4.3) specializes to

$$\overline{\int_{\mathcal{P}'} \dot{\varphi}^\alpha dv} - \int_{\mathcal{S}'} \varphi^\alpha \mathbf{q} \cdot \mathbf{n}' da = - \int_{\mathcal{S}'} \mathbf{j}^\alpha \cdot \mathbf{n}' da + \int_{\mathcal{P}'} s^\alpha dv. \quad (4.60)$$

We now use the external virtual power (4.18), where γ^α and ξ_s^α are conjugate to $\dot{\varphi}^\alpha$. We set as virtual field the advective term $\dot{\varphi}^\alpha + \text{grad} \varphi^\alpha \cdot \mathbf{q}$ to follow the motion of \mathcal{S}' augmented by the fact that the configurational traction $\mathbf{C}\mathbf{n}'$ is power conjugate to \mathbf{q} on \mathcal{S}' .

Using that

$$\xi_s^\alpha (\dot{\varphi}^\alpha + \text{grad} \varphi^\alpha \cdot \mathbf{q}) = (\boldsymbol{\xi}^\alpha \cdot \mathbf{n}) \dot{\varphi}^\alpha + (\text{grad} \varphi^\alpha \otimes \boldsymbol{\xi}^\alpha) \mathbf{n} \cdot \mathbf{q}, \quad (4.61)$$

we arrive at the total external configurational power

$$\begin{aligned} \mathcal{W}_{\text{ext}}(\mathcal{P}') = \int_{\mathcal{S}'} \left(\mathbf{C} + \sum_{\alpha=1}^n \text{grad} \varphi^\alpha \otimes \boldsymbol{\xi}^\alpha \right) \mathbf{n}' \cdot \mathbf{q} da \\ + \sum_{\alpha=1}^n \left\{ \int_{\mathcal{P}'} \gamma^\alpha \dot{\varphi}^\alpha dv + \int_{\mathcal{S}'} \xi_s^\alpha \dot{\varphi}^\alpha da \right\}. \end{aligned} \quad (4.62)$$

The motion of \mathcal{S}' involves the normal component $\mathbf{q} \cdot \mathbf{n}'$, thus power is indifferent to the tangential component of \mathbf{q} , yielding

$$\mathbf{C} + \sum_{\alpha=1}^n \text{grad} \varphi^\alpha \otimes \boldsymbol{\xi}^\alpha =: \zeta \mathbf{1}, \quad (4.63)$$

where ζ is a scalar field.

Thus, the first integral of (4.62) becomes

$$\int_{\mathcal{S}'} \zeta \mathbf{q} \cdot \mathbf{n}' da. \quad (4.64)$$

Using the arguments that led to the free-energy imbalance (4.15), for isothermal

processes, for a migrating control volume \mathcal{P}' with a velocity \mathbf{q} , we state that

$$\begin{aligned} \overline{\int_{\mathcal{P}'} \dot{\psi} dv} &= \int_{\mathcal{P}'} \dot{\psi} dv + \int_{S'} \left(\psi - \sum_{\alpha=1}^n \mu^\alpha \varphi^\alpha \right) \mathbf{q} \cdot \mathbf{n}' da \leq \\ &\sum_{\alpha=1}^n \left\{ \int_{\mathcal{P}'} \gamma^\alpha \dot{\varphi}^\alpha dv + \int_{S'} \xi_S^\alpha \dot{\varphi}^\alpha da - \int_{S'} \mu^\alpha \mathbf{j}^\alpha \cdot \mathbf{n}' da + \int_{\mathcal{P}'} \mu^\alpha s_{\text{ext}}^\alpha dv \right\} \\ &\quad + \int_{S'} \zeta \mathbf{q} \cdot \mathbf{n}' da, \end{aligned} \quad (4.65)$$

leading to

$$\begin{aligned} \int_{\mathcal{P}'} \dot{\psi} dv &\leq \sum_{\alpha=1}^n \left\{ \int_{\mathcal{P}'} \gamma^\alpha \dot{\varphi}^\alpha dv + \int_{S'} \xi_S^\alpha \dot{\varphi}^\alpha da - \int_{S'} \mu^\alpha \mathbf{j}^\alpha \cdot \mathbf{n}' da + \int_{\mathcal{P}'} \mu^\alpha s_{\text{ext}}^\alpha dv \right\} \\ &\quad + \int_{S'} \left(\zeta - \left(\psi - \sum_{\alpha=1}^n \mu^\alpha \varphi^\alpha \right) \right) \mathbf{q} \cdot \mathbf{n}' da, \end{aligned} \quad (4.66)$$

which implies that

$$\zeta := \psi - \sum_{\alpha=1}^n \mu^\alpha \varphi^\alpha. \quad (4.67)$$

Thus, using the constitutive part (4.67) in the relation (4.63), we arrive at the configurational stress

$$\mathbf{C} := \left(\psi - \sum_{\alpha=1}^n \mu^\alpha \varphi^\alpha \right) \mathbf{1} - \sum_{\alpha=1}^n \text{grad} \varphi^\alpha \otimes \boldsymbol{\xi}^\alpha, \quad (4.68)$$

while using (4.39) and (4.59) with (4.68), we obtain respectively the internal and external configurational forces

$$\mathbf{f} := \sum_{\alpha=1}^n \varphi^\alpha \text{grad} \mu^\alpha \quad \wedge \quad \mathbf{e} := - \sum_{\alpha=1}^n \gamma^\alpha \text{grad} \varphi^\alpha. \quad (4.69)$$

In considering the Larché–Cahn derivatives, the configurational stress (4.68) becomes the relative configurational stress

$$\mathbf{C}_\sigma := \left(\psi - \sum_{\alpha=1}^n \mu_\sigma^\alpha \varphi^\alpha \right) \mathbf{1} - \sum_{\alpha=1}^n \text{grad} \varphi^\alpha \otimes \boldsymbol{\xi}_\sigma^\alpha, \quad (4.70)$$

while

$$\mathbf{f}_\sigma := \sum_{\alpha=1}^n \varphi^\alpha \text{grad} \mu_\sigma^\alpha, \quad (4.71)$$

is the relative internal configurational force. Note that the external configurational force is not constitutively determined, thus, it does not depend upon the choice of the reference species.

Remark 2 (The dependency of \mathbf{C} and \mathbf{f} upon the reference species and the indifference of the configurational balance to the reference species). Given reference species φ^σ , we can establish the following relations that appear in the configurational stress (4.68)

$$\begin{aligned} -\sum_{\alpha=1}^n \mu_\sigma^\alpha \varphi^\alpha &= -\sum_{\alpha=1}^n \mu^\alpha \varphi^\alpha + \mu^\sigma \sum_{\alpha=1}^n \varphi^\alpha \\ &= -\left(\sum_{\alpha=1}^n \mu^\alpha \varphi^\alpha \right) + \mu^\sigma, \end{aligned} \quad (4.72)$$

and

$$\begin{aligned} \sum_{\alpha=1}^n \text{grad } \varphi^\alpha \otimes \boldsymbol{\xi}_\sigma^\alpha &= \sum_{\alpha=1}^n \text{grad } \varphi^\alpha \otimes (\boldsymbol{\xi}^\alpha - \boldsymbol{\xi}^\sigma) \\ &= \sum_{\alpha=1}^n \text{grad } \varphi^\alpha \otimes \boldsymbol{\xi}^\alpha - \left(\sum_{\alpha=1}^n \text{grad } \varphi^\alpha \right) \otimes \boldsymbol{\xi}^\sigma \\ &= \sum_{\alpha=1}^n \text{grad } \varphi^\alpha \otimes \boldsymbol{\xi}^\alpha. \end{aligned} \quad (4.73)$$

while for the internal configurational force (4.69)₁

$$\begin{aligned} \sum_{\alpha=1}^n \varphi^\alpha \text{grad } \mu_\sigma^\alpha &= \sum_{\alpha=1}^n \varphi^\alpha \text{grad } \mu^\alpha - \text{grad } \mu^\sigma \sum_{\alpha=1}^n \varphi^\alpha, \\ &= \left(\sum_{\alpha=1}^n \varphi^\alpha \text{grad } \mu^\alpha \right) - \text{grad } \mu^\sigma. \end{aligned} \quad (4.74)$$

Based on (4.72) and (4.73), we can assert that there is only one term in \mathbf{C} (4.68) that depends on the reference species, that is, the relative configurational stress can be written as

$$\mathbf{C}_\sigma := \mathbf{C} + \mu^\sigma \mathbf{1}, \quad (4.75)$$

while the relative internal configurational force (4.69)₁ is specialized with (4.74) yielding

$$\mathbf{f}_\sigma := \mathbf{f} - \text{grad } \mu^\sigma \mathbf{1}, \quad (4.76)$$

Finally, although the configurational stress and the internal configurational force depend upon the choice φ^σ , this dependency vanishes in the configurational balance (4.59),

$$\begin{aligned} \text{div } \mathbf{C}_\sigma + \mathbf{f}_\sigma &= \text{div}(\mathbf{C} + \mu^\sigma \mathbf{1}) + \mathbf{f} - \text{grad } \mu^\sigma, \\ &= \text{div } \mathbf{C} + \mathbf{f}. \end{aligned} \quad (4.77)$$

□

4.5 Dimensionless Cahn-Hilliard equations

Recalling the final system enclosed by (4.4), (4.39), (4.42), (4.56), (4.57) and (4.47), we arrive at

$$\begin{aligned}
\dot{\varphi}^\alpha &= s^\alpha - \operatorname{div} \mathbf{J}_\sigma^\alpha, \\
\mathbf{J}_\sigma^\alpha &= - \sum_{\beta=1}^n M_0^{\alpha\beta} \varphi^\alpha (\delta^{\alpha\beta} - \varphi^\beta) \operatorname{grad} \mu_\sigma^\beta, \\
\mu_\sigma^\beta &= N_v k_B \vartheta \ln \frac{\varphi^\beta}{\varphi^\sigma} + 2N_v \sum_{\alpha=1}^n (\Omega^{\beta\alpha} - \Omega^{\sigma\alpha}) \varphi^\alpha \\
&\quad - \sum_{\alpha=1}^n (\Gamma^{\beta\alpha} - \Gamma^{\sigma\alpha}) \operatorname{div} \operatorname{grad} \varphi^\alpha - (\gamma^\alpha + \gamma^\sigma), \\
s_{\text{int}}^\alpha &= - \sum_{c=1}^{n_s} \left\{ (v^{c\alpha} - \varpi^{c\alpha}) \left(k_+^c \prod_{a=1}^n (\varphi^a)^{v^{ca}} - k_-^c \prod_{a=1}^n (\varphi^a)^{\varpi^{ca}} \right) \right\},
\end{aligned} \tag{4.78}$$

with

$$\varphi^\alpha(\mathbf{x}, 0) = \varphi_0^\alpha \quad \text{in } \mathcal{P}, \tag{4.79}$$

subject to periodic boundary conditions,

where we inserted the definition of the reaction velocities r_+^c and r_-^c for ideal solutions in s_{int}^α . To make the equations dimensionless, we introduce the reference energy density $\psi_0 := 2N_v k_B \vartheta$ and define the set of diffusion coefficients $D^{\alpha\beta}$,

$$D^{\alpha\beta} = \psi_0 M_0^{\alpha\beta} \varphi^\alpha (\delta^{\alpha\beta} - \varphi^\beta) \quad \text{no sum on } \alpha \text{ and } \beta. \tag{4.80}$$

which follow a linear response relation between the reference energy density and the species mobilities as proposed by Einstein [87, 88]. We additionally define the following dimensionless variables

$$\bar{\mathbf{x}} = L_0^{-1} \mathbf{x}, \quad \bar{t} = T_0^{-1} t, \quad \bar{\vartheta}_c^{\alpha\beta} = \vartheta^{-1} \vartheta_c^{\alpha\beta}. \tag{4.81}$$

Conventionally, the reference time for the Cahn–Hilliard system T_0 is given as a relation between the diffusion coefficient, the interface thickness, and domain length, i.e., $T_0 = D_0 \ell_0^2 L_0^{-4}$ where $L_0 \gg \ell_0$ [89, 90]. We set D_0 and ℓ_0 as the reference diffusion coefficient and interface thickness of a reference species. We propose the following sets of scalar dimensionless numbers for the multicomponent framework, that is,

$$\begin{aligned}
\bar{k}_c^+ &= k_c^+ D_0^{-1} \ell_0^{-2} L_0^4, & \bar{k}_c^- &= k_c^- D_0^{-1} \ell_0^{-2} L_0^4, & \bar{\psi} &= \psi_0^{-1} \psi, \\
\bar{\sigma}^{\alpha\beta} &= \sigma^{\alpha\beta} (\psi_0 L_0)^{-1}, & \bar{D}^{\alpha\beta} &= D^{\alpha\beta} D_0^{-1} \ell_0^{-2} L_0^2, & \bar{\ell}^{\alpha\beta} &= L_0^{-1} \ell^{\alpha\beta}, \\
\bar{\gamma}^\alpha &= \psi_0^{-1} \gamma^\alpha.
\end{aligned} \tag{4.82}$$

By inserting the dimensionless quantities in (4.78), we find the following dimensionless forms

$$\begin{aligned}
\dot{\varphi}^\alpha &= \bar{s}^\alpha - \overline{\text{div}} \bar{\mathcal{J}}^{\alpha\sigma}, \\
\bar{\mathcal{J}}_\sigma^\alpha &= - \sum_{\beta=1}^n D^{\alpha\beta} \overline{\text{grad}} \bar{\mu}_\sigma^\beta, \\
\bar{\mu}_\sigma^\beta &= \frac{1}{2} \ln \frac{\varphi^\beta}{\varphi^\sigma} + 2 \sum_{\alpha=1}^n (\bar{\vartheta}_c^{\beta\alpha} - \bar{\vartheta}_c^{\sigma\alpha}) \varphi^\alpha - \sum_{\alpha=1}^n (\bar{\sigma}^{\beta\alpha} \bar{\ell}^{\beta\alpha} - \bar{\sigma}^{\sigma\alpha} \bar{\ell}^{\sigma\alpha}) \overline{\text{div}} \text{grad} \varphi^\alpha \quad (4.83) \\
&\quad - (\bar{\gamma}^\alpha + \bar{\gamma}^\sigma), \\
\bar{s}_{\text{int}}^\alpha &= - \sum_{c=1}^{n_s} \left\{ (v^{c\alpha} - \varpi^{c\alpha}) (\bar{k}_+^c \prod_{a=1}^n (\varphi^a)^{v^{ca}} - \bar{k}_-^c \prod_{a=1}^n (\varphi^a)^{\varpi^{ca}}) \right\},
\end{aligned}$$

with the initial condition (4.79).

4.6 An energetic variational approach for the multicomponent Cahn–Hilliard equations

4.6.1 Free energies

Let us consider the following multicomponent functions for both the species and species gradient concentrations, respectively

$$\tilde{\varphi} = \{\varphi^1, \dots, \varphi^n\} \quad (4.84a)$$

$$\text{grad} \tilde{\varphi} = \{\text{grad} \varphi^1, \dots, \text{grad} \varphi^n\} \quad (4.84b)$$

$$\varphi = \{\varphi^1, \dots, \varphi^{n-1}, 1 - \sum_{\alpha=1}^{n-1} \varphi^\alpha\} \quad (4.84c)$$

$$\text{grad} \varphi = \{\text{grad} \varphi^1, \dots, \text{grad} \varphi^{n-1}, - \sum_{\alpha=1}^{n-1} \text{grad} \varphi^\alpha\}. \quad (4.84d)$$

The aforementioned sets φ and $\text{grad} \varphi$ take into account the mass constraint (4.5) by imposing $\varphi^n = 1 - \sum_{\alpha=1}^{n-1} \varphi^\alpha$ where we use the n -th species as the reference component. Thereby, we do not consider φ^n . The tilde functions embrace the whole set of species. In a physical domain \mathcal{P} , the Ginzburg–Landau free energy is given by

$$\tilde{\Psi}(\tilde{\varphi}, \text{grad} \tilde{\varphi}) = \int_{\mathcal{P}} \left[\tilde{\psi}(\tilde{\varphi}, \text{grad} \tilde{\varphi}) \right] dv = \int_{\mathcal{P}} \left[\tilde{\psi}^\varphi(\tilde{\varphi}) + \tilde{\psi}^s(\text{grad} \tilde{\varphi}) \right] dv. \quad (4.85)$$

This energy is a function of both the n -well free energy $\tilde{\psi}^\varphi$

$$\tilde{\psi}^\varphi(\tilde{\varphi}) = N_v k_B \vartheta \left(\sum_{\alpha=1}^n \varphi^\alpha \ln \varphi^\alpha \right) + N_v \sum_{\alpha=1}^n \sum_{\beta=1}^n \Omega^{\alpha\beta} \varphi^\alpha \varphi^\beta \quad (4.86a)$$

$$\begin{aligned} \psi^\varphi(\varphi) = N_v k_B \vartheta \left\{ \sum_{\alpha=1}^{n-1} \varphi^\alpha \ln \varphi^\alpha + \left(1 - \sum_{\alpha=1}^{n-1} \varphi^\alpha\right) \ln \left(1 - \sum_{\beta=1}^{n-1} \varphi^\beta\right) \right\} \\ + N_v \left\{ \sum_{\alpha=1}^{n-1} \sum_{\beta=1}^{n-1} (\Omega^{\alpha\beta} + \Omega^{nn} - \Omega^{\alpha n} - \Omega^{n\beta}) \varphi^\alpha \varphi^\beta \right. \end{aligned} \quad (4.86b)$$

$$\left. + \sum_{\alpha=1}^{n-1} (\Omega^{\alpha n} + \Omega^{n\alpha} - 2\Omega^{nn}) \varphi^\alpha \right\}. \quad (4.86c)$$

and the interfacial free energy

$$\tilde{\psi}^s(\text{grad } \tilde{\varphi}) = \frac{1}{2} \sum_{\alpha=1}^n \sum_{\beta=1}^n \Gamma_{\alpha\beta} \text{grad } \varphi^\alpha \cdot \text{grad } \varphi^\beta \quad (4.87a)$$

$$\psi^s(\text{grad } \varphi) = \frac{1}{2} \sum_{\alpha=1}^{n-1} \sum_{\beta=1}^{n-1} (\Gamma_{\alpha\beta} + \Gamma_{nn} - \Gamma_{\alpha n} - \Gamma_{n\beta}) \text{grad } \varphi^\alpha \cdot \text{grad } \varphi^\beta. \quad (4.87b)$$

Using a negative definite gradient energy with null diagonal, for example the binary case $\Gamma^{\alpha\beta} = -0.5\Gamma$, we can recover the former Cahn-Hilliard equation [45].

4.6.2 Chemical potentials

As mentioned above, the chemical potential is the variational derivative of the free energy with respect to the species concentration. Such energy quantifies the exchange process resulting from the bulk and interfacial contributions. Hence, the α -th chemical potential taking as the reference species the n -th component is

$$\tilde{\mu}^\alpha = \frac{\delta \tilde{\Psi}}{\delta \varphi^\alpha}, \quad (4.88)$$

which entails

$$\frac{\delta \Psi}{\delta \varphi^\alpha} = \frac{\delta \tilde{\Psi}}{\delta \varphi^\alpha} - \frac{\delta \tilde{\Psi}}{\delta \varphi^n} = \tilde{\mu}^\alpha - \tilde{\mu}^n, \quad (4.89)$$

for $\alpha = 1, \dots, n-1$. The n -well (bulk) term is

$$\begin{aligned} \tilde{\mu}_\varphi^\alpha &= N_v k \vartheta (\ln \varphi^\alpha + 1) + N_v \sum_{\beta=1}^n (\Omega^{\alpha\beta} + \Omega^{\beta\alpha}) \varphi^\beta \\ &= N_v k \vartheta (\ln \varphi^\alpha + 1) + 2N_v \sum_{\beta=1}^n \Omega^{\alpha\beta} \varphi^\beta, \end{aligned} \quad (4.90a)$$

and the interfacial one is given by

$$\begin{aligned}\tilde{\mu}_s^\alpha &= -\frac{1}{2} \sum_{\beta=1}^n (\Gamma^{\alpha\beta} + \Gamma^{\beta\alpha}) \Delta\varphi^\beta \\ &= -\sum_{\beta=1}^n \Gamma^{\alpha\beta} \Delta\varphi^\beta.\end{aligned}\tag{4.91a}$$

We apply (4.89) which leads to the following set of chemical potentials

$$\mu_\varphi^\alpha = N_v k \vartheta \left(\ln \frac{\varphi^\alpha}{\varphi^n} \right) + 2N_v \sum_{\beta=1}^n (\Omega^{\alpha\beta} - \Omega^{n\beta}) \varphi^\beta,\tag{4.92}$$

$$\mu_s^\alpha = -\sum_{b=1}^n (\Gamma^{\alpha b} - \Gamma^{n b}) \Delta\varphi^b\tag{4.93}$$

for $\alpha = 1, \dots, n$. Finally, $\mu^\alpha = \mu_\varphi^\alpha + \mu_s^\alpha$ [45].

4.6.3 Generalized Fick's law

The mass fluxes relating the off-diagonal terms in the Onsager reciprocal relations are given by

$$\mathbf{j}^\alpha = -\sum_{\beta=1}^n \mathbf{M}^{\alpha\beta} \text{grad } \tilde{\mu}^\beta, \quad \alpha = 1, \dots, n,\tag{4.94}$$

where $\mathbf{M}^{\alpha\beta}$ are the Onsager mobility coefficients. To conserve mass, the mass fluxes must satisfy the following constraint

$$\sum_{\alpha=1}^n \mathbf{j}^\alpha = 0,\tag{4.95}$$

which implies the relation

$$\sum_{\beta=1}^n \mathbf{M}^{\alpha\beta} = 0, \quad \forall \alpha.\tag{4.96}$$

Thereby, the mass flux for each component is

$$\begin{aligned}\mathbf{j}^\alpha &= -\sum_{\beta=1}^n \mathbf{M}^{\alpha\beta} \text{grad } \tilde{\mu}^\beta \\ &= -\left(\sum_{\beta=1}^{n-1} \mathbf{M}^{\alpha\beta} \text{grad } \tilde{\mu}^\beta + \mathbf{M}^{\alpha n} \text{grad } \tilde{\mu}^n \right) \\ &= -\left(\sum_{\beta=1}^{n-1} \mathbf{M}^{\alpha\beta} \text{grad } \tilde{\mu}^\beta - \left(\sum_{\beta=1}^{n-1} \mathbf{M}^{\alpha\beta} \right) \text{grad } \tilde{\mu}^n \right) \\ &= -\sum_{\beta=1}^{n-1} \mathbf{M}^{\alpha\beta} \text{grad } (\tilde{\mu}^\beta - \tilde{\mu}^n)\end{aligned}\tag{4.97}$$

As expressed above, the mobility tensor depends on the species concentrations [45].

Chapter 5

Derivation of a coupled chemo-mechanical system

We develop a thermodynamically-consistent framework to characterise the evolution of chemically active elastic solids. We model the system as a solid-species solution where the species mass transport and chemical reaction drive the stress generation process. We treat the solid as a continuum body and following the Larché and Cahn network model, we define displacement and strain fields. Thereby, the strain quantifies the deformation of the network with respect to a reference network configuration set as an undeformed state. We carry out balances of solid and species mass conservation, balances of conservation of linear and angular momenta as well as balances of microforces. Using conservation balances and first and second law of thermodynamics, we build a Lagrangian description for the Helmholtz free energy of system. By means of the Coleman-Noll procedure, we find the relations between the chemical potentials, microforces, stress and the Helmholtz free energy. A mass constraint imposed by the solid crystalline structure leads to definition of the relative chemical potentials, relative mass fluxes, and relative microforces. These physical quantities result from the definition of the Larché-Cahn derivative in saturated systems. Additionally, a general law of mass action models the source/sink of mass in the balance of species mass conservation. This relation allows to model complex chemical reactions. Finally, we provide several simulation results to showcase and verify the chemo-mechanical interactions of a solid-species solution that undergoes spinodal decomposition, chemical reactions and deformation.

5.1 Introduction

When considering a deformable medium, chemical reactions may affect the solid strength and its mechanical properties. Analogously, high mechanical strength may suppress either the volumetric shrinkage or swelling associated with the local volume changes caused by the chemical processes. Therefore, the chemical processes, associated with mass transport and chemical reactions, induce volume changes that lead to stresses around the reaction site.

Finding innovative ways of approaching the modelling of solids is an important open research topic in science and engineering. For instance, areas such as material science and geoscience are constantly in the search of new models which allow them to improve the properties of materials or to understand the formation of mineral assemblages. Both relate solids that undergo chemical processes. Thus, the description of solidity and its properties is crucial to understand the nature of the physical and chemical responses of solids. In this effort, Gibbs carried out a comprehensive study that set the groundwork of the thermodynamical properties of solids [91]. However, Gibbs' solid model does not quantify internal adjustment caused by compositional changes since the concept of solid state diffusion did not exist by Gibbs' time. Herein, we seek to model multicomponent elastic solids that allow for changes in composition while remaining in the solid state, and in particular, the impact of compositional changes towards stress generation [33–36]. Larché and Cahn introduced the equilibrium conditions of deformable bodies which change composition as a result of chemical processes [10, 12, 38]. For instance, dissolution and precipitation at solid-fluid interfaces change the chemical composition of the solid which in turn induce stresses associated with volume changes. Larché-Cahn's approach models the solid as a network which allows to define the stress-strain relations. In nature, a solid network can be, for example, the unit cell of the crystalline structure of polymers, which arranges the atoms in a systematic and repeating pattern. Thus, we follow the network model of Larché and Cahn to adequately describe the multicomponent solid.

To date, several authors have published the intrinsic behaviour of diffusion-mechanics based on theoretical modelling as well as experimental procedures [3, 92–100]. For instance, Dal et al. [34] study the performance of lithium ion battery electrodes by using a electro-chemo-mechanical coupling at finite strain. In their model, the Butler-Volmer kinetic equation defines the electrochemistry

of the surface reaction. At the solid boundary, the reaction triggers the diffusion of ions in the battery which in turn induces volumetric deformation. Spinodal decomposition during the phase transformation of martensite relates large volume changes. As a consequence, deformation can occur leading to a change in solid crystalline structure. Moreover, the precipitation of new phases, which may possess another crystalline structure, induces additional stresses in the solid. Motivated by this, Rudraraju et al. [101] propose a multicomponent framework for crystalline solids under diffusional phase transformation. The free energy of the system is a function of both a mechanical potential, which relates the symmetry-breaking structural changes of the crystal unit cell, and the chemical free energy where each spinodal represents a phase.

The outline of this chapter is as follows. Section §5.2 studies the kinematics of the motion, the fundamental balances of a continuum body and the thermodynamic laws. Therein, we present a coupled system of partial differential equations to model mass transport and deformation processes. In section §5.3, we present the Coleman–Noll procedure together with the necessary constitutive relations that define a neo-Hookean elastic solid undergoing spinodal decomposition while its constituent species react. In this section, we also make use of the Larché–Cahn derivative as outlined in section §4.2.3, followed by Section §5.4 which covers the dimensionless forms of the coupled system of chemo-mechanical equations for the multicomponent framework in conjunction with the dimensionless numbers of the coupling.

5.2 Fundamental balances and thermodynamics laws

5.2.1 Kinematics of the motion

We introduce a system of partial differential equations to capture the evolution of a multicomponent elastic solid undergoing spinodal decomposition together with a reversible chemical reaction. In our framework, deformation induced across the solid boundaries and compositional changes drive the stress generation process. Henceforth, we will call this mechanism as stress-assisted volume changes. We treat the solid as a continuum body that occupies an open subset \mathbf{B} of the

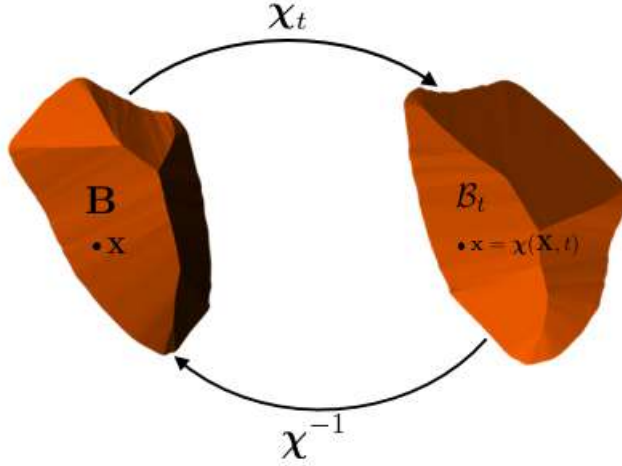


Figure 5.1 The deformation field χ defines the kinematics of the motion of the particles in the body from a configuration \mathbf{B} onto another configuration \mathcal{B}_t .

Euclidean space \mathcal{E} . A time-dependent deformation field $\chi : \mathbf{B} \times T \rightarrow \mathcal{B}_t \subset \mathcal{E}$ describes the motion from a configuration \mathbf{B} onto another configuration \mathcal{B}_t . We refer to \mathbf{B} as the reference configuration and to \mathbf{X} as the particles in \mathbf{B} . We set the reference configuration such that \mathbf{B} represents an undeformed state of the solid. The deformation field characterizes the kinematics of the motion of the particles in the body, and after deformation, it assigns to each material particle \mathbf{X} at a given $t \in T$ a spatial particle \mathbf{x} in the current configuration \mathcal{B}_t . The deformation field is then expressed as

$$\mathbf{x} \stackrel{\text{def}}{=} \chi(\mathbf{X}, t) = \chi_t(\mathbf{X}), \quad (5.1)$$

which implies

$$\mathcal{B}_t = \chi_t(\mathbf{B}). \quad (5.2)$$

The deformation field is invertible; namely, there exists an inverse deformation field $\chi^{-1} : \mathcal{B}_t \times T \rightarrow \mathbf{B} \subset \mathcal{E}$ such that

$$\mathbf{x} = \chi_t(\chi^{-1}(\mathbf{x}, t)), \quad (5.3)$$

and which renders

$$\mathbf{X} \stackrel{\text{def}}{=} \chi^{-1}(\mathbf{x}, t). \quad (5.4)$$

Figure 5.1 portrays the reference and current configuration in conjunction with the motion of the particles. Herein, we adopt the notation suggested by Gurtin et al. [33]. In particular, we use the differential operators that account for

the material and spatial description of scalar, vector, and tensor fields. Then, ∇ and Div represent the gradient and divergence with respect to material particles \mathbf{X} in the reference configuration \mathbf{B} , respectively. Likewise, grad and div correspond to the gradient and divergence with respect to spatial particles $\mathbf{x} = \boldsymbol{\chi}_t(\mathbf{X})$ in the current configuration \mathcal{B}_t , respectively. Besides, we denote second order tensors and vectors by bold symbols.

In deforming bodies undergoing mass transport and chemical reactions, the particles move relative to each other as a result of external forces and compositional changes. This movement can be arrested by measuring the relative displacement of the particles. We use a Lagrangian description of the displacement field \mathbf{u} which defines the kinematics of the motion, that is,

$$\mathbf{u} = \mathbf{x}(\mathbf{X}, t) - \mathbf{X} \quad (5.5)$$

and the deformation gradient

$$\mathbf{F} = \nabla \boldsymbol{\chi}_t = \nabla \mathbf{u} + \mathbf{I} \quad (5.6)$$

where \mathbf{I} defines the second order identity tensor. To ensure an admissible deformation, i.e., a continuum body cannot penetrate itself, the Jacobian of the deformation gradient must fulfill the following constraint

$$J \stackrel{\text{def}}{=} \det \mathbf{F} > 0. \quad (5.7)$$

The velocity of a material particle \mathbf{X} as a function of the motion is given by

$$\mathbf{V} \stackrel{\text{def}}{=} \frac{\partial \boldsymbol{\chi}(\mathbf{X}, t)}{\partial t} \quad (5.8)$$

and its counterpart in the current configuration is

$$\mathbf{v} \stackrel{\text{def}}{=} \left. \frac{\partial \boldsymbol{\chi}(\mathbf{X}, t)}{\partial t} \right|_{\mathbf{x}=\boldsymbol{\chi}^{-1}(\mathbf{x}, t)}. \quad (5.9)$$

Equation (5.9) describes the velocity at time t of a material particle located at $\mathbf{x} = \boldsymbol{\chi}_t(\mathbf{X})$.

Given the definition of the deformation gradient and the spatial velocity, the right Cauchy-Green stress, the Green-Lagrange strain, the rate of strain tensors and the spatial velocity gradient are given by

$$\mathbf{C} = \mathbf{F}^\top \mathbf{F}, \quad (5.10)$$

$$\mathbf{E} = \frac{1}{2} \left(\mathbf{F}^\top \mathbf{F} - \mathbf{I} \right) = \frac{1}{2} (\mathbf{C} - \mathbf{I}), \quad (5.11)$$

$$\mathbf{D} = \text{sym}(\text{grad } \mathbf{v}) = \frac{1}{2}(\text{grad } \mathbf{v} + \text{grad } \mathbf{v}^\top), \quad (5.12)$$

$$\mathbf{L} = (\text{grad } \mathbf{v}) = \dot{\mathbf{F}}\mathbf{F}^{-1}. \quad (5.13)$$

The relation between the reference and current configuration is obtained by applying the change of variable theorem. In particular, these equations account for the deformation of an infinitesimal line, area, and volume element, that is,

$$d\mathbf{x} = \mathbf{F} d\mathbf{X}, \quad (5.14)$$

$$da = J\mathbf{F}^{-\top} da_{\text{R}}, \quad (5.15)$$

$$dv = J dv_{\text{R}}. \quad (5.16)$$

5.2.2 Fundamental balances

We derive a set of balance equations in the form of partial differential equations which define how the mass, linear and angular momenta, internal energy and entropy vary in time as the solid-species system endures mechanical and chemical processes. As suggested in [33–36], three primary fields govern the coupled chemo-mechanical responses of the solid: the deformation $\boldsymbol{\chi}(\mathbf{X}, t)$, the species concentration $\varphi_{\text{R}}^\alpha(\mathbf{X}, t)$ per unit of reference volume, and the chemical potential $\mu_{\text{R}}^\alpha(\mathbf{X}, t)$ per unit of reference volume where α denotes the α -th species that composes the solid.

Let $\mathbf{P} \subset \mathbf{B}$ be an arbitrary control volume in conjunction with its boundary $S = \partial\mathbf{P}$. Analogously, consider \mathcal{P}_t as a bounded control volume of \mathcal{B}_t such that $\mathcal{P}_t = \boldsymbol{\chi}(\mathbf{P})$ with boundary $\mathcal{S} = \partial\mathcal{P}_t$. According to Cauchy's theorem, the traction \mathbf{t} on a surface $da \subset \mathcal{S}$ and whose normal \mathbf{n} points outwards is

$$\mathbf{t} \stackrel{\text{def}}{=} \mathbf{T}(\mathbf{x}, t)\mathbf{n}. \quad (5.17)$$

This traction characterizes the force exerted by the rest of the body $\mathcal{B}_t \setminus \mathcal{P}_t$ on \mathcal{P}_t through $da \subset \mathcal{S}$ [34, 35]. The traction \mathbf{t} depends linearly pointwise on the normal \mathbf{n} through Cauchy's stress tensor \mathbf{T} [102]. Applying the Equation (5.15) to the identity $\mathbf{t}_{\text{R}} da_{\text{R}} = \mathbf{t} da$, we find the force acting on the surface element da as a function of the surface element da_{R} [33, 34]. This identity leads to the nominal stress tensor \mathbf{T}_{R} ,

$$\mathbf{T}_{\text{R}} da_{\text{R}} = \mathbf{T} da \quad \text{with} \quad \mathbf{T}_{\text{R}} = J\mathbf{T}\mathbf{F}^{-\top}. \quad (5.18)$$

As mentioned above, the chemo-mechanical interactions take place through an elastically deforming solid composed by a network and constituent species. Consequently, we formulate balances of mass conservation for both the solid and the constituent species. Thus, we define $\varphi_{\mathbf{R}}^\alpha$ as the local concentration of the α -th species per unit of undeformed configuration together with a spatial species outflux \mathbf{j}^α . In agreement with the balance of mass conservation, the rate of mass change of the α -th species in the control volume \mathbf{P} has to be equal to the contribution from the mass supply, typically caused by chemical reactions between the species, and the net mass flux through the boundary \mathcal{S} , that is,

$$\overline{\int_{\mathbf{P}} \dot{\varphi}_{\mathbf{R}}^\alpha dv_{\mathbf{R}}} = \int_{\mathbf{P}} s^\alpha dv_{\mathbf{R}} - \int_{\mathcal{S}} \mathbf{j}^\alpha \cdot \mathbf{n} dv \quad (5.19)$$

where s^α is the mass supply expressed in the reference configuration. As outlined in §4.2.1 (see (4.2)), the mass supply is composed by two terms, an external contribution due to external agents and an internal contributions due to chemical reactions. Thus,

$$s^\alpha := s_{\text{int}}^\alpha + s_{\text{ext}}^\alpha. \quad (5.20)$$

Using the divergence theorem, we transform the surface integral of the species flux into a volume integral of the divergence of the species flux as follows

$$\overline{\int_{\mathbf{P}} \dot{\varphi}_{\mathbf{R}}^\alpha dv_{\mathbf{R}}} = \int_{\mathbf{P}} s^\alpha dv_{\mathbf{R}} - \int_{\mathcal{S}} \text{div } \mathbf{j}^\alpha dv. \quad (5.21)$$

The Lagrangian description of Equation (5.21) is

$$\overline{\int_{\mathbf{P}} \dot{\varphi}_{\mathbf{R}}^\alpha dv_{\mathbf{R}}} = \int_{\mathbf{P}} s^\alpha dv_{\mathbf{R}} - \int_{\mathbf{P}} \text{Div } \mathbf{J}_R^\alpha dv_{\mathbf{R}} \quad (5.22)$$

where we use the Piola transform. Thus, the material species flux is then $\mathbf{J}_R^\alpha = \mathbf{F}^{-1}(\mathbf{J}\mathbf{j}^\alpha)$. Finally, the localized version of Equation (5.22) is given by

$$\dot{\varphi}_{\mathbf{R}}^\alpha = s^\alpha - \text{Div } \mathbf{J}_R^\alpha. \quad (5.23)$$

The concentration of each species is linearly dependent on the other, that is,

$$\sum_{\alpha=1}^n \varphi_{\mathbf{R}}^\alpha = 1 \quad (5.24)$$

which renders

$$\sum_{\alpha=1}^n \dot{\varphi}_{\mathbf{R}}^\alpha = 0 \quad \text{and} \quad \sum_{\alpha=1}^n \nabla \varphi_{\mathbf{R}}^\alpha = 0 \quad (5.25)$$

where n stands for the total number of species. In general, when the solid is solely composed of the diffusing species the mass constraint given by Equation

(5.24) must always hold. Herein, we restrict our attention to the case where mass transport by vacancies is not feasible.

Henceforth, a superimposed dot ($\dot{\cdot}$) stands for the material time derivative, for instance, $\dot{\varphi}_R^\alpha$ is the material time derivative of the concentration species. With regard to the conservation of solid mass, we define ρ and ρ_0 as the solid density in the current and reference configuration, respectively. Then, the balance of solid mass conservation reads

$$\int_{\mathcal{P}_t} \rho \, dv = \int_{\mathbf{P}} \rho_0 \, dv_R \quad (5.26)$$

In Equation (5.26), we convert the volume integral in the current configuration into its counterpart in the reference configuration by employing the relation (5.16). Finally, we use the localization theorem that leads to the local conservation of solid mass

$$\rho_0 = J\rho. \quad (5.27)$$

Neglecting all inertial effects; namely, we assume the spatial velocity \mathbf{v} is invariant through the time, the balance of conservation of linear momenta reads

$$\int_S \mathbf{t} \, da + \int_{\mathbf{P}} \mathbf{b} \, dv_R = \mathbf{0}. \quad (5.28)$$

The balance of linear momenta relates all forces that influence any change in the motion of the body. Such balance involves the traction \mathbf{t} acting on a surface element da as well as a body force \mathbf{b} . Conventionally, the body force \mathbf{b} accounts for forces resulting from gravitational effects. Through the diverge theorem and the definition (5.17), we express the surface integral in Equation (5.28) as a volume integral

$$\int_{\mathcal{P}_t} \operatorname{div} \mathbf{T} \, dv + \int_{\mathbf{P}} \mathbf{b} \, dv_R = \mathbf{0} \quad (5.29)$$

and after some straightforward manipulations in Equation (5.29), the localized Lagrangian form of the balance of linear momenta is

$$\operatorname{Div} \mathbf{T}_R + \mathbf{b} = \mathbf{0}. \quad (5.30)$$

The balance of conservation of angular momenta can be expressed as

$$\int_{\mathcal{P}_t} \mathbf{x} \times \mathbf{t} \, dv + \int_{\mathbf{P}} \mathbf{x} \times \mathbf{b} \, dv_R = \mathbf{0} \quad (5.31)$$

where after using the definition of the balance of linear momenta, the divergence theorem and the localization theorem, we end up with

$$\mathbf{T}^\top = \mathbf{T}. \quad (5.32)$$

The previous relation is a direct consequence of the symmetric nature of Cauchy's tensor [11, 103]. Finally, the localized Lagrangian form of the balance of angular momenta is

$$\text{skw}\mathbf{T}_R\mathbf{F}^T = \mathbf{0}. \quad (5.33)$$

Following the line of thought introduced by Gurtin and Fried [50, 73–75], we separate balances of conservation laws from constitutive equations. As a consequence, we include a balance of microforces, that is

$$\int_{\mathbf{P}} (\pi^\alpha + \gamma^\alpha) dv_R = - \int_{\mathcal{S}} \boldsymbol{\xi}^\alpha \cdot \mathbf{n} da \quad (5.34)$$

where the vector $\boldsymbol{\xi}^\alpha$ and the scalar π^α (γ^α) correspond to the α -th microstress and α -th the internal (external) microforce, respectively. In general, the microstresses and microforces are quantities associated with microscopic configurations of atoms. We express the balance of microforces in a Lagrangian form

$$\int_{\mathbf{P}} (\pi^\alpha + \gamma^\alpha) dv_R = - \int_{\mathbf{P}} \text{Div} \boldsymbol{\Xi}^\alpha dv_R, \quad (5.35)$$

and after applying the localization theorem, the balance for microforces reads

$$\pi^\alpha + \gamma^\alpha = -\text{Div} \boldsymbol{\Xi}^\alpha \quad (5.36)$$

where $\boldsymbol{\Xi}^\alpha = \mathbf{F}^{-1}(J\boldsymbol{\xi}^\alpha)$.

5.2.3 Thermodynamics laws and free energy inequality

We separate conservation statements from constitutive equations as suggested by Gurtin & Fried [50, 73–75].

To describe the thermodynamics of this system, we introduce a power expenditure $\mathcal{W}_{\text{ext}} = \mathcal{W}_{\text{ext}}(\mathbf{P}) + \mathcal{W}_{\text{ext}}(\mathcal{P})$ externally to \mathbf{P} and \mathcal{P} done by the external microforce and force on \mathbf{P} , and the microtraction and traction on \mathcal{S}

$$\mathcal{W}_{\text{ext}}(\mathbf{P}) := \sum_{\alpha=1}^n \left\{ \int_{\mathbf{P}} \gamma^\alpha \dot{\varphi}_R^\alpha dv_R \right\} + \int_{\mathbf{P}} \mathbf{b} \cdot \mathbf{v} dv_R, \quad (5.37a)$$

$$\mathcal{W}_{\text{ext}}(\mathcal{P}) := \sum_{\alpha=1}^n \left\{ \int_{\mathcal{S}} \xi_S^\alpha \dot{\varphi}_R^\alpha da \right\} + \int_{\mathcal{S}} \mathbf{t} \cdot \mathbf{v} da. \quad (5.37b)$$

Neglecting all inertial effects and body forces, the first law of thermodynamics characterizes the energy balance between the rate of internal energy $\dot{\epsilon}$ and the rate

at which chemo-mechanical power, caused by external forces, species transport and chemical reactions, is expended. The first law is then,

$$\begin{aligned} \overline{\int_{\mathbf{P}} \varepsilon dv_{\mathbf{R}}} &= \mathcal{W}_{\text{ext}} - \int_{\mathcal{S}} \mathbf{q} \cdot \mathbf{n} da + \int_{\mathbf{P}} r dv_{\mathbf{R}} \\ &\quad - \sum_{\alpha=1}^n \left\{ \int_{\mathcal{S}} \mu_{\mathbf{R}}^{\alpha} \mathbf{J}^{\alpha} \cdot \mathbf{n} da - \int_{\mathbf{P}} \mu_{\mathbf{R}}^{\alpha} s_{\text{ext}}^{\alpha} dv_{\mathbf{R}} \right\}. \end{aligned} \quad (5.38)$$

As mentioned in chapter §4.2.2, there is no contribution of s_{int}^{α} to the energy balance (5.38). The entropy imbalance, in the form of the Clausius-Duhem inequality, states that the rate of growth of the entropy η is at least as large as the entropy flux \mathbf{q}/ϑ plus the contribution from the entropy supply q/ϑ , that is,

$$\overline{\int_{\mathbf{P}} \eta dv_{\mathbf{R}}} \geq - \int_{\mathcal{S}} \frac{\mathbf{q} \cdot \mathbf{n}}{\vartheta} da + \int_{\mathbf{P}} \frac{r}{\vartheta} dv_{\mathbf{R}} \quad (5.39)$$

where \mathbf{q} , r and ϑ stand for the spatial heat flux, heat supply and temperature, respectively.

Remark 3. *Let us rewrite (5.37) using index notation. Einstein summation convention applies, i.e., summation over a pair of repeated indexes*

$$\mathcal{W}_{\text{ext}}(\mathbf{P}) = \sum_{\alpha=1}^n \left\{ \int_{\mathbf{P}} \gamma^{\alpha} \dot{\varphi}_{\mathbf{R}}^{\alpha} dv_{\mathbf{R}} \right\} + \int_{\mathbf{P}} \mathbf{b}_i \mathbf{v}_i dv_{\mathbf{R}}, \quad (5.40a)$$

$$\mathcal{W}_{\text{ext}}(\mathcal{P}) = \sum_{\alpha=1}^n \left\{ \int_{\mathcal{S}} \xi_{\mathcal{S}}^{\alpha} \dot{\varphi}_{\mathbf{R}}^{\alpha} da \right\} + \int_{\mathcal{S}} \mathbf{t}_i \mathbf{v}_i da. \quad (5.40b)$$

Using the relation (5.17) in (5.40b), we obtain

$$\mathcal{W}_{\text{ext}}(\mathcal{P}) = \sum_{\alpha=1}^n \left\{ \int_{\mathcal{S}} \xi_{\mathcal{S}}^{\alpha} \dot{\varphi}_{\mathbf{R}}^{\alpha} da \right\} + \int_{\mathcal{S}} \mathbf{T}_{ij} \mathbf{n}_j \mathbf{v}_i da. \quad (5.41)$$

Then, we apply integration by parts and the divergence theory

$$\mathcal{W}_{\text{ext}}(\mathcal{P}) = \sum_{\alpha=1}^n \left\{ \int_{\mathcal{P}} (\xi_i^{\alpha} \dot{\varphi}_{\mathbf{R}}^{\alpha})_{,i} dv \right\} + \int_{\mathcal{P}} (\mathbf{T}_{ij} \mathbf{v}_i)_{,j} dv. \quad (5.42)$$

The Lagrangian form (5.42) is

$$\mathcal{W}_{\text{ext}}(\mathbf{P}) = \sum_{\alpha=1}^n \left\{ \int_{\mathbf{P}} (\Xi_J^{\alpha} \dot{\varphi}_{\mathbf{R}}^{\alpha})_{,J} dv_{\mathbf{R}} \right\} + \int_{\mathbf{P}} (\mathbf{T}_{RiJ} \mathbf{v}_i)_{,J} dv_{\mathbf{R}}. \quad (5.43)$$

In (5.43), we use the Piola transform. Now, \mathcal{W}_{ext} is given by

$$\begin{aligned} \mathcal{W}_{\text{ext}} = & \sum_{\alpha=1}^n \left\{ \int_{\mathbf{P}} (\Xi_{J,J}^\alpha + \gamma^\alpha) \dot{\varphi}_R^\alpha + \dot{\varphi}_{R,J}^\alpha \Xi_J^\alpha dv_R \right\} \\ & + \int_{\mathbf{P}} (\mathbf{T}_{RiJ,J} + \mathbf{b}_i) \mathbf{v}_i + \mathbf{T}_{RiI} \dot{\mathbf{F}}_{iI} dv_R. \end{aligned} \quad (5.44)$$

where we use the definition (5.13) for the spatial velocity gradient.

The localized Lagrangian version of (5.38) and (5.39) read

$$\dot{\varepsilon} = \mathcal{W}_{\text{ext}} - \text{Div} \mathbf{q}_R + r - \sum_{\alpha=1}^n \{ \text{Div} \mu_R^\alpha \mathbf{J}_R^\alpha - \mu_R^\alpha s_{\text{ext}}^\alpha \}, \quad (5.45)$$

and

$$\dot{\eta} \geq -\text{Div} \vartheta^{-1} \mathbf{q}_R + \vartheta^{-1} r \quad (5.46)$$

where $\mathbf{q}_R = \mathbf{F}^{-1}(J\mathbf{q})$ is the material heat flux. Moreover, \mathcal{W}_{ext} is

$$\mathcal{W}_{\text{ext}} = \sum_{\alpha=1}^n \{ (\text{Div} \Xi^\alpha + \gamma^\alpha) \dot{\varphi}_R^\alpha + \Xi^\alpha \cdot \nabla \dot{\varphi}_R^\alpha \} + (\text{Div} \mathbf{T}_R + \mathbf{b}) \cdot \mathbf{v} + \mathbf{T}_R : \dot{\mathbf{F}}. \quad (5.47)$$

Rewriting (5.45) and (5.46), and multiplying (5.46) by ϑ , we obtain

$$\dot{\varepsilon} = \mathcal{W}_{\text{ext}} - \text{Div} \mathbf{q}_R + r - \sum_{\alpha=1}^n \{ \nabla \mu_R^\alpha \cdot \mathbf{J}_R^\alpha + \mu_R^\alpha \text{Div} \mathbf{J}_R^\alpha - \mu_R^\alpha s_{\text{ext}}^\alpha \}, \quad (5.48)$$

and

$$\vartheta \dot{\eta} \geq \vartheta^{-1} \nabla \vartheta \cdot \mathbf{q}_R - \text{Div} \mathbf{q}_R + r. \quad (5.49)$$

The Helmholtz free energy results from applying the Legendre transform to the internal energy while replacing the entropy of the system by the temperature as an independent variable., i.e., $\dot{\psi} = \dot{\varepsilon} - \dot{\vartheta} \eta - \vartheta \dot{\eta}$. Consequently, we obtain

$$\dot{\psi} \leq \mathcal{W}_{\text{ext}} - \sum_{\alpha=1}^n \{ \nabla \mu_R^\alpha \cdot \mathbf{J}_R^\alpha + \mu_R^\alpha \text{Div} \mathbf{J}_R^\alpha - \mu_R^\alpha s_{\text{ext}}^\alpha \} - \vartheta^{-1} \nabla \vartheta \cdot \mathbf{q}_R - \dot{\vartheta} \eta \quad (5.50)$$

Introducing the balances of both mass conservation and microforces into (5.50), the free energy imbalance under isothermal conditions is

$$\dot{\psi} \leq \mathbf{T}_R : \dot{\mathbf{F}} + \sum_{\alpha=1}^n \{ (\mu_R^\alpha - \pi^\alpha) \dot{\varphi}_R^\alpha + \Xi^\alpha \cdot \nabla \dot{\varphi}_R^\alpha - \mathbf{J}_R^\alpha \cdot \nabla \mu_R^\alpha - \mu_R^\alpha s_{\text{int}}^\alpha \}. \quad (5.51)$$

The dissipation inequality can be expressed as

$$\begin{aligned} \delta & \stackrel{\text{def}}{=} \mathbf{T}_R : \dot{\mathbf{F}} + \sum_{\alpha=1}^n \{ (\mu_R^\alpha - \pi^\alpha) \dot{\varphi}_R^\alpha + \Xi^\alpha \cdot \nabla \dot{\varphi}_R^\alpha - \mathbf{J}_R^\alpha \cdot \nabla \mu_R^\alpha - \mu_R^\alpha s_{\text{int}}^\alpha \} \\ & - \dot{\psi} \geq 0. \end{aligned} \quad (5.52)$$

where we can split the inequality into the local

$$\delta_l \stackrel{\text{def}}{=} \mathbf{T}_R : \dot{\mathbf{F}} + \sum_{\alpha=1}^n \{ (\mu_R^\alpha - \pi^\alpha) \dot{\varphi}_R^\alpha + \boldsymbol{\Xi}^\alpha \cdot \nabla \dot{\varphi}_R^\alpha - \mu_R^\alpha s_{\text{int}}^\alpha \} - \dot{\psi} \geq 0 \quad (5.53)$$

and diffusional contributions

$$\delta_d \stackrel{\text{def}}{=} - \sum_{\alpha=1}^n \mathbf{J}_R^\alpha \cdot \nabla \mu_R^\alpha. \quad (5.54)$$

5.3 Constitutive relations and Coleman-Noll procedure

Throughout the derivation of the constitutive behaviour of the multicomponent solid, we use the Larché-Cahn derivative expressed by (4.21) together with the mass constraint given by (5.24). We assume the following constitutive dependency of the free energy ψ

$$\psi = \hat{\psi}(\boldsymbol{\varphi}_R, \nabla \boldsymbol{\varphi}_R, \mathbf{F}) = \hat{\psi}^{ch}(\boldsymbol{\varphi}_R, \nabla \boldsymbol{\varphi}_R) + \hat{\psi}^{el}(\mathbf{F}^e(\mathbf{F}, \boldsymbol{\varphi}_R)). \quad (5.55)$$

The objectivity principle requires the constitutive relation (5.55) to be invariant under a superposed rigid body motion or equivalently, independent of the observer. We can relate two different displacement fields χ and χ^* as follows

$$\chi^*(\mathbf{X}, t) = \mathbf{Q}(t)\chi(\mathbf{X}, t) + \mathbf{c}(t) \quad (5.56)$$

where $\mathbf{Q}(t)$ represents a rotation tensor and $\mathbf{c}(t)$ the relative translations. Therefore, the transformation of the potential (5.55) following (5.56) implies

$$\psi = \hat{\psi}(\boldsymbol{\varphi}_R, \nabla \boldsymbol{\varphi}_R, \mathbf{F}) = \bar{\psi}(\boldsymbol{\varphi}_R, \nabla \boldsymbol{\varphi}_R, \mathbf{C}) \quad (5.57)$$

which ensures consistency with the dissipation inequality (5.52) and the principle of frame-indifference.

We use the Coleman-Noll procedure [104], which finds necessary and sufficient conditions that ensure the dissipation inequality (5.52) is satisfied by arbitrary solutions of the underlying balance laws, to find a set of constitutive equations as a pair of each kinematic process. We then rewrite (5.52) following (5.55) as

$$\begin{aligned} & \left(\mathbf{T}_R - \frac{\partial \hat{\psi}}{\partial \mathbf{F}} \right) : \dot{\mathbf{F}} + \sum_{\alpha=1}^n \left(\mu_R^\alpha - \pi^\alpha - \frac{\partial \hat{\psi}}{\partial \varphi_R^\alpha} \right) \dot{\varphi}_R^\alpha \\ & + \sum_{\alpha=1}^n \left(\boldsymbol{\Xi}^\alpha - \frac{\partial \hat{\psi}}{\partial \nabla \varphi_R^\alpha} \right) \cdot \nabla \dot{\varphi}_R^\alpha - \sum_{\alpha=1}^n \{ \mathbf{J}_R^\alpha \cdot \nabla \mu_R^\alpha + \mu_R^\alpha s_{\text{int}}^\alpha \} \geq 0. \end{aligned} \quad (5.58)$$

Therefore, it is possible to find arbitrary values for $\dot{\mathbf{F}}$, $\dot{\varphi}_{\mathbf{R}}^\alpha$, $\nabla\dot{\varphi}_{\mathbf{R}}^\alpha$, and $\nabla\mu_{\mathbf{R}}^\alpha$ at a given time and position such that (5.58) always hold.

The relative chemical potential $\mu_{\mathbf{R}\sigma}^\alpha$ results from the Larché-Cahn derivative as a consequence of incorporating the mass constraint given by Equation (5.24). According to Larché-Cahn [38], the relative chemical potential expresses the chemical potential of α -th species measured relative to the chemical potential of σ -th species. This definition entails that, for saturated systems, the mass constraint given by Equation (5.24) must always hold. Analogously, the relative microforce Ξ_σ^α emerges from the constraint imposed in the concentration gradients, i.e., Equation (5.25). As a consequence, we rewrite (5.58) in the Larché-Cahn sense the following terms: $\pi^\alpha := \pi_\sigma^\alpha$, $\mu^\alpha := \mu_{\mathbf{R}\sigma}^\alpha$ and $\Xi^\alpha := \Xi_\sigma^\alpha$ as well as the material mass fluxes $\mathbf{J}_{\mathbf{R}}^\alpha := \mathbf{J}_{\mathbf{R}\sigma}^\alpha$ as all these quantities are expressed relative to the σ -th reference species. Thus, the energy imbalance is

$$\begin{aligned} \left(\mathbf{T}_{\mathbf{R}} - \frac{\partial\hat{\psi}}{\partial\mathbf{F}} \right) : \dot{\mathbf{F}} + \sum_{\alpha=1}^n \left(\mu_{\mathbf{R}\sigma}^\alpha - \pi_\sigma^\alpha - \frac{\partial^{(\sigma)}\hat{\psi}}{\partial\varphi_{\mathbf{R}}^\alpha} \right) \dot{\varphi}_{\mathbf{R}}^\alpha \\ + \sum_{\alpha=1}^n \left(\Xi_\sigma^\alpha - \frac{\partial^{(\sigma)}\hat{\psi}}{\partial\nabla\varphi_{\mathbf{R}}^\alpha} \right) \cdot \nabla\dot{\varphi}_{\mathbf{R}}^\alpha - \sum_{\alpha=1}^n \mathbf{J}_{\mathbf{R}\sigma}^\alpha \cdot \nabla\mu_{\mathbf{R}\sigma}^\alpha \geq 0. \end{aligned} \quad (5.59)$$

The latter implies that the following relations must hold to keep consistency with the dissipation imbalance

$$\mathbf{T}_{\mathbf{R}} = \frac{\partial\hat{\psi}}{\partial\mathbf{F}}, \quad (5.60a)$$

$$\pi_\sigma^\alpha = \mu_{\mathbf{R}\sigma}^\alpha - \frac{\partial^{(\sigma)}\hat{\psi}}{\partial\varphi_{\mathbf{R}}^\alpha}, \quad (5.60b)$$

$$\Xi_\sigma^\alpha = \frac{\partial^{(\sigma)}\hat{\psi}}{\partial\nabla\varphi_{\mathbf{R}}^\alpha}. \quad (5.60c)$$

We use a logarithmic multi-well potential together with a multi-gradient-type potential for the chemical energy, that is,

$$\begin{aligned} \hat{\psi}^{ch}(\varphi_{\mathbf{R}}, \nabla\varphi_{\mathbf{R}}) = N_v k_B \vartheta \left(\sum_{\alpha=1}^n \varphi_{\mathbf{R}}^\alpha \ln \varphi_{\mathbf{R}}^\alpha \right) + N_v \sum_{\alpha=1}^n \sum_{\beta=1}^n \Omega^{\alpha\beta} \varphi_{\mathbf{R}}^\alpha \varphi_{\mathbf{R}}^\beta \\ + \frac{1}{2} \sum_{\alpha=1}^n \sum_{\beta=1}^n \Gamma^{\alpha\beta} \nabla\varphi_{\mathbf{R}}^\alpha \cdot \nabla\varphi_{\mathbf{R}}^\beta. \end{aligned} \quad (5.61)$$

This expression corresponds to the extension of former Cahn-Hilliard equation towards multicomponent systems [32, 46]. The Ginzburg-Landau free energy governs the dynamics of the phase separation process undergoing spinodal decomposition. Table 5.1 resumes the physical parameters used in the multicomponent framework.

Table 5.1: Physical parameters for the multicomponent system

Physical parameter	Name
N_v	Number of molecules per unit volume
k_B	Boltzmann constant
$\Omega^{\alpha\beta}$	Interaction energy between the α -th and β -th species
$\Gamma^{\alpha\beta}$	Interfacial energy between the α -th and β -th species
ϑ	Absolute temperature

Following [35], we assume the elastic solid behaves as a compressible neo-Hookean whose elastic energy is given by

$$\hat{\psi}^{el}(\mathbf{F}^e) = \frac{G}{2} [\mathbf{F}^e : \mathbf{F}^e - 3] + \frac{G}{\beta} [(\det \mathbf{F}^e)^{-\beta} - 1] \quad (5.62)$$

where G and β are material parameters that relate the shear modulus and the weak compressibility of the material. β is a function of Poisson ratio ν such that $\beta = 2\nu/1 - 2\nu$. In line with treatments of thermoelasticity, we assume a multiplicative decomposition of the deformation gradient [35], that is,

$$\mathbf{F}^e = \mathbf{F}^\varphi \mathbf{F}, \quad (5.63a)$$

$$\mathbf{F}^\varphi = \left(1 + \sum_{\alpha=1}^n \omega^\alpha (\varphi_{\mathbf{R}}^\alpha - \varphi_{\mathbf{R}0}^\alpha) \right)^{-\frac{1}{3}} \mathbf{I} \quad (5.63b)$$

$$\mathbf{F}^\varphi = J_\varphi^{-\frac{1}{3}} \mathbf{I} \quad (5.63c)$$

This expression suggests that as long as the local species concentrations change with respect to the initial distribution, the solid must undergo elastic deformation. Moreover, the swelling material parameter ω_α is related to the crystalline structure of the solid and its mechanical properties.

The evolution of the conserved field $\varphi_{\mathbf{R}}^\alpha$ obeys a non-Fickian diffusion driven by the chemical potential differences between the species. Combining the expression (5.60b) and (5.60c) by means of the balance of conservation of microforces (5.36) and given the constitutive relation for the free energy (5.55), the relative chemical potential of the α -th species can be expressed as

$$\mu_{\mathbf{R}\sigma}^\alpha = \frac{\partial^{(\sigma)} \hat{\psi}}{\partial \varphi_{\mathbf{R}}^\alpha} - \text{Div} \frac{\partial^{(\sigma)} \hat{\psi}}{\partial \nabla \varphi_{\mathbf{R}}^\alpha} - (\gamma^\alpha + \gamma^\sigma) \quad (5.64)$$

and therefore,

$$\begin{aligned} \mu_{R\sigma}^\alpha &= N_v k_B \vartheta \left(\ln \frac{\varphi_R^\alpha}{\varphi_R^\sigma} \right) + 2N_v \sum_{\beta=1}^n (\Omega^{\alpha\beta} - \Omega^{\sigma\beta}) \varphi_R^\beta \\ &\quad - \sum_{\beta=1}^N (\Gamma^{\alpha\beta} - \Gamma^{\sigma\beta}) \operatorname{Div} \nabla \varphi_R^\beta - \frac{1}{3} \omega_\sigma^\alpha J_\varphi^{-1} \operatorname{tr}[\mathbf{T}_R \mathbf{F}^\top] - (\gamma^\alpha + \gamma^\sigma) \end{aligned} \quad (5.65)$$

where

$$\omega_\sigma^\alpha = \omega^\alpha - \omega^\sigma. \quad (5.66)$$

We define $p := -\frac{1}{3} \operatorname{tr}[\mathbf{T}_R \mathbf{F}^\top]$ as the mechanical pressure and emphasize that this pressure modifies the mass transport rate. Therefore, for deformable bodies undergoing mass transport, this physical quantity alters the driving force of the chemical process. Furthermore, we define $p_\varphi^\alpha := \omega_\sigma^\alpha J_\varphi^{-1} p$ as a mechanical pressure scaled by the local variation of α -th species. Thus, we rewrite (5.65) as

$$\begin{aligned} \mu_{R\sigma}^\alpha &= N_v k_B \vartheta \left(\ln \frac{\varphi_R^\alpha}{\varphi_R^\sigma} \right) + 2N_v \sum_{\beta=1}^n (\Omega^{\alpha\beta} - \Omega^{\sigma\beta}) \varphi_R^\beta \\ &\quad - \sum_{\beta=1}^N (\Gamma^{\alpha\beta} - \Gamma^{\sigma\beta}) \operatorname{Div} \nabla \varphi_R^\beta + p_\varphi^\alpha - (\gamma^\alpha + \gamma^\sigma) \end{aligned} \quad (5.67)$$

For convenience, we split the chemical potential $\mu_{R\sigma}^\alpha$ such that $\mu_{R\sigma}^\alpha = \mu_\varphi^\alpha + \mu_s^\alpha + p_\varphi^\alpha$. Thereby,

$$\begin{aligned} \mu_\varphi^\alpha &= N_v k_B \vartheta \left(\ln \frac{\varphi_R^\alpha}{\varphi_R^\sigma} \right) + 2N_v \sum_{\beta=1}^n (\Omega^{\alpha\beta} - \Omega^{\sigma\beta}) \varphi_R^\beta - (\gamma^\alpha + \gamma^\sigma), \\ \mu_s^\alpha &= - \sum_{\beta=1}^N (\Gamma^{\alpha\beta} - \Gamma^{\sigma\beta}) \operatorname{Div} \nabla \varphi_R^\beta, \\ p_\varphi^\alpha &= -\frac{1}{3} \omega_\sigma^\alpha J_\varphi^{-1} \operatorname{tr}[\mathbf{T}_R \mathbf{F}^\top]. \end{aligned} \quad (5.68)$$

The constitutive relation for the Piola-Kirchhoff stress tensor is

$$\mathbf{T}_R = G J_\varphi^{-1/3} [\mathbf{F}^e - (\det \mathbf{F}^e)^{-\beta} \mathbf{F}^{e-\top}] \quad (5.69)$$

As mentioned before, the species fluxes are given by

$$\mathbf{J}_{R\sigma}^\alpha \stackrel{\text{def}}{=} - \sum_{\beta=1}^n \mathbf{M}^{\alpha\beta} J \mathbf{C}^{-1} \nabla \mu_{R\sigma}^\beta \quad (5.70)$$

where $\mathbf{M}^{\alpha\beta}$ are the Onsager mobility coefficients. Moreover, we do not neglect the off-diagonal terms in the Onsager reciprocal relations. We guarantee mass

conservation by imposing the mass fluxes to satisfy

$$\sum_{\alpha=1}^n \mathbf{J}_{R\sigma}^{\alpha} = 0, \quad (5.71)$$

which leads to

$$\sum_{\beta=1}^n M^{\alpha\beta} = 0, \quad \forall \alpha. \quad (5.72)$$

5.4 Dimensionless analysis of the system of chemo-mechanical equations

The couple system of chemo-mechanical equations is given by

$$\begin{aligned} \dot{\varphi}_R^{\alpha} &= s^{\alpha} - \text{Div } \mathbf{J}_{R\sigma}^{\alpha}, \\ \mathbf{J}_{R\sigma}^{\alpha} &= - \sum_{\beta=1}^n M^{\alpha\beta} J C^{-1} \nabla \mu_{R\sigma}^{\beta}, \\ \mu_{R\sigma}^{\alpha} &= \frac{\partial^{(\sigma)} \psi}{\partial \varphi_R^{\alpha}} - \text{Div} \frac{\partial^{(\sigma)} \psi}{\partial (\nabla \varphi_R^{\alpha})} - (\gamma^{\alpha} + \gamma^{\sigma}), \\ s_{\text{int}}^{\alpha} &= - \sum_{c=1}^{N_s} (v_{\alpha c} - \varpi_{\alpha c}) (k_c^+ \prod_{a=1}^n \varsigma^a (\varphi_R^a)^{v_{ac}} - k_c^- \prod_{a=1}^n \varsigma^a (\varphi_R^a)^{\varpi_{ac}}), \\ \text{Div } \mathbf{T}_R + \mathbf{b} &= \mathbf{0}, \\ \mathbf{T}_R &= G J_{\varphi}^{-1/3} [\mathbf{F}^e - (\det \mathbf{F}^e)^{-\beta} \mathbf{F}^{e-\top}], \end{aligned} \quad (5.73)$$

with

$$\begin{aligned} \varphi_R^{\alpha}(\mathbf{X}, 0) &= \varphi_0^{\alpha} && \text{in } \mathbf{P}, \\ \mathbf{u}(\mathbf{X}, 0) &= u_0 && \text{in } \mathbf{P}, \end{aligned} \quad (5.74)$$

subject to periodic boundary conditions.

We use the same definition for s_{int}^{α} as suggested in (4.78). Moreover, we introduce a free energy density $\psi_0 = 2N_v k_B \vartheta$ together with a set of diffusion coefficients $D_{\alpha\beta}$ such that

$$D^{\alpha\beta} = \psi_0 M^{\alpha\beta} \varphi_R^{\alpha} (\delta_{\alpha\beta} - \varphi_R^{\beta}). \quad (5.75)$$

To make dimensionless the energy densities, and the governing and constitutive equations, we define the following dimensionless variables

$$\bar{\mathbf{u}} = u_0^{-1} \mathbf{u} \quad \bar{\mathbf{x}} = L_0^{-1} \mathbf{x} \quad \bar{t} = D_0 \ell_0^2 L_0^{-4} t \quad (5.76)$$

where u_0 , D_0 and ℓ_0 account for a reference deformation state, the diffusion coefficient and interface thickness of a reference species, respectively. We propose the

following sets of scalar and vector dimensionless numbers for the multicomponent chemo-mechanical system, that is,

$$\begin{aligned}\omega^\alpha, \bar{k}_+^c &= k_+^c D_0^{-1} \ell_0^{-2} L_0^4, \quad \bar{k}_-^c = k_-^c D_0^{-1} \ell_0^{-2} L_0^4, \quad \bar{\vartheta}_c^{\alpha\beta} = \vartheta^{-1} \vartheta_c^{\alpha\beta}, \\ \bar{\ell}^{\alpha\beta} &= L_0^{-1} \ell^{\alpha\beta}, \quad \bar{\psi} = \hat{\psi} \psi_0^{-1}, \quad \bar{\sigma}^{\alpha\beta} = \sigma^{\alpha\beta} (\psi_0 L_0)^{-1}, \quad \beta, \quad \bar{\mathbf{b}} = G^{-1} \mathbf{b}, \\ \bar{G} &= G \psi_0^{-1}, \quad l = u_0 L_0^{-1}, \quad \bar{D}^{\alpha\beta} = D^{\alpha\beta} D_0^{-1} \ell_0^{-2} L_0^2, \quad \bar{\gamma}^\alpha = \psi_0^{-1} \gamma^\alpha.\end{aligned}\quad (5.77)$$

By inserting the dimensionless quantities in (5.61) and (5.62), we find the following dimensionless forms of the chemical energy

$$\begin{aligned}\bar{\psi}^{ch}(\boldsymbol{\varphi}_R, \bar{\nabla} \boldsymbol{\varphi}_R) &= \frac{1}{2} \left(\sum_{\alpha=1}^n \varphi_R^\alpha \ln \varphi_R^\alpha \right) + \sum_{\alpha=1}^n \sum_{\beta=1}^n \bar{\vartheta}_c^{\alpha\beta} \varphi_R^\alpha \varphi_R^\beta \\ &+ \frac{1}{2} \sum_{\alpha=1}^n \sum_{\beta=1}^n \bar{\sigma}^{\alpha\beta} \bar{\ell}^{\alpha\beta} \bar{\nabla} \varphi_R^\alpha \cdot \bar{\nabla} \varphi_R^\beta\end{aligned}\quad (5.78)$$

and the mechanical energy

$$\bar{\psi}^{el}(\bar{\mathbf{F}}^e) = \bar{G} \left\{ \frac{1}{2} [\bar{\mathbf{F}}^e : \bar{\mathbf{F}}^e - 3] + \frac{1}{\beta} [(\det \bar{\mathbf{F}}^e)^{-\beta} - 1] \right\} \quad (5.79)$$

where $\bar{\mathbf{F}}^e = J_\varphi^{-1/3} (\mathbf{I} + l \bar{\nabla} \bar{\mathbf{u}})$.

Likewise, the dimensionless forms of the governing and constitutive equations read

$$\begin{aligned}\frac{\partial \varphi_R^\alpha}{\partial \bar{t}} &= \bar{\nabla} \cdot \left(\sum_{\beta=1}^n \bar{D}^{\alpha\beta} \bar{\mathbf{M}} \bar{\nabla} \bar{\mu}_{R\sigma}^\beta \right) + \bar{s}^\alpha, \\ \bar{\mathbf{M}} &= \det(\mathbf{I} + l \bar{\nabla} \bar{\mathbf{u}}) (\mathbf{I} + l \bar{\nabla} \bar{\mathbf{u}})^{-1} \mathbf{I} (\mathbf{I} + l \bar{\nabla} \bar{\mathbf{u}})^{-\top}, \\ \bar{\mu}_{R\sigma}^\alpha &= \frac{1}{2} \left(\ln \frac{\varphi_R^\alpha}{\varphi_R^\sigma} \right) + 2 \sum_{\beta=1}^n (\bar{\vartheta}_c^{\alpha\beta} - \bar{\vartheta}_c^{\sigma\beta}) \varphi_R^\beta - \sum_{\beta=1}^N (\bar{\sigma}^{\alpha\beta} \bar{\ell}^{\alpha\beta} - \bar{\sigma}^{\sigma\beta} \bar{\ell}^{\sigma\beta}) \bar{\Delta} \varphi_R^\beta \\ &- \frac{1}{3} \omega^{\alpha\sigma} J_\varphi^{-1} \bar{G} \text{tr}[\bar{\mathbf{T}}_R (\mathbf{I} + l \bar{\nabla} \bar{\mathbf{u}})^\top] - (\bar{\gamma}^\alpha + \bar{\gamma}^\sigma), \\ \bar{s}_{\text{int}}^\alpha &= - \sum_{c=1}^{n_s} \left\{ (v^{c\alpha} - \varpi^{c\alpha}) (\bar{k}_+^c \prod_{a=1}^n (\varphi_R^a)^{v^{ca}} - \bar{k}_-^c \prod_{a=1}^n (\varphi_R^a)^{\varpi^{ca}}) \right\}, \\ \text{Div} \bar{\mathbf{T}}_R + \bar{\mathbf{b}} &= \mathbf{0}, \\ \bar{\mathbf{T}}_R &= J_\varphi^{-1/3} [J_\varphi^{\frac{1}{3}} (\mathbf{I} + l \bar{\nabla} \bar{\mathbf{u}}) - (\det J_\varphi^{\frac{1}{3}} (\mathbf{I} + l \bar{\nabla} \bar{\mathbf{u}}))^{-\beta} (J_\varphi^{\frac{1}{3}} (\mathbf{I} + l \bar{\nabla} \bar{\mathbf{u}}))^{-\top}].\end{aligned}\quad (5.80)$$

subjected to the boundary conditions (5.74).

Chapter 6

Numerical simulation

6.1 Reaction-diffusion process of a four phases system

The following numerical results, discussion, and conclusions are reported in the manuscript "Reactive n -species Cahn–Hilliard system: A thermodynamically-consistent model for reversible chemical reaction" [45]. Copyright clearances from the Journal of Computational and Applied Mathematics (JCAM) and the authors to use the material in this thesis can be found in Appendix A.

We perform a numerical simulation of a two-dimensional multicomponent Cahn-Hilliard reactive equation that showcases the temporal evolution and interactions of a four species system φ^1 , φ^2 , φ^3 and φ^4 as expressed by the model we propose in the previous sections. Herein, we consider a reversible chemical reaction with forward k^+ and backward k^- reaction rates of 1000 and 10, respectively [45]. The chemical reaction in our formulation is general. Therefore, modelling a specific chemical process generates neither implementation nor theoretical difficulties. By inserting the corresponding stoichiometry coefficients and reaction rates, our model is capable of representing arbitrary processes. We consider the following chemical reaction,



where the stoichiometry vectors $v^{\alpha\beta}$ and $\varpi^{\alpha\beta}$ are given by

$$v^{\alpha\beta} = (5, 1, 0, 0), \quad \text{and} \quad \varpi^{\alpha\beta} = (0, 0, 2, 1). \quad (6.2)$$

As a pointed out in §4.2, the temporal evolution of the conserved field undergoing spinodal decomposition with chemical reaction is governed by

$$\dot{\varphi}^\alpha = s^\alpha - \operatorname{div} \mathbf{j}^\alpha. \quad (6.3)$$

We denote H^2 as the Sobolev space of square integrable functions with square integrable first and second derivatives and $(\cdot, \cdot)_{\mathcal{P}}$ as the L^2 inner product over the physical domain \mathcal{P} with boundary \mathcal{S} [45]. By multiplying the governing equation (6.3) by a test function ϱ^α , which belongs to H^2 , using the definition for the mass fluxes (4.94) and integrating by parts, the primal variational formulation can then be given by:

$$\begin{aligned} (\varrho^\alpha, \dot{\varphi}^\alpha)_{\mathcal{P}} &= (\varrho^\alpha, s^\alpha)_{\mathcal{P}} - (\varrho^\alpha, \mathbf{j}_{i,i}^\alpha)_{\mathcal{P}} \\ &= (\varrho^\alpha, s^\alpha)_{\mathcal{P}} + (\varrho_{,i}^\alpha, \mathbf{j}_i^\alpha)_{\mathcal{P}} - (\varrho^\alpha, \mathbf{j}_i^\alpha \mathbf{n}_i)_{\mathcal{S}} \\ &= (\varrho^\alpha, s^\alpha)_{\mathcal{P}} + (\varrho_{,i}^\alpha, -\mathbf{M}^{\alpha\beta}(\mu_\varphi^\beta + \mu_s^\beta)_{,i})_{\mathcal{P}} \\ &\quad - (\varrho^\alpha, -\mathbf{M}^{\alpha\beta}(\mu_{,i}^\beta) \mathbf{n}_i)_{\mathcal{S}} \\ &= (\varrho^\alpha, s^\alpha)_{\mathcal{P}} - (\varrho_{,i}^\alpha, \mathbf{M}^{\alpha\beta} \mu_{\varphi,i}^\beta)_{\mathcal{P}} - (\varrho_{,i}^\alpha, (\mathbf{M}^{\alpha\beta} \mu_s^\beta)_{,i})_{\mathcal{P}} \\ &\quad + (\varrho_{,i}^\alpha, (\mathbf{M}_{,i}^{\alpha\beta}) \mu_s^\beta)_{\mathcal{P}} + (\varrho^\alpha, \mathbf{M}^{\alpha\beta}(\mu_{,i}^\beta) \mathbf{n}_i)_{\mathcal{S}} \\ &= (\varrho^\alpha, s^\alpha)_{\mathcal{P}} - (\varrho_{,i}^\alpha, \mathbf{M}^{\alpha\beta} \mu_{\varphi,i}^\beta)_{\mathcal{P}} + (\varrho_{,ii}^\alpha, \mathbf{M}^{\alpha\beta} \mu_s^\beta)_{\mathcal{P}} \\ &\quad + (\varrho_{,i}^\alpha, (\mathbf{M}_{,i}^{\alpha\beta}) \mu_s^\beta)_{\mathcal{P}} + (\varrho^\alpha, \mathbf{M}^{\alpha\beta}(\mu_{,i}^\beta) \mathbf{n}_i)_{\mathcal{S}} \\ &\quad - (\varrho_{,i}^\alpha \mathbf{n}_i, \mathbf{M}^{\alpha\beta} \mu_s^\beta)_{\mathcal{S}} \end{aligned} \quad (6.4)$$

In a reversible chemical reaction, the reactant and product species are never totally consumed. For instance, in equation (6.1), the species φ^1 and φ^2 react to form the species φ^3 and φ^4 which in turn react to form back the species φ^1 and φ^2 until the system reaches equilibrium [45]. In general, such reactions do not need to have the same reaction rates. Thereby, we seek to model a system which follows a reversible chemical reaction such as (6.1).

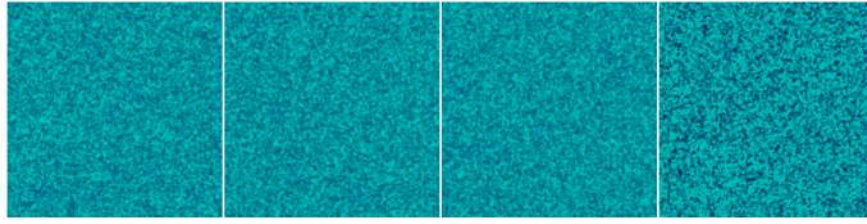
Regarding the physical parameters that rule the spinodal decomposition, we set the interaction energy as

$$\Omega^{\alpha\beta} = \begin{bmatrix} 0.0 & 0.5 & 0.7 & 0.6 \\ 0.5 & 0.0 & 0.4 & 0.7 \\ 0.7 & 0.4 & 0.0 & 0.7 \\ 0.6 & 0.7 & 0.7 & 0.0 \end{bmatrix} \quad (6.5)$$

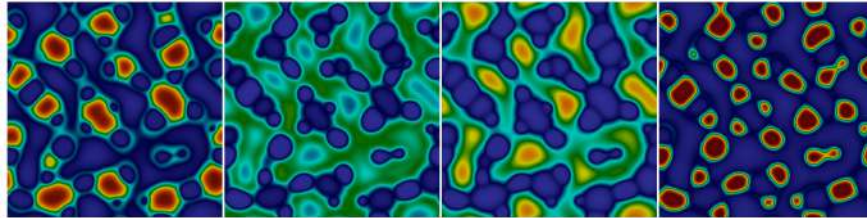
Moreover, the magnitude of the interfacial energy between φ^α and φ^β is

$$\Gamma^{\alpha\beta} = \begin{bmatrix} 0.0 & -0.5 & -0.75 & -0.75 \\ -0.5 & 0.0 & -0.45 & -0.65 \\ -0.75 & -0.45 & 0.0 & -0.75 \\ -0.75 & -0.65 & -0.75 & 0.0 \end{bmatrix} \quad (6.6)$$

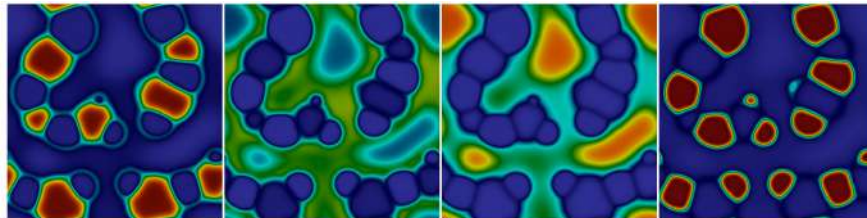
For instance, the magnitude of the interfacial energy between φ_1 and φ_3 corresponds to -0.75 .



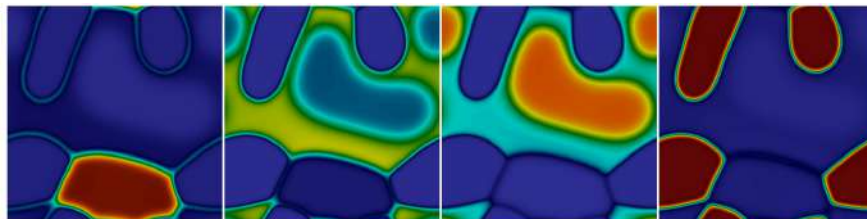
(a) Initial condition



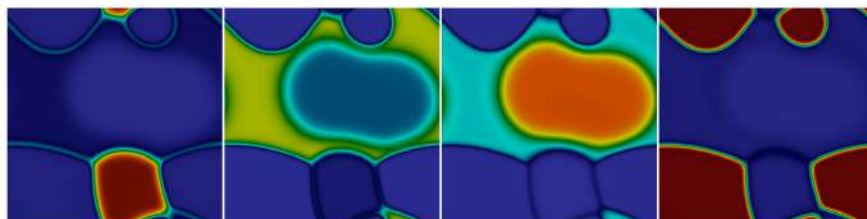
(b) $t = 6 \times 10^{-5}$



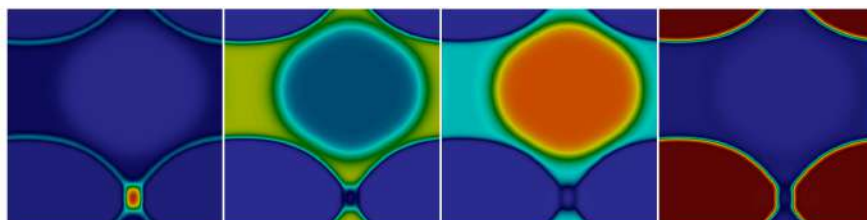
(c) $t = 1 \times 10^{-3}$



(d) $t = 5 \times 10^{-3}$



(e) $t = 1 \times 10^{-2}$



(f) $t = 3 \times 10^{-2}$

Figure 6.1 Temporal evolution of the concentration for species $\hat{\varphi}^1$, $\hat{\varphi}^2$, $\hat{\varphi}^3$, and $\hat{\varphi}^4$, respectively

The parameters $N_v k_B \vartheta$ and N_v take the values of 9000 and 6000, respectively. Furthermore, the initial condition for each component is set such that φ^α takes random values between $\bar{\varphi}^\alpha \pm 0.05$, assuming that $\bar{\varphi}^\alpha$ is $1/n$. As discussed above, we calculate φ^n by applying at each time-step the constraint defined by (4.6), which guarantees the consistency of the process. The coupled system of partial differential equations for our example computes four coupled concentrations corresponding to $[\dot{\varphi}^\alpha] = \varphi^\alpha$, for $\alpha = 1, \dots, 4$, that evolve in time, is

$$\dot{\varphi}^1 = -5k_+(\varphi^1)^5\varphi^2 + 5k_-(\varphi^3)^2\varphi^4 - \text{div}\mathbf{j}_4^1, \quad (6.7a)$$

$$\dot{\varphi}^2 = -k_+(\varphi^1)^5\varphi^2 + k_-(\varphi^3)^2\varphi^4 - \text{div}\mathbf{j}_4^2, \quad (6.7b)$$

$$\dot{\varphi}^3 = 2k_+(\varphi^1)^5\varphi^2 - 2k_-(\varphi^3)^2\varphi^4 - \text{div}\mathbf{j}_4^3. \quad (6.7c)$$

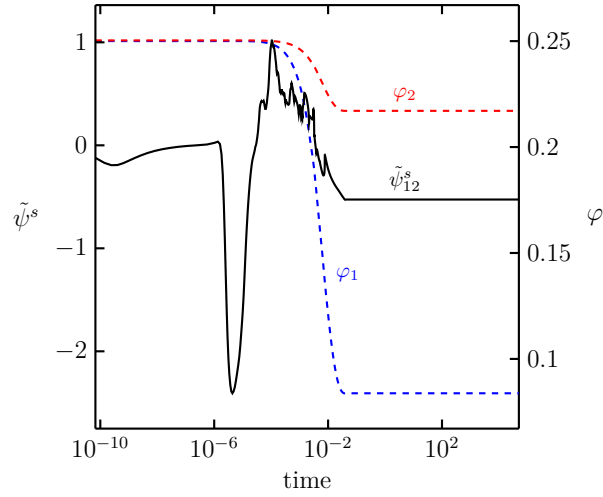
In (6.7), we use the Larché–Cahn derivative with $\dot{\varphi}^4$ as the reference species. We form and solve the system of equations using PetIGA [105], an open source framework for high-performance computing which has proven flexible, robust and highly scalable. This framework was applied to various multiphysics and multi-scale processes, in particular phase-field modeling applications [106–114]. Following [90], we use isogeometric analysis to discretize in space equation (6.4). This technique successfully solves the standard Cahn–Hilliard equation in primal form as it allows for high-order, and highly-continuous basis functions, i.e., H^2 -conforming spaces. We use a square domain $\mathcal{P} = [0, 1]^2$, using 64 C^1 -quadratic elements with periodic boundary conditions. In order to control possible numerical instabilities induced by the time discretization, we use the generalized- α method as suggested by Vignal et al. [115].

Figure 6.1 presents the temporal evolution of the concentration of each component. The randomly perturbed initial condition goes through spinodal decomposition during the early stages and is followed by coarsening. Our results highlight these phenomena including the reaction process. Figures 6.1-(b) and 6.1-(c) depict the early stages of the process, $t < 10^{-3}$, when chain structures are formed by components $\dot{\varphi}^1$ and $\dot{\varphi}^4$, whereas the components $\dot{\varphi}^2$ and $\dot{\varphi}^3$ play an interstitial role. Later on, $t > 10^{-3}$, a merging process takes place to form large and rounded structures. When the system reaches steady state, the component $\dot{\varphi}^1$ forms a bridge at the interface of the two elliptical structures defined by component $\dot{\varphi}^4$. Furthermore, the component $\dot{\varphi}^2$ becomes the interstitial component, while the component $\dot{\varphi}^3$ forms a circular structure, surrounded by the component $\dot{\varphi}^4$ [45].

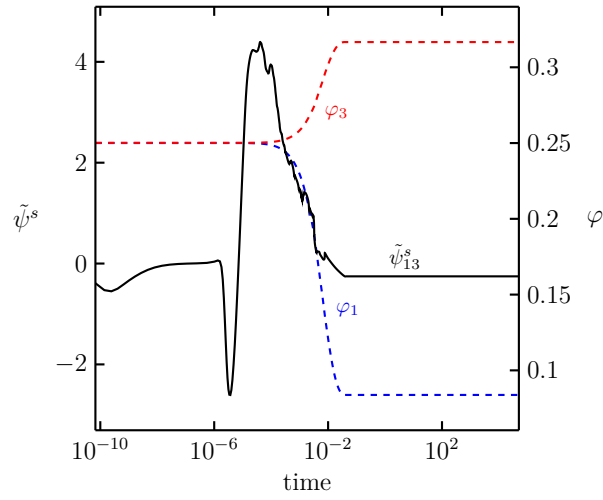
Figures 6.2 and 6.3 depicts the interfacial energy pair (solid black lines) and the masses of each component (red and blue dashed lines). The chemical reactions

occur mainly in the range $10^{-3} < t < 10^{-2}$, and outside this range the mass of each component remains roughly constant. Since the backward reaction plays no substantial role in the process, due to the fact that $k^+ \gg k^-$, components φ^1 and φ^2 react decreasing their initial masses. Consequently, this reaction increases the masses of the components φ^3 and φ^4 as a function of the consumption of reactant components. The nature of a system undergoing chemical reactions can create (destroy) the interface between the phases. Thus, the interfacial energy must also change according to this evolution process. Particularly, Figure 6.3-(a) illustrates this process, whereby the interfacial energy grows as a result of the emerging product phase. On the contrary, when considering the early stages of each phase, Figure 6.2 and 6.3 suggest that the spinodal decomposition controls the interfacial energy evolution since the chemical process plays no substantial role during this early process. The relation between the free-energy and the external power, $\dot{\psi} - \sum_a^n (\text{grad } \mu^\alpha \cdot \mathbf{j}^\alpha) = \dot{w}^{ext}$, bearing in mind that the use periodic boundary conditions renders $\dot{w}^{ext} = - \sum_a^n \mu^\alpha s^\alpha$, suggests the reaction term may act as either source or sink of energy, explaining the growth observed in the free-energy. Therefore, this reaction may increase the free energy. Figure 6.4 provides a picture of such behaviour [45].

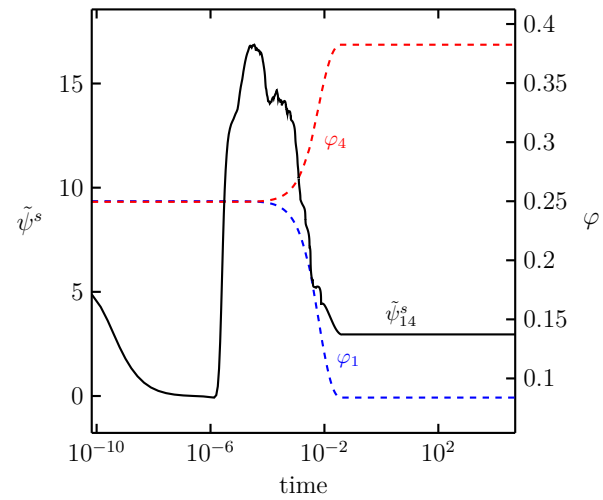
The spinodal decomposition controls the early stages since the phases start separating (unmixing) from each other. Later on, the system favors the growth of regions rich in each component caused by either phase merging or Ostwald ripening. Figure 6.4 shows the evolution over time of the total free-energy functional depicting the concentration fields at four stages, that is, the initial condition, spinodal decomposition, coarsening at the beginning of the chemical reaction, at the end of the chemical reaction, and the steady state [45].



(a) Interfacial energy for components $\dot{\varphi}^1$ and $\dot{\varphi}^2$

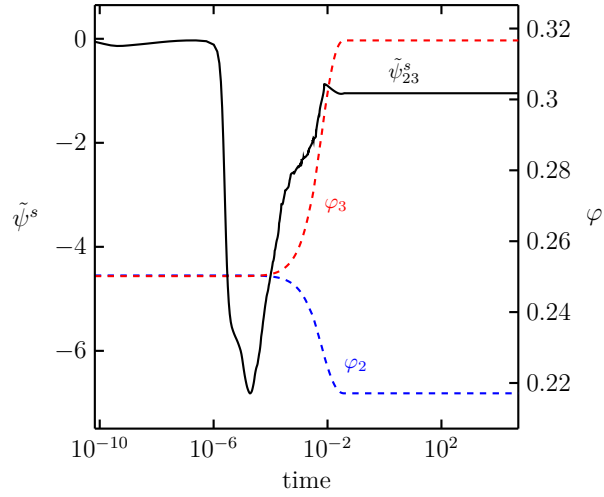


(b) Interfacial energy for components $\dot{\varphi}^1$ and $\dot{\varphi}^3$

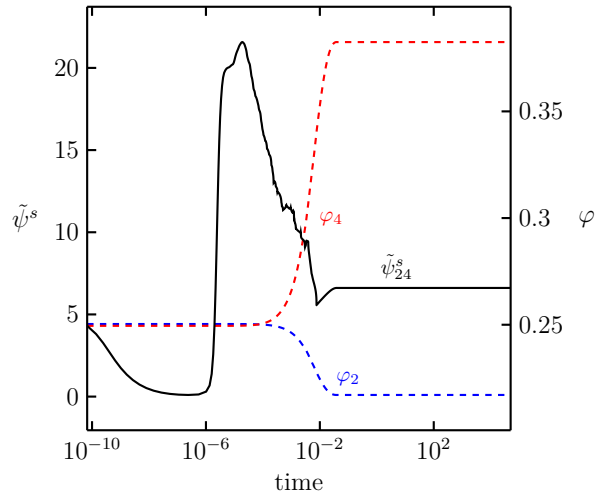


(c) Interfacial energy for components $\dot{\varphi}^1$ and $\dot{\varphi}^4$

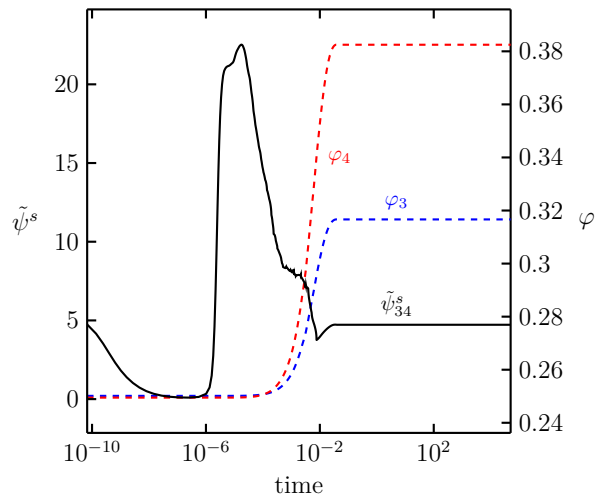
Figure 6.2 Temporal evolution of interfacial energies and masses for $\dot{\varphi}^1$ – $\dot{\varphi}^2$, $\dot{\varphi}^1$ – $\dot{\varphi}^3$, and $\dot{\varphi}^1$ – $\dot{\varphi}^4$, respectively



(a) Interfacial energy for components $\dot{\varphi}^2$ and $\dot{\varphi}^3$



(b) Interfacial energy for components $\dot{\varphi}^2$ and $\dot{\varphi}^4$



(c) Interfacial energy for components $\dot{\varphi}^3$ and $\dot{\varphi}^4$

Figure 6.3 Temporal evolution of interfacial energies and masses for $\dot{\varphi}^2$ - $\dot{\varphi}^3$, $\dot{\varphi}^2$ - $\dot{\varphi}^4$, and $\dot{\varphi}^3$ - $\dot{\varphi}^4$, respectively

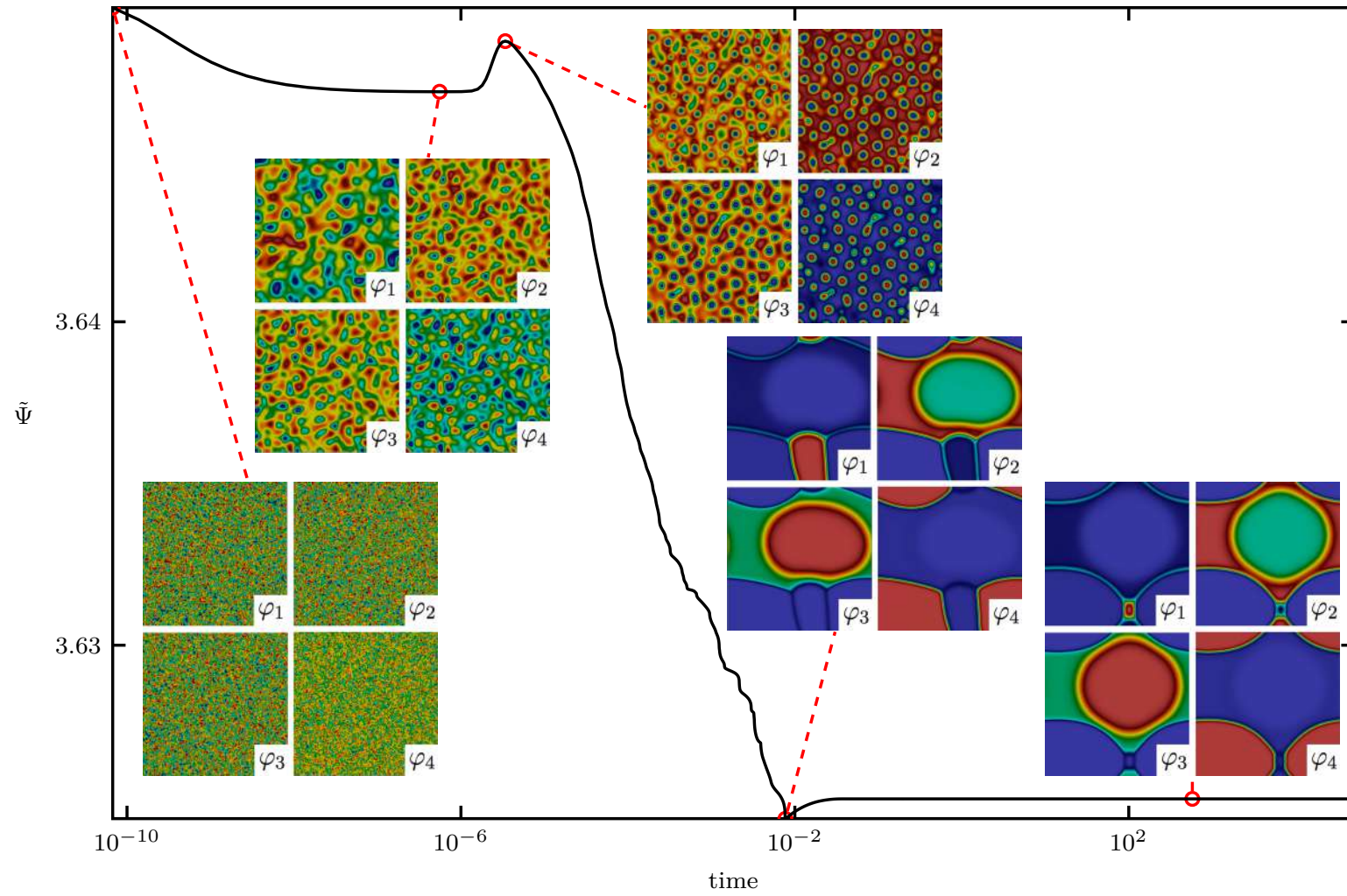


Figure 6.4 Temporal evolution of free energy.

To conclude, we derive a set of conservation laws within the appropriate thermodynamic constraints for a multicomponent Cahn–Hilliard system with multiple reversible chemical reactions. For binary systems, we recover the standard Cahn–Hilliard equation. Additionally, we couple the multi-phase framework with chemical reactions using an ideal mass action law. We perform a numerical simulation with four components and one reversible chemical reaction with different chemical reaction rates that showcases the robustness of the model we propose. The simulation also shows consistency with expected spinodal decomposition as well as the reversible chemical reaction [45].

6.2 The merging of circular inclusions

We now state the problem as: find $\varphi \in \mathcal{C}^4(\mathcal{P})$ such that (4.83) given (4.79) subject to periodic boundary conditions up to the fourth derivative of φ with respect to \mathbf{x} in a square open region $\mathcal{P} = (0, 1) \times (0, 1)$. To do so, we use the PetIGA [116] isogeometric analysis framework and solve this equation in its primal version. We use 256×256 element mesh of a polynomial degree 4 and continuity 3. The initial and boundary conditions are described by

$$\begin{aligned}
 h &= 0.2 \\
 \delta^1 &= 0.31 - 0.8 \left(0.5 \tanh \left(\frac{(x - 0.375)^2 + (y - 0.65)^2 - 0.17^2}{0.01h(h + 1.7)} \right) + 0.5 \right) \\
 \delta^2 &= 0.31 - 0.8 \left(0.5 \tanh \left(\frac{(x - 0.375)^2 + (y - 0.35)^2 - 0.1^2}{0.01h(h + 1.0)} \right) + 0.5 \right) \\
 \varphi_0^1 &= 1 + \delta_1 + \delta_2, \\
 \varphi_0^2 &= 0.999 - \varphi_0^1, \\
 \varphi_0^3 &= 1 - \varphi_0^1 - \varphi_0^2,
 \end{aligned} \tag{6.8}$$

in \mathcal{P} , subject to periodic boundary conditions on $\partial\mathcal{P} \times (0, T)$,

and pictured in figures 6.5a, 6.5b, and 6.5c.

Table 6.1 summarizes the dimensional parameters which render the dimensionless parameters in (6.9).

Table 6.1: Chemical and physical parameters for the three phases system

Physical parameter	Value	Name
ψ_0 [J m ⁻³]	2×10^7	Energy density
L_0 [m]	10^{-6}	Domain length
ϑ [K]	1000.0	Absolute temperature
ϑ_c^{12} [K]	1100.0	Critical temperature between phases 1 and 2
ϑ_c^{13} [K]	1200.0	Critical temperature between phases 1 and 3
ϑ_c^{23} [K]	1300.0	Critical temperature between phases 2 and 3
D [m ² s ⁻¹]	10^{-20}	Diffusion coefficient (same for all phases)
k^+ [m ² s ⁻¹]	10^{-14}	Forward reaction rate
σ^{12} [J m ⁻²]	0.816	Interfacial energy between phases 1 and 2
σ^{13} [J m ⁻²]	0.625	Interfacial energy between phases 1 and 3
σ^{23} [J m ⁻²]	0.921	Interfacial energy between phases 2 and 3
ℓ^{12} [m]	1.5×10^{-8}	Interface thickness between phases 1 and 2
ℓ^{13} [m]	2×10^{-8}	Interface thickness between phases 1 and 3
ℓ^{23} [m]	10^{-8}	Interface thickness between phases 2 and 3

$$\begin{aligned}
 \bar{D}^{\alpha\beta} &= 1 \times 10^4 \begin{bmatrix} 1 & 1 & 1 \\ 1 & 1 & 1 \\ 1 & 1 & 1 \end{bmatrix}, \quad \bar{\vartheta}_c^{\alpha\beta} = \begin{bmatrix} 0 & 1.100 & 1.200 \\ 1.100 & 0 & 1.300 \\ 1.200 & 1.300 & 0 \end{bmatrix}, \\
 \bar{\sigma}^{\alpha\beta} \bar{\ell}^{\alpha\beta} &= -10^{-4} \begin{bmatrix} 0 & 6.121 & 6.250 \\ 6.121 & 0 & 4.605 \\ 6.250 & 4.605 & 0 \end{bmatrix}, \quad v^{\alpha\beta} = \begin{bmatrix} 1 & 1 & 0 \end{bmatrix}, \\
 \varpi^{\alpha\beta} &= \begin{bmatrix} 0 & 0 & 1 \end{bmatrix}, \quad \bar{k}_+ = 0.01,
 \end{aligned} \tag{6.9}$$

where we choose $D_0 = D$ and $\ell_0 = \ell^{23}$ as the reference diffusion coefficient and interface thickness of a reference species, respectively.

We aim to describe configurational tractions as the driven forces in the motion of interfaces in a multicomponent system undergoing reactions. We then describe the configurational traction along a level curve \mathcal{L}_*^α , upon which $\varphi^\alpha = \varphi_*^\alpha$. To do so, we then introduce the normal and tangential coordinates n^α and m^α on \mathcal{L}_*^α , with unit vectors $\boldsymbol{\nu}^\alpha$ and $\boldsymbol{\tau}^\alpha$ defined such that

$$\text{grad } \varphi^\alpha = |\text{grad } \varphi^\alpha| \boldsymbol{\nu}^\alpha, \quad |\boldsymbol{\nu}^\alpha| = 1, \tag{6.10}$$

augmented by a sign convention which ensures that rotating $\boldsymbol{\tau}^\alpha$ clockwise by $\pi/2$ yields $\boldsymbol{\nu}^\alpha$.

To further the understanding of how configurational fields are developed, we portray the configurational tractions $\mathbf{C}_\sigma \boldsymbol{\nu}^\alpha$. In reckoning these tractions in a $\{n, m\}$ -frame, we arrive at

$$\mathbf{C}_\sigma = \zeta \mathbf{1} - \sum_{\alpha=1}^n \{ |\text{grad } \varphi^\alpha| \boldsymbol{\nu}^\alpha \otimes \boldsymbol{\xi}_\sigma^\alpha \}, \quad (6.11)$$

with a free-energy of the form

$$\begin{aligned} \hat{\psi}(\boldsymbol{\varphi}, \text{grad } \boldsymbol{\varphi}) &= f(\varphi^\alpha) + \frac{1}{2} \sum_{\alpha=1}^n \sum_{\beta=1}^n \Gamma^{\alpha\beta} \text{grad } \varphi^\alpha \cdot \text{grad } \varphi^\beta, \\ &= f(\varphi^\alpha) + \frac{1}{2} \sum_{\alpha=1}^n \sum_{\beta=1}^n \Gamma^{\alpha\beta} |\text{grad } \varphi^\alpha| |\text{grad } \varphi^\beta| \boldsymbol{\nu}^\alpha \cdot \boldsymbol{\nu}^\beta, \end{aligned} \quad (6.12)$$

the relative configurational stress \mathbf{C}_σ is then rewritten as

$$\mathbf{C}_\sigma = \zeta \mathbf{1} + \sum_{\alpha=1}^n \left\{ |\text{grad } \varphi^\alpha| \boldsymbol{\nu}^\alpha \otimes \left(\sum_{\beta=1}^n (\Gamma^{\alpha\beta} - \Gamma^{\sigma\beta}) |\text{grad } \varphi^\beta| \boldsymbol{\nu}^\beta \right) \right\}. \quad (6.13)$$

Moreover, the configurational tractions $\mathbf{C}_\sigma \boldsymbol{\nu}^\alpha$ can be specialized to

$$\mathbf{C}_\sigma \boldsymbol{\nu}^\alpha = \left\{ \zeta + \sum_{\hat{\alpha}=1}^n \sum_{\hat{\beta}=1}^n \left((\Gamma^{\hat{\alpha}\hat{\beta}} - \Gamma^{\sigma\hat{\beta}}) |\text{grad } \varphi^{\hat{\alpha}}| |\text{grad } \varphi^{\hat{\beta}}| \boldsymbol{\nu}^{\hat{\alpha}} \otimes \boldsymbol{\nu}^{\hat{\beta}} \right) \right\} \boldsymbol{\nu}^\alpha. \quad (6.14)$$

The relation (6.14) expresses the traction $\mathbf{C}_\sigma \boldsymbol{\nu}^\alpha$ as a linear combination of all unit normals $\boldsymbol{\nu}^{\hat{\alpha}}$ for $1 \leq \hat{\alpha} \leq n$.

To compute all the relative physical and chemical quantities, the relative chemical potential, mass fluxes, microstresses, and byproducts, we set the reaction product as the reference phase. Figure 6.5 pictures the merging process between two circular inclusions of distinct size at early stages, while in figure 6.6 shows the evolution of this system after the merging. From left to right, we present phases 1, 2, and 3, respectively. As the inclusions approach one another, here represented by phase 2, which in turn are embedded in phase 1, the chemical reaction



takes place at the interface between these two phases. The components $\dot{\varphi}^1$ and $\dot{\varphi}^2$ represent the reactant phases, while $\dot{\varphi}^3$ the reaction product.

To understand how the merging process is initiated, we portray the relative configuration traction field. Figure 6.7 presents streamlines of the relative configurational traction $\mathbf{C}_3 \boldsymbol{\nu}^1$, while figure 6.8 depicts the relative configurational

traction $\mathbf{C}_3\nu^2$ field at the same times. In figure 6.10, blue curves are the relative n_σ^α -nullclines of the relative configurational traction $\mathbf{C}_\sigma\nu^\alpha$. In all these figures, the black curve is a level curve \mathcal{L}_0^α upon which $\varphi^\alpha = 0$.

In the streamlines presented in figure 6.7, before and after the merging, we see that these tractions are normal to the interface. Moreover, in figure 6.8a, we observe that the relative configurational traction related to the phase 1, corresponding to the background phase, $\mathbf{C}_3^1\nu^1$, tends to avoid the merging. Conversely and more strongly, the relative configurational traction related to the phase 2, corresponding to the inclusions, $\mathbf{C}_3^2\nu^2$, overcome $\mathbf{C}_3^1\nu^1$ and provoke the merging.

The relative n_σ^α -nullclines surround the interface from both sides guaranteeing the phase segregation, restraining the mass transfer through it. At the initial condition or even at early stages, there are two n_σ^α -nullclines for each phase around every inclusion. They are circular and occurring innerly and outerly to the level curve \mathcal{L}_0^α . When the merging process is initiated, these n_σ^α -nullclines break apart favoring the mass transfer as shown in figure 6.9a and 6.9b. At this stage, there is one n_σ^α -nullcline in each inclusion for each phase and they horseshoe-shaped curves. After the merging, these n_σ^α -nullclines also merge, as pictured in figures 6.9c and 6.9d, and surround the level curve \mathcal{L}_0^α innerly and outerly once again, thus enforcing that no ‘particle’ crosses the interface and ensuring a steady phase segregation.

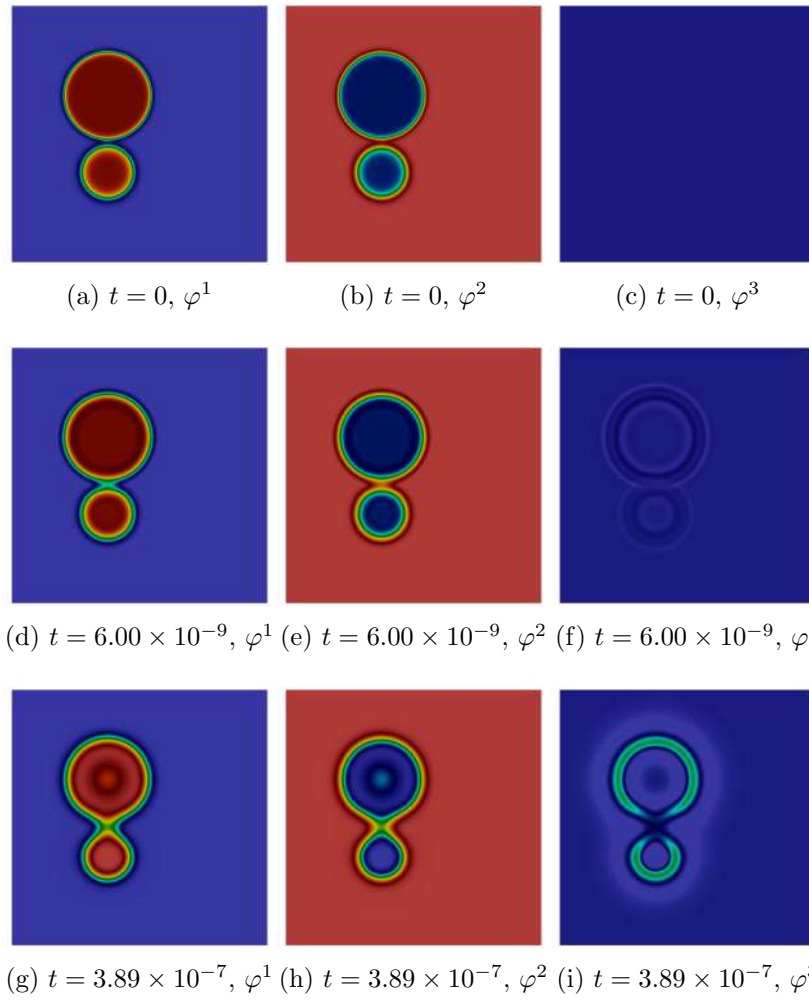
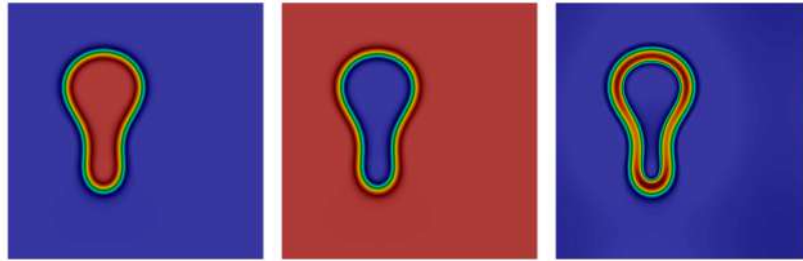
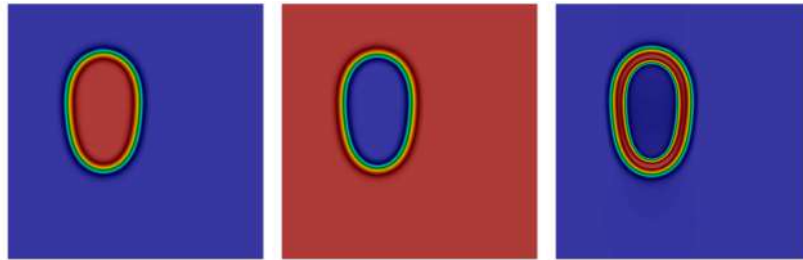


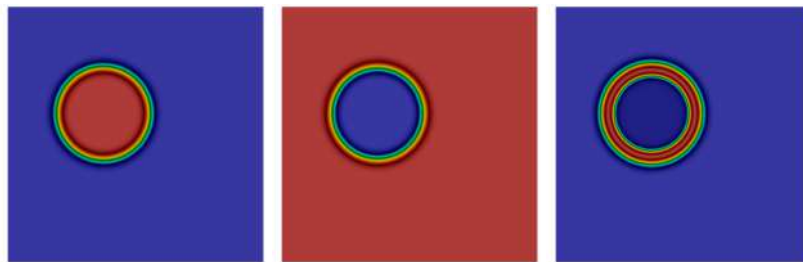
Figure 6.5 Phase-field evolution before the merging. Left: φ^1 ; Middle: φ^2 ; Right: φ^3



(a) $t = 6.77 \times 10^{-6}$, φ^1 (b) $t = 6.77 \times 10^{-6}$, φ^2 (c) $t = 6.77 \times 10^{-6}$, φ^3

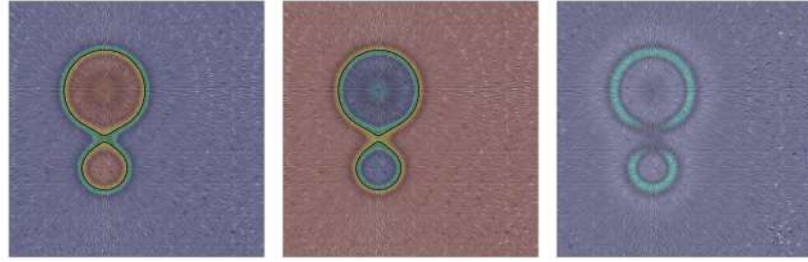


(d) $t = 3.00 \times 10^{-5}$, φ^1 (e) $t = 3.00 \times 10^{-5}$, φ^2 (f) $t = 3.00 \times 10^{-5}$, φ^3

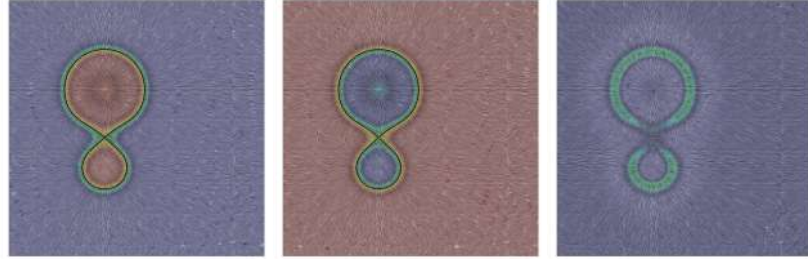


(g) $t = 5.70 \times 10^{-3}$, φ^1 (h) $t = 5.70 \times 10^{-3}$, φ^2 (i) $t = 5.70 \times 10^{-3}$, φ^3

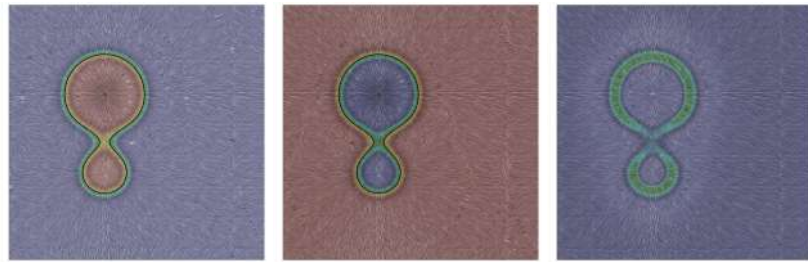
Figure 6.6 Phase-field evolution after the merging. Left: φ^1 ; Middle: φ^2 ; Right: φ^3 .



(a) $t = 2.30 \times 10^{-7}$, $\mathbf{C}_3\nu^1, \varphi^1$ (b) $t = 2.30 \times 10^{-7}$, $\mathbf{C}_3\nu^2, \varphi^2$ (c) $t = 2.30 \times 10^{-7}$, $\mathbf{C}_3\nu^3, \varphi^3$

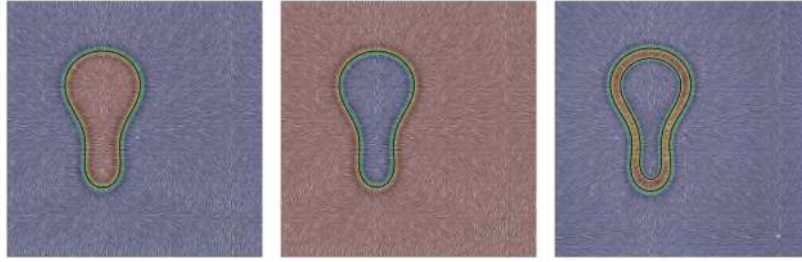


(d) $t = 3.89 \times 10^{-7}$, $\mathbf{C}_3\nu^1, \varphi^1$ (e) $t = 3.89 \times 10^{-7}$, $\mathbf{C}_3\nu^2, \varphi^2$ (f) $t = 3.89 \times 10^{-7}$, $\mathbf{C}_3\nu^3, \varphi^3$

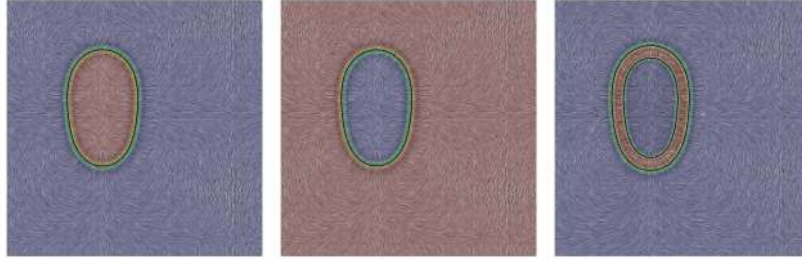


(g) $t = 6.76 \times 10^{-7}$, $\mathbf{C}_3\nu^1, \varphi^1$ (h) $t = 6.76 \times 10^{-7}$, $\mathbf{C}_3\nu^2, \varphi^2$ (i) $t = 6.76 \times 10^{-7}$, $\mathbf{C}_3\nu^3, \varphi^3$

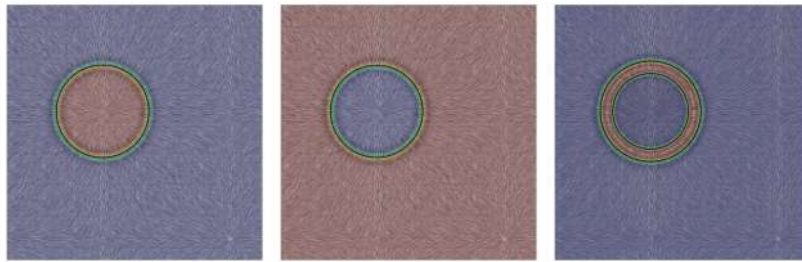
Figure 6.7 Streamlines of the relative configurational traction $\mathbf{C}_\sigma\nu^\alpha$, level curve \mathcal{L}_0^α (black) upon which $\varphi^\alpha = 0$.



(a) $t = 6.77 \times 10^{-6}$, $\mathbf{C}_3 \boldsymbol{\nu}^1, \varphi^1$ (b) $t = 6.77 \times 10^{-6}$, $\mathbf{C}_3 \boldsymbol{\nu}^1, \varphi^2$ (c) $t = 6.77 \times 10^{-6}$, $\mathbf{C}_3 \boldsymbol{\nu}^3, \varphi^3$

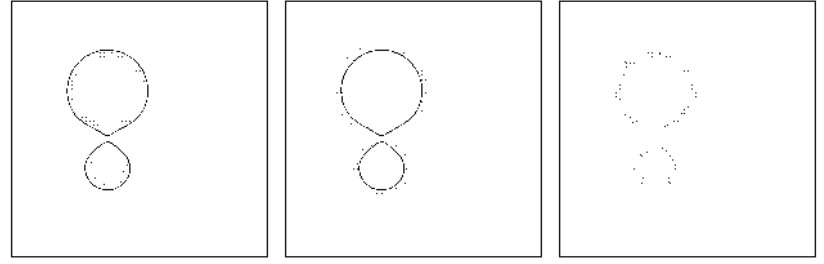


(d) $t = 3.00 \times 10^{-5}$, $\mathbf{C}_3 \boldsymbol{\nu}^1, \varphi^1$ (e) $t = 3.00 \times 10^{-5}$, $\mathbf{C}_3 \boldsymbol{\nu}^2, \varphi^2$ (f) $t = 3.00 \times 10^{-5}$, $\mathbf{C}_3 \boldsymbol{\nu}^3, \varphi^3$

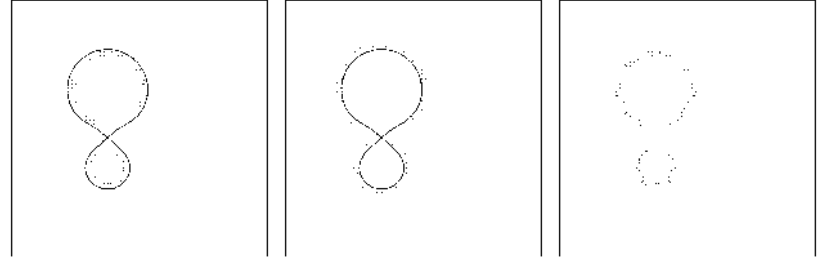


(g) $t = 5.70 \times 10^{-3}$, $\mathbf{C}_3 \boldsymbol{\nu}^1, \varphi^1$ (h) $t = 5.70 \times 10^{-3}$, $\mathbf{C}_3 \boldsymbol{\nu}^2, \varphi^2$ (i) $t = 5.70 \times 10^{-3}$, $\mathbf{C}_3 \boldsymbol{\nu}^3, \varphi^3$

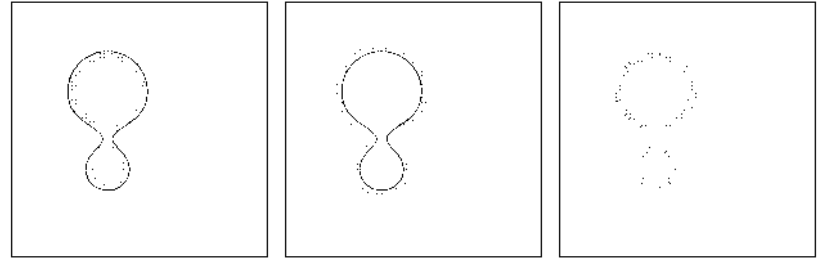
Figure 6.8 Streamlines of the relative configurational traction $\mathbf{C}_\sigma \boldsymbol{\nu}^\alpha$, level curve \mathcal{L}_0^α (black) upon which $\varphi^\alpha = 0$.



(a) $t = 2.30 \times 10^{-7}$, $\mathbf{C}_3\nu^1, \varphi^1$ (b) $t = 2.30 \times 10^{-7}$, $\mathbf{C}_3\nu^2, \varphi^2$ (c) $t = 2.30 \times 10^{-7}$, $\mathbf{C}_3\nu^3, \varphi^3$



(d) $t = 3.89 \times 10^{-7}$, $\mathbf{C}_3\nu^1, \varphi^1$ (e) $t = 3.89 \times 10^{-7}$, $\mathbf{C}_3\nu^2, \varphi^2$ (f) $t = 3.89 \times 10^{-7}$, $\mathbf{C}_3\nu^3, \varphi^3$



(g) $t = 6.76 \times 10^{-7}$, $\mathbf{C}_3\nu^1, \varphi^1$ (h) $t = 6.76 \times 10^{-7}$, $\mathbf{C}_3\nu^2, \varphi^2$ (i) $t = 6.76 \times 10^{-7}$, $\mathbf{C}_3\nu^3, \varphi^3$

Figure 6.9 Streamlines of the relative configurational traction $\mathbf{C}_\sigma\nu^\alpha$, level curve \mathcal{L}_0^α (black) upon which $\varphi^\alpha = 0$.

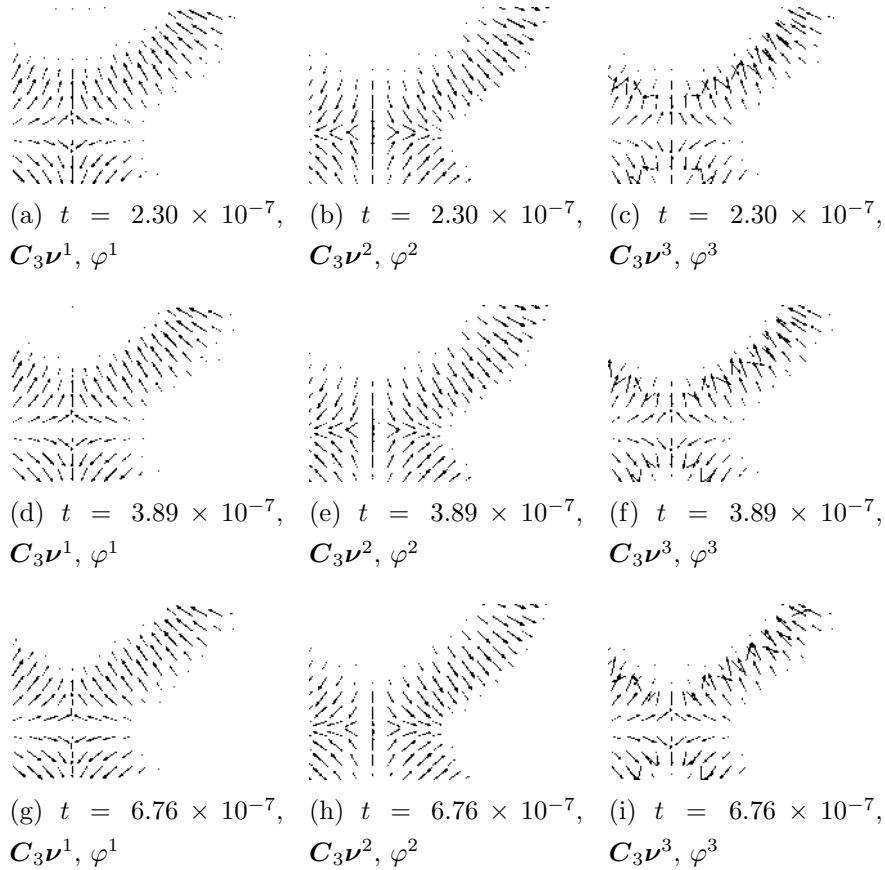


Figure 6.10 Streamlines of the relative configurational traction $C_\sigma\nu^\alpha$, level curve \mathcal{L}_0^α (black) upon which $\varphi^\alpha = 0$.

6.3 The inhomogeneous thermodynamic pressure in solid solutions

In discussing systems undergoing volume changes, Truesdell §5C [117]—in the appendix *A Theory of Multiphase Mixtures* by Passman, Nunziato & Walsh—identified the thermodynamical pressure as the conjugate power expenditure to this thermo-kinematic process, that is, change of volume versus thermodynamic pressure. One should bear in mind that the spherical part of the Cauchy tensor only provides the mechanical' contribution which is indeed an essential part of the thermodynamic pressure. Nevertheless, by no means, the spherical part of the Cauchy tensor represents a complete description of the pressure. Thermodynamically speaking, the thermodynamic pressure is defined as the negative variation of the Helmholtz free-energy with respect to the volumetric variations, that is,

$p^{th} = -\partial\Psi/\partial v$. In multicomponent systems, we also identify $p_\alpha = \varphi_\alpha p$ as the pressure related to the α -th species, with a concentration φ_α . At the steady state, this thermodynamic pressure can be spatially inhomogeneous which entails that the system reaches equilibrium under non-hydrostatic stresses [10, 12, 37, 38].

To model the physical and chemical responses that lead to inhomogeneous pressures, we use the thermodynamically-consistent model for the description of the chemo-mechanical interactions of multicomponent solids far from equilibrium described in §3. Inhomogeneous stress generation and therefore spatially inhomogeneous pressure distributions arise from either external loading induced by deformation across the solid boundaries or local volume changes associated with chemical processes. In this section, we model the inhomogeneous pressure distributions that result from local volume changes. We show that nucleation and growth of new phases induce volumetric stresses that lead to spatially inhomogeneous pressure distributions. We use a constitutive relation for the elastic energy that relates the stress-assisted volume changes as well as stresses resulting from mechanical loading. Moreover, we allow for interfacial interactions in the definition of the chemical energy. By doing so, we can describe the Ostwald ripening and Gibbs–Thomson effects which have repeatedly been reported in the geosciences literature as an important feature in the evolution of metamorphic rocks [18–20]. Using our thermodynamically-consistent framework, we model an elastic solid composed of three phases. As the phases diffuse and react, the solid undergoes volumetric stresses which drive the generation of the inhomogeneous pressure distribution. We calculate this pressure as the negative of the variation of the Helmholtz free energy with respect to the specific volume. Herein, we do not model a specific case in geoscience. However, the parameters used in the simulation are in the range of common physical processes in geoscience.

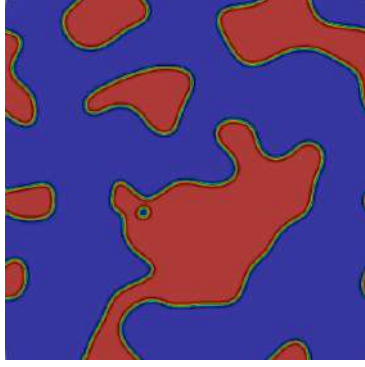


Figure 6.11 represents the spatial distribution of the initial concentrations for both $\hat{\varphi}^1$ and $\hat{\varphi}^2$. Regions colored by red and blue represent the species $\hat{\varphi}^1$ and $\hat{\varphi}^2$, respectively. As the chemical and mechanical processes evolve, the system favours generating a new species $\hat{\varphi}^3$ which contributes to the volumetric stress formation in the solid as it nucleates and grows.

We treat the system as a general multicomponent solid whose crystalline structure imposes a mass constraint such that the relation (4.5) holds. One of the phases emerges from a forward chemical reaction. The chemical reaction occurs in solid state, and as it proceeds, the new phase grows and nucleates. As mentioned in chapter §3.3, we do not take into account neither diffusion by vacancies nor grain boundaries between the phases. In other words, the crystalline structure of each phase, described by a lattice such as Figure 3.3, is coherent. We portrait the scenario where local volume changes caused by chemical interactions trigger the stress generation in the solid which in turn reflects spatial variations in pressure. This physical quantity corresponds to the thermodynamic pressure described in chapter §3.6. We use the diffusion coefficients, the reaction rates, and the thermodynamic properties of commonly found in solid solutions. Table 6.2 condenses such quantities. The overall reaction is given by $\hat{\varphi}^1 + \hat{\varphi}^2 \xrightarrow{k_+} \hat{\varphi}^3$.

Moreover, φ_1 , φ_2 , and φ_3 define the concentration of the phases $\hat{\varphi}^1$, $\hat{\varphi}^2$, and $\hat{\varphi}^3$, respectively. Figure 6.11 depicts the spatial distribution of the initial concentration for the phases A and B, respectively. We assume the initial concentration of $\hat{\varphi}^3$ to be zero. We also assume a solid without distortions at $t = 0.0$. This implies zero relative displacements in the sample and thus, zero strains. We choose a spatial distribution of the concentrations, as Figure 6.11 shows, to account for large concentration gradients so we can see the effect of the interface evolution [32]. Namely, the contribution of the curvature in the chemical potential. We are interested in observing the effect of local variations in the concentration upon

the generation of inhomogeneous stress and pressure distribution which translates into the impact of the concentration species on the deformation gradient captured by a volumetric stress tensor. Hence, the whole source of stress generation comes from the volumetric deformation since we do not impose external loading nor deformation. Furthermore, there are no species fluxes through the boundaries. Following [33], deformation itself cannot induce mass transport. Therefore, for mass transport to happen, there must be chemical potential gradients where the chemo-mechanical coupling accounts for the contributions from both the physical and chemical responses of the solid-species system which in the material sciences literature is known as the absence of a piezo-diffusive effect. We set the chemical energy parameter as well as the number of molecules per volume so that we guarantee a non-convex triple-well energy functional. For instance, Figure 3.6 models the two phases case. Phase separation processes are not common in metamorphic evolution. Therefore, one can set the chemical energy such that no phase separation emerging from interfacial interactions occur.

Table 6.2: Chemical and physical parameters to calculate the thermodynamic pressure

Physical parameter	Value	Name
ϑ [K]	1373.15	Temperature
ϑ^c [K]	1500.0	Critical temperature
D [m ² s ⁻¹]	10 ⁻²⁰	Diffusion coefficient
k_+ [m ² s ⁻¹]	10 ⁻¹⁴	Reaction rate
σ [J m ⁻²]	0.817	Interfacial energy
ℓ [m]	10 ⁻⁸	Interface thickness
G [GPa]	44	Shear modulus
β [-]	0.17	Poisson's ratio
ω [-]	10 ⁻²	Swelling parameter

Figures 6.12-6.15 show the temporal evolution of the concentration of the phases $\hat{\varphi}^1$, $\hat{\varphi}^2$, and $\hat{\varphi}^3$ together with the spatial distribution of the thermodynamic pressure, p^{th} , as the solid-three species system goes to equilibrium, respectively. Unlike the thermodynamic pressure, the concentrations and time evolution are presented as dimensionless quantities. As discussed above, we calculate the concentration of the species $\hat{\varphi}^3$, φ_3 , by applying at each time-step the constraint defined by 3.1, which guarantees the consistency of the process. At early stages $t < 5.6 \times 10^{-4}$, Figure 6.12, the non-Fickian diffusion essentially controls the tem-

poral evolution of both the physical and mechanical processes as the forward chemical reaction plays no substantial role. One can verify such assertion by checking the species mass evolution in Figure 6.16, where during $t < 2.63 \times 10^{-3}$ the species masses remain approximately constant. Moreover, from Figure 6.12, one can also infer that there is no formation of the species $\dot{\varphi}^3$ until $t > 5.6 \times 10^{-4}$. Therefore, the initial condition, spatially distributed as Figure 6.11, goes through phase separation during the early stages and is followed by coarsening [45]. These interactions lead to a merging process which eventually forms large and rounded structures as suggested by Figures 6.12 and 6.13. Hence, we conclude that at the early stages the source of stress generation is entirely characterised by variations in local composition caused by diffusion and therefore, the dynamics of the spatially inhomogeneous pressure distribution results solely from both the phase separation and coarsening mechanisms while the system tries to minimise its free energy by reducing the interface between the species $\dot{\varphi}^1$, $\dot{\varphi}^2$ and $\dot{\varphi}^3$. Figure 6.16 also depicts the temporal evolution of the interfacial energy which verifies that during $t < 2.63 \times 10^{-3}$, in particular for the species $\dot{\varphi}^1$ and $\dot{\varphi}^2$, the interfacial energy decreases. Furthermore, the stress-assisted volume change mechanism primarily occurs along the boundary between $\dot{\varphi}^1$ and $\dot{\varphi}^2$ as the system forms the rounded structures. Namely, large stresses arise along the interface between $\dot{\varphi}^1$ and $\dot{\varphi}^2$. Figure 6.18 reports the dynamics of the neo-Hookean energy functional which captures the shrinkage and swelling process as the phases diffuse through the solid structure. From the free energy evolution, Figure 6.17, shows that the system is minimising its free energy as the diffusion dissipative process occurs. The latter is a direct consequence of the principle of minimum energy which states the internal energy is minimised as the system reaches constant entropy. The free energy functional describes the contribution from both the physical and chemical responses of the solid. As discussed in Section 3.5, the model captures the dynamics of the Ostwald ripening [18–20]. In the range between $1.73 \times 10^{-3} < t < 2.63 \times 10^{-3}$, Figure 6.13 illustrates that the smaller aggregates of phase $\dot{\varphi}^1$ tend to dissolve into the solid solution and precipitate along the surface of the larger aggregates. Such mechanism leads to a large rounded structure of the species $\dot{\varphi}^1$ which is entirely enclosed by the species $\dot{\varphi}^2$. Figure 6.13 also shows the heterogeneous distribution of the thermodynamic pressure. The thickness of the reaction layer between the phases $\dot{\varphi}^1$ and $\dot{\varphi}^2$ is irregular, see Figure 6.13 (c)-(d). Conventionally, during reaction-diffusion processes, one can expect a planar growth of the reaction layer. Nevertheless, when considering reaction-induced stresses and interfacial contributions, the chemical potential becomes also a function of both

the surface curvature and the mechanical pressure which leads to an irregular reaction layer of thickness. As a result, the driving force of the diffusion process changes along the reaction layer which induces different diffusion rates at the reaction boundary. The forward chemical reaction occurs mainly the time interval between $8.02 \times 10^{-3} < t < 3.91 \times 10^{-2}$, see Figure 6.14. Milke et al. [2] define that positive volume changes involve the creation of space by moving out mass from the reaction site, and thus, the reaction products can grow and accommodate. On the contrary, negative volume changes induce mass transport into the reaction site by consuming the reactant phases. During this stage, the system forms the species ϕ^3 along the boundary between the species ϕ^1 and ϕ^2 .

Milke et al. [118] provides experimental evidence that the system forstatite (fo) - quartz (qtz) - enstatite (en) produces a reaction rim, mainly composed of enstatite (en), of irregular thickness. They suggest that the nature of this behaviour is due to the mechanical contributions to the chemical potentials resulting from the local volume changes caused by the chemical reaction. Although the mechanical contributions are important since they influence the chemical potentials, one must also consider the contributions of surface curvature between the phases as they also alter to a large degree the chemical potentials. This curvature effect is called the Gibbs-Thomson effect [119–121]. The mechanism of rim growth as defined by metamorphic petrologists results from the chemical reaction between neighboring minerals [2, 122]. In particular, such a process, which is strongly related to the mechanical properties of the solid, involves large volume changes that lead to large volumetric stresses.

Eventually, the volumetric stress drives the spatial variations in pressure. Moreover, one can verify from Figure 6.16 that in the range between $8.02 \times 10^{-3} < t < 3.91 \times 10^{-2}$ the species masses change as well as the interfacial energy. Consequently, the masses of the reactant species ϕ^1 and ϕ^2 tend to decrease while the reaction product, in this case the species ϕ^3 , increases. At the end of such stage, the system completely consumes the mass of the species ϕ^1 and as expected the interfacial energy of the species ϕ^3 increases as the forward reaction generates more species ϕ^3 and therefore grows interface. Following [45], the reaction term in the chemical process increases the free energy of the system resulting in the growth tend depicted by Figure 6.17 in the time interval between $8.02 \times 10^{-3} < t < 3.91 \times 10^{-2}$. Finally, the interleaving between the chemical and mechanical responses of the solid form an elongated structure along the solid primarily composed of the species ϕ^2 and surrounded by the species ϕ^3 . Due the large

volume changes associated with the chemical process, we can see the stresses all along the solid and thereby the notorious inhomogeneous pressure distribution at the steady state. Figure 6.17 shows that from $t > 7.99 \times 10^{-2}$ all dissipative processes ceased as the free energy remains constant. This final pressure defines the equilibrium condition of the system and results from the interleaving between the physical and chemical responses of the solid. The red dots shows in Figure 6.17 represent the beginning of the processes mentioned above. In particular, one and two account for the beginning of the phase separation and coarsing processes, respectively. Analogously, between three and four the system undergoes the Ostwald ripening effect. Finally, five and six define the action of the forward chemical reaction and the equilibrium state of the solid-species system, respectively.

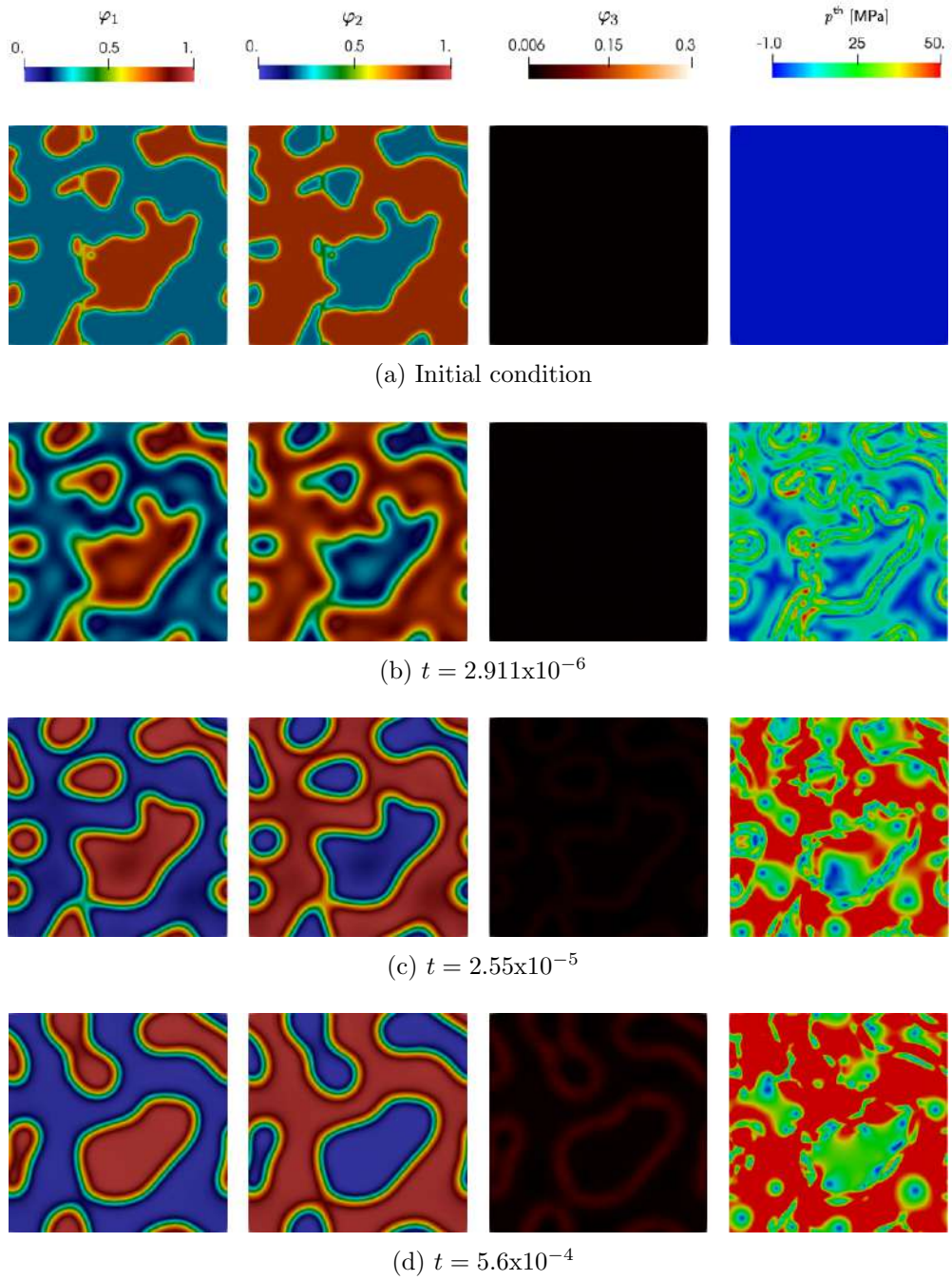


Figure 6.12 depicts the behaviour of the three phases system at the early stages. According to the evolution, the system is mostly controlled by the interleaving of phase separation and coarsening. Therefore, the volume changes and subsequent stress generation result from the diffusion process itself leading to the inhomogeneous pressure distribution

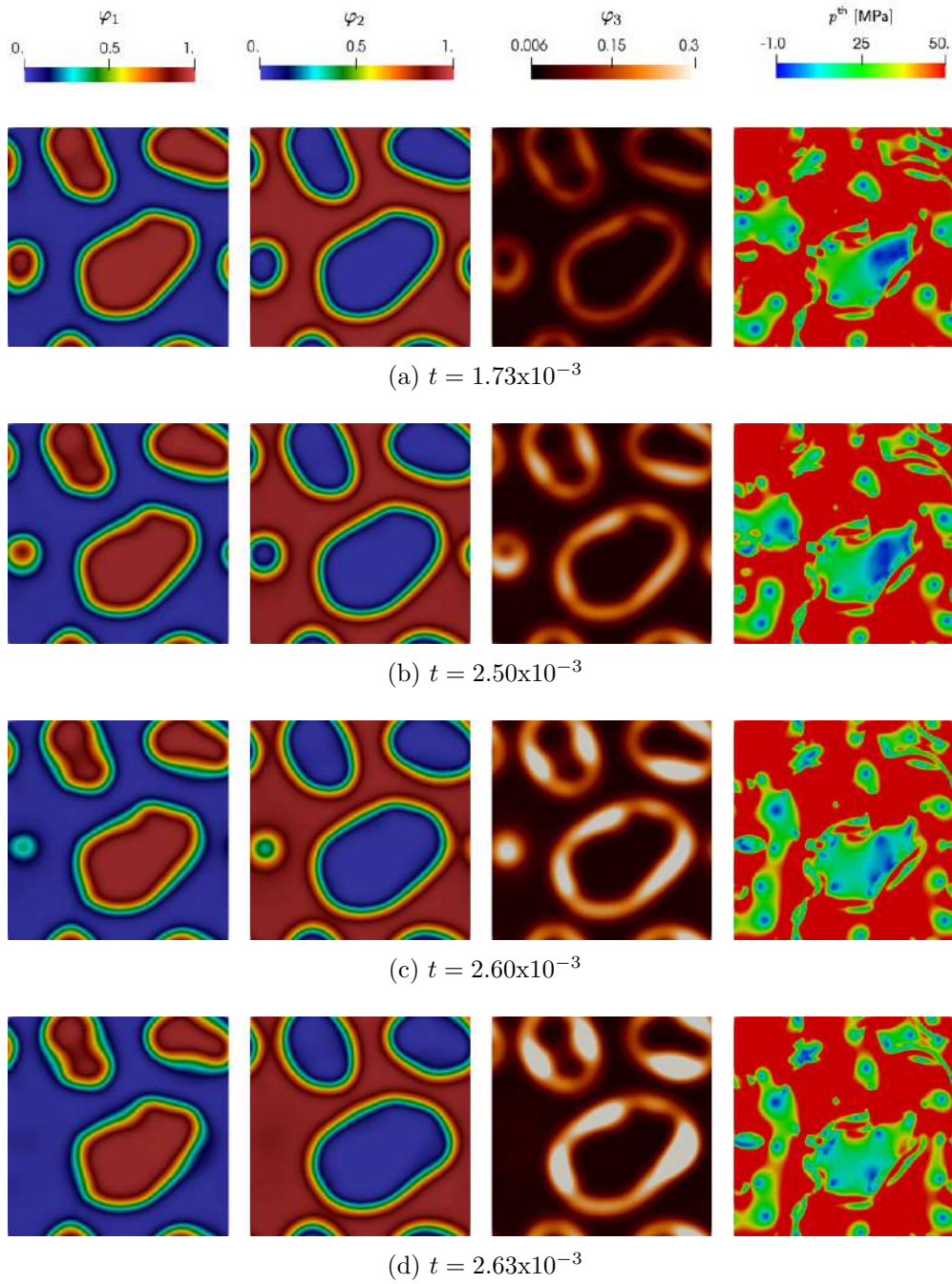


Figure 6.13 portrays the dynamics of the system as it follows the Ostwald ripening effect. The unstable particles on the surface dissolve and go into the solution, and once the solution gets supersaturated, these particles tend to precipitate onto the surface of the more stable structures. Consequently, the larger structure in the system grows.

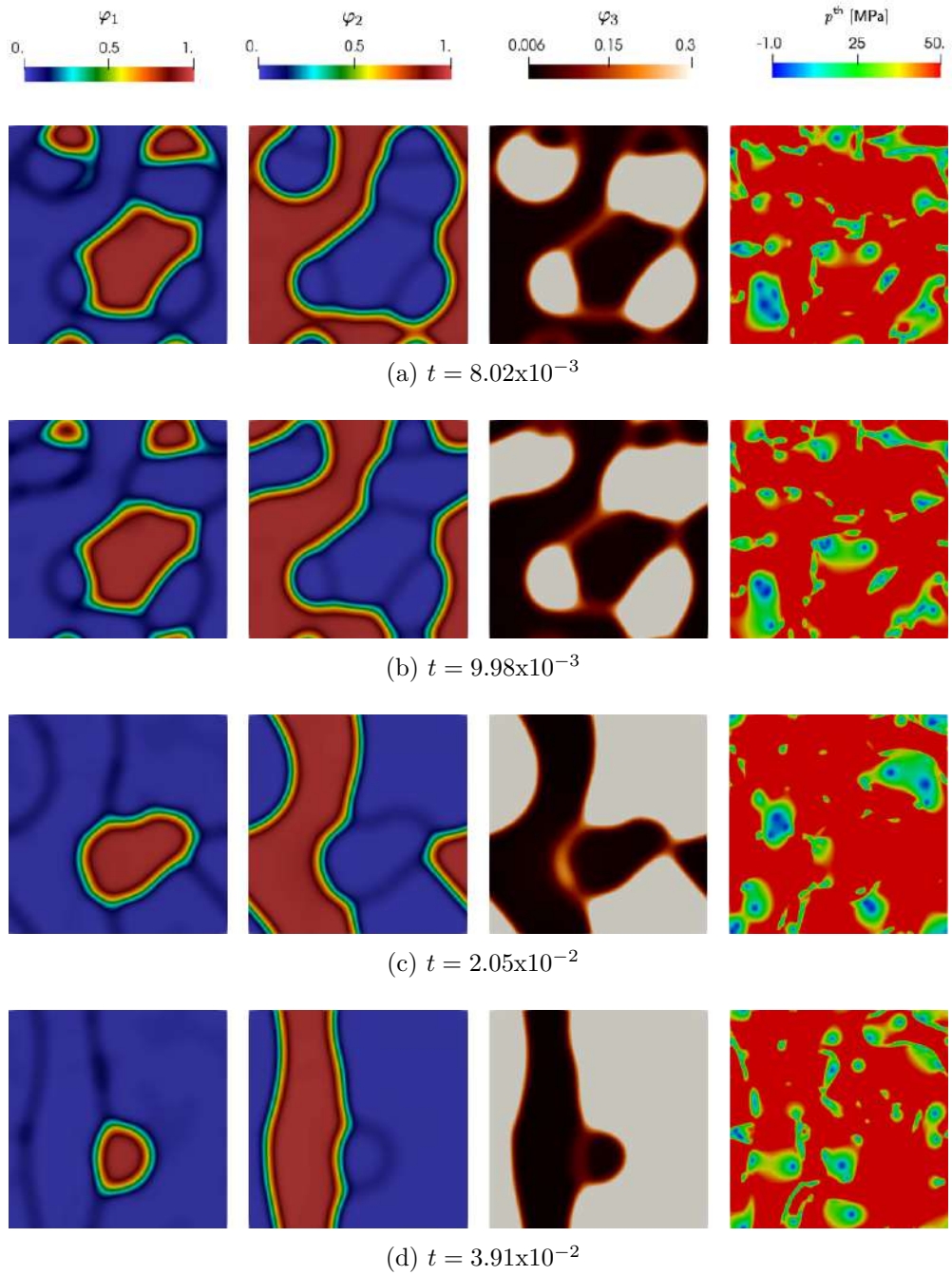


Figure 6.14 shows the reaction between the species φ^1 and φ^2 to produce a new phase C along their boundary. The evolution favours to consume in a greater proportion the phase φ^1 than the phase φ^2 . The simulation results show how the nucleation and growth of phases induce volumetric stresses which in turn contribute to generate the inhomogeneous pressure distribution.

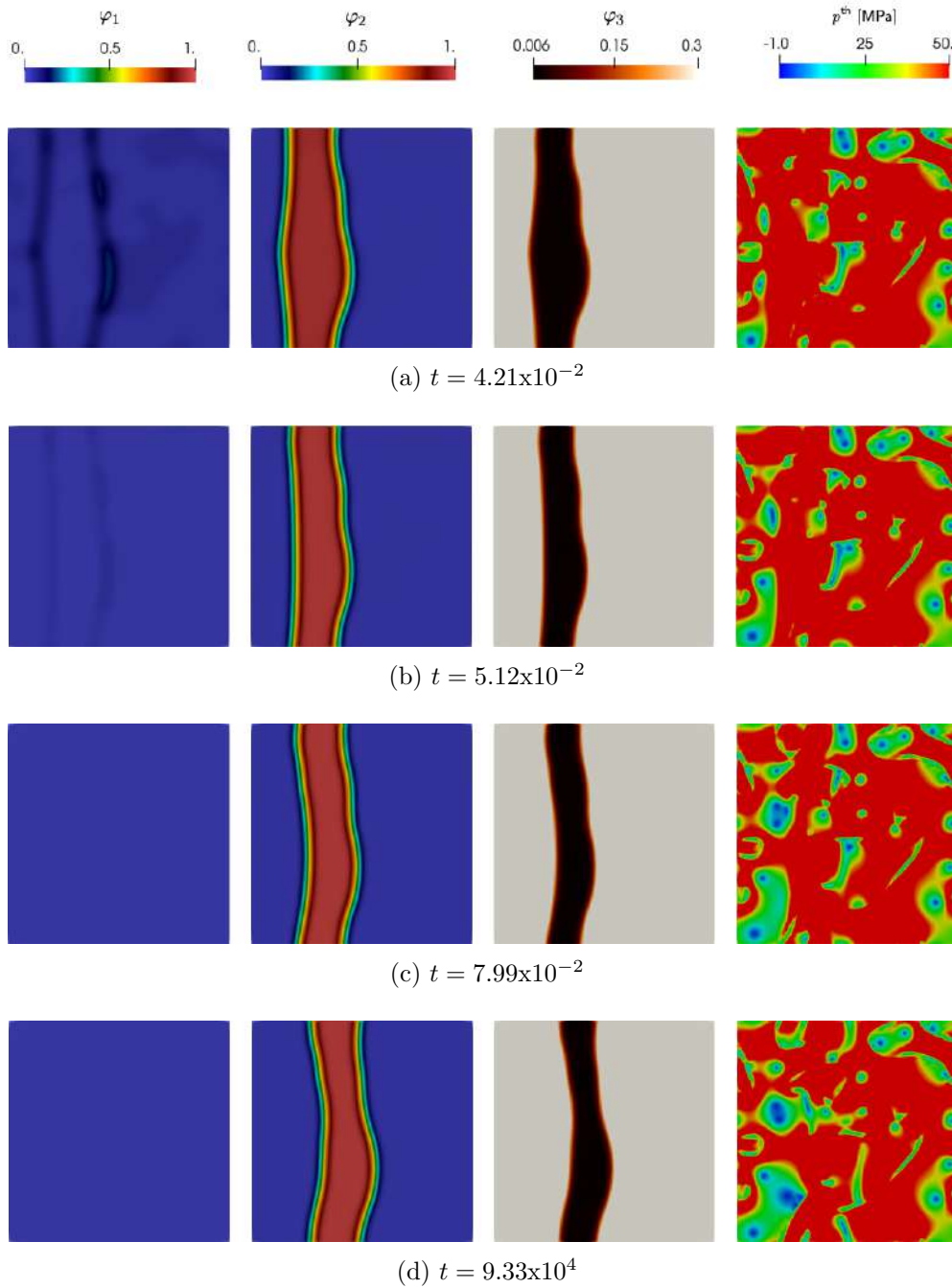


Figure 6.15 suggests that the chemical reaction acts as either a source or sink of energy. In this particular case, it contributes to increasing the free energy of the system. Once the chemical process ceases, the system minimizes its free energy solely by mass transport leading to the steady state at $t > 9.33 \times 10^4$. Finally, the thermodynamic pressure at $t > 9.33 \times 10^4$, which results from the contribution of both chemical and mechanical responses of the solid, defines the equilibrium of the metamorphic system.

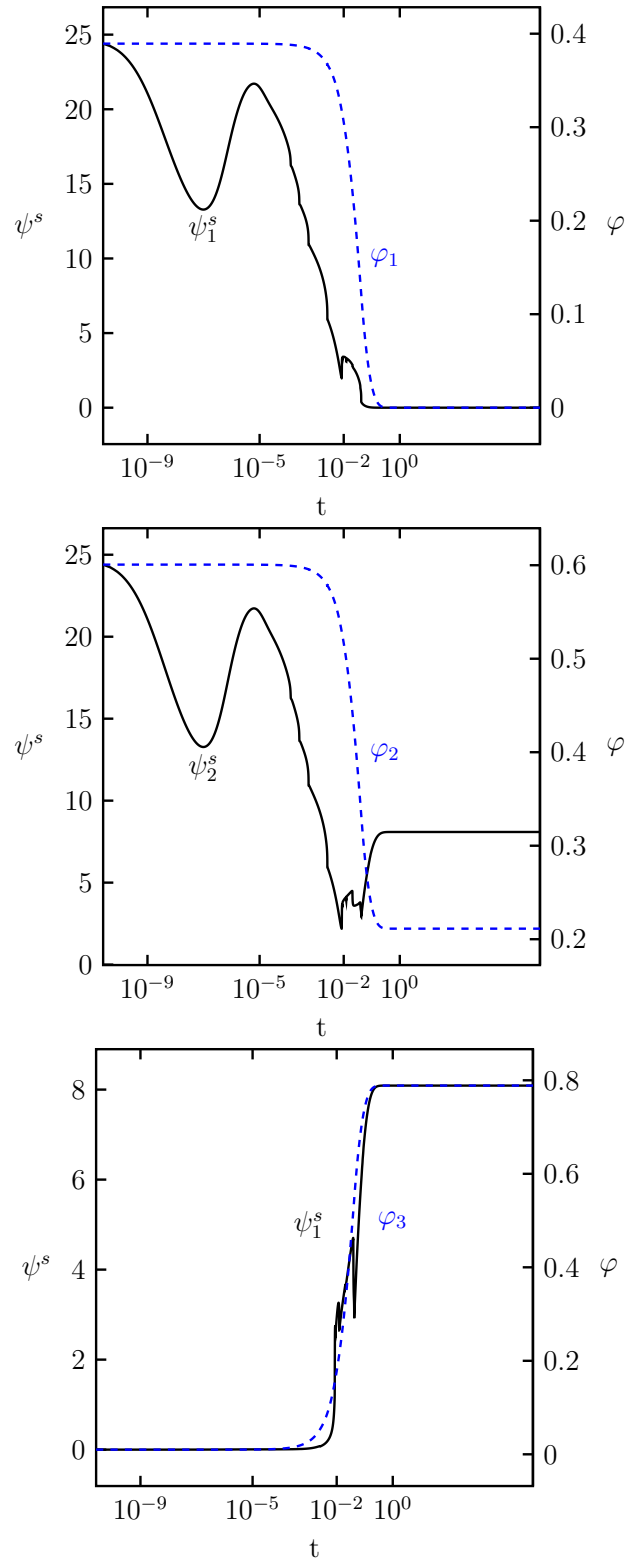


Figure 6.16 depicts that when a system undergoes a chemical process, either mass transport or chemical reaction, the dynamics favours to either produce or destroy the interface between the species. Thus, the interfacial energy must change according to this evolution process.

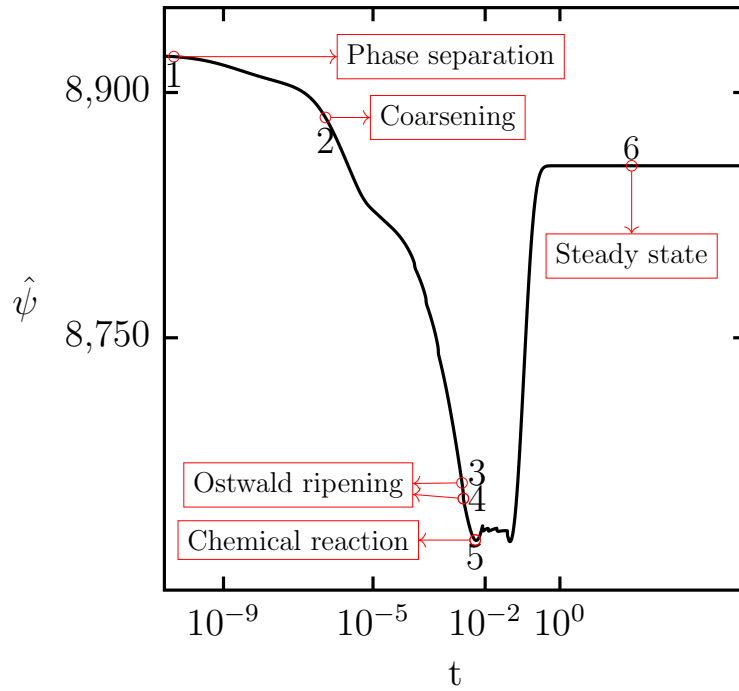


Figure 6.17 shows the free energy evolution and marks the beginning of processes such as phase separation and coarsening, Ostwald ripening effect, the chemical reaction and steady state.

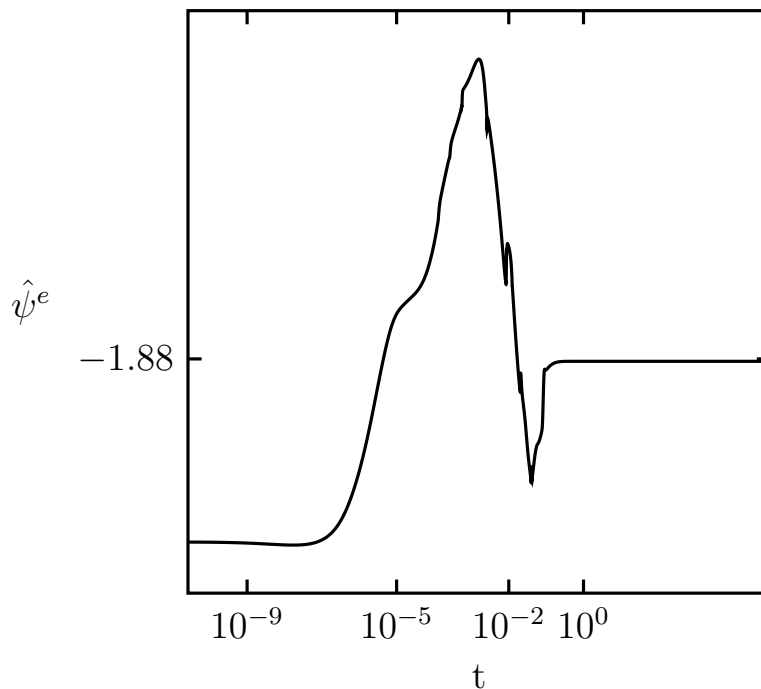


Figure 6.18 depicts the elastic energy of a neo-Hookean solid model. Since no deformation is induced across the solid boundaries, the variation of the elastic energy entirely results from the volumetric stresses associated with the variations in local composition.

The possibility of describing the formation of metamorphic mineral aggregates with spatial inhomogeneous pressure distributions collides with the classical description of the formation of metamorphic minerals. The classical interpretations assume an isotropic thermodynamic equilibrium to explain metamorphic mineral assemblages via thermobarometry techniques and phase diagrams. Therefore, the formation processes that induce heterogeneous pressure distributions imply that these techniques may not be robust to characterize metamorphic systems. That is, these inhomogeneous pressure conditions contradict the foundational assumptions of uniform pressure and temperature distributions. Thus, the nature of the pressure distribution that defines the equilibrium of metamorphic rocks and especially how to calculate and define this quantity are still open questions in our opinion. As pointed out by Hobbs and Ord [3] (and references therein), the thermodynamic equilibrium is entirely characterized by the thermodynamic pressure given by the partial derivative of the Helmholtz free energy with respect to the specific volume or when considering Gibbs free energy, the partial derivative has to be taken with respect to the volume. We believe that heretofore, in the geosciences literature, the lithostatic pressure has erroneously been used to describe the state of equilibrium of the metamorphic rocks. And recently, works on inhomogeneous pressure distributions use the mean stress to characterize equilibrium conditions [1, 13]. Such pressure definitions only make sense from a thermodynamic point of view when the solid behaves elastically without ongoing chemical processes [3]. Solids under either viscoelastic, diffusional creep, or plastic behavior as well as ongoing chemical reactions between the constituent phases relate dissipative processes which lead to additional contributions to the definition of thermodynamic pressure [3]. Hobbs and Ord have carried out an extensive review on the subject [3, 14] (see also e.g [15] and references therein).

To conclude, using a chemo-mechanical model for solid solutions, we study how the mechanical response affects on the evolution of a chemically active solid-three species solution. We demonstrate that the interleaving between the chemical and mechanical responses of the multicomponent solid influences the generation of spatial variations in pressure. This pressure corresponds to the thermodynamic pressure and defines the equilibrium conditions of the system. By setting the corresponding physical and mechanical properties, one can model the chemo-mechanical behaviour of a multicomponent solid which follows interfacial effects as well as large stresses. Moreover, this framework can help as a first step to model the behaviour of the stress-generation processes in metamorphic minerals which

lead to spatial distribution of the thermodynamic pressure. Nevertheless, one must bear in mind that, phase separation mechanisms are not common processes in metamorphic systems. Therefore, to model these metamorphic systems using the aforementioned framework, the chemical energy must be set such that no phase separation takes place along the process. This can be achieved by choosing the initial distribution of the phases concentration at the minimum values of the chemical energy. Thereby, the system does not tend to minimise the energy by separating the phases.

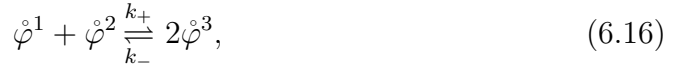
6.4 Coupled chemo-mechanical responses of solid solutions

In this section, we carry out 2D and 3D numerical simulations of a solid solution composed of three phases φ^1 , φ^2 , and φ^3 to investigate their coupled chemo-mechanical interactions. In particular, the 2D simulation shows how interfacial interactions together with a reversible chemical reaction between the phases engender volumetric stresses as a result of local volume changes. The 3D simulation, on the other hand, studies a pure ripening mechanism. The interfacial interactions between the phases drive the phase separation process and allow for the Ostwald ripening and Gibbs-Thomson effects. We show the temporal evolution of the dimensionless phases concentrations as well as the dimensionless displacements in both x and y directions.

Our motivation to carry out simulations in both phase separation and interfacial interactions coupled with deformation relies on the evidence of the spinodal decomposition patterns in crystals of K-rich feldspar. Moreover, the uphill diffusion of chemical components caused by exsolution processes favours spinodal decomposition and deformation. These processes are associated with the temperature gradient in the crust and shear zones and overburden, respectively. Hence, this spontaneous phase separation process coupled with deformation as a result of changes in temperature controls the evolution of the texture of the metamorphic system since, when considering a deformable medium, the evolution of the phase separation is also a function the local stresses [21].

6.4.1 Reversible chemical reaction of random distributed phases

The reversible chemical reaction between the phases is



where the stoichiometry vectors $v^{\alpha\beta}$ and $\varpi^{\alpha\beta}$ are given by

$$v^{\alpha\beta} = (1, 1, 0), \quad \text{and} \quad \varpi^{\alpha\beta} = (0, 0, 2). \quad (6.17)$$

We seek to study the stress-assisted volume changes mechanism triggered by the chemical processes. Therefore, we do not consider deformation induced across the solid boundaries. We set the external body forces and external microforces such that $\mathbf{b} = \mathbf{0}$ and $\gamma^\alpha = 0$, respectively. Moreover, we neglect all inertial effects. Consequently, the spatial velocity is $\mathbf{v} = \mathbf{0}$. The reaction rates and the diffusion coefficients are in the range of common physical process in geoscience. On the other hand, the mechanical properties of the solid are in the range of the mechanical properties for metamorphic minerals such as garnet [123]. We assume that the three phases diffuse at the same rate. Therefore, we only consider one diffusion coefficient. In this simulation example, we set $k_+ > k_-$. Thus, the forward chemical reaction occurs faster than the backwards one. Our initial condition serves as the reference configuration which we choose as an underformed state of the body. The mass supply of each phase, captured by the reaction term s^α , results solely from internal contributions as (6.16) takes place. Therefore, we set $s_{\text{ext}} = 0.0$ in (5.20). The initial spatial distribution of the phases concentrations is random such that φ^α takes values between $\varphi^\alpha \pm 0.05$ where we assume φ^α is $1/n$. We calculate the concentration of $\dot{\varphi}^3$ following the mass constraint given by (5.24). As mentioned before, this mass constraint is applied at each time step to calculate the relative quantities resulting from the Larché–Cahn derivative. By doing so, we guarantee the consistency of the process. Furthermore, there is no mass flux at the solid boundaries.

Figure 6.19 portrays the spatial distribution of the initial phases concentrations in conjunction with the initial displacements. We set the parameters in the chemical energy such that we obtain a triple-well function. This function allows us to model the phase separation process. The initial concentrations for the phases $\dot{\varphi}^1$, $\dot{\varphi}^2$, and $\dot{\varphi}^3$ will tend to reach the concentrations at the well points as the system minimises its global free energy. Table 6.3 summarises the param-

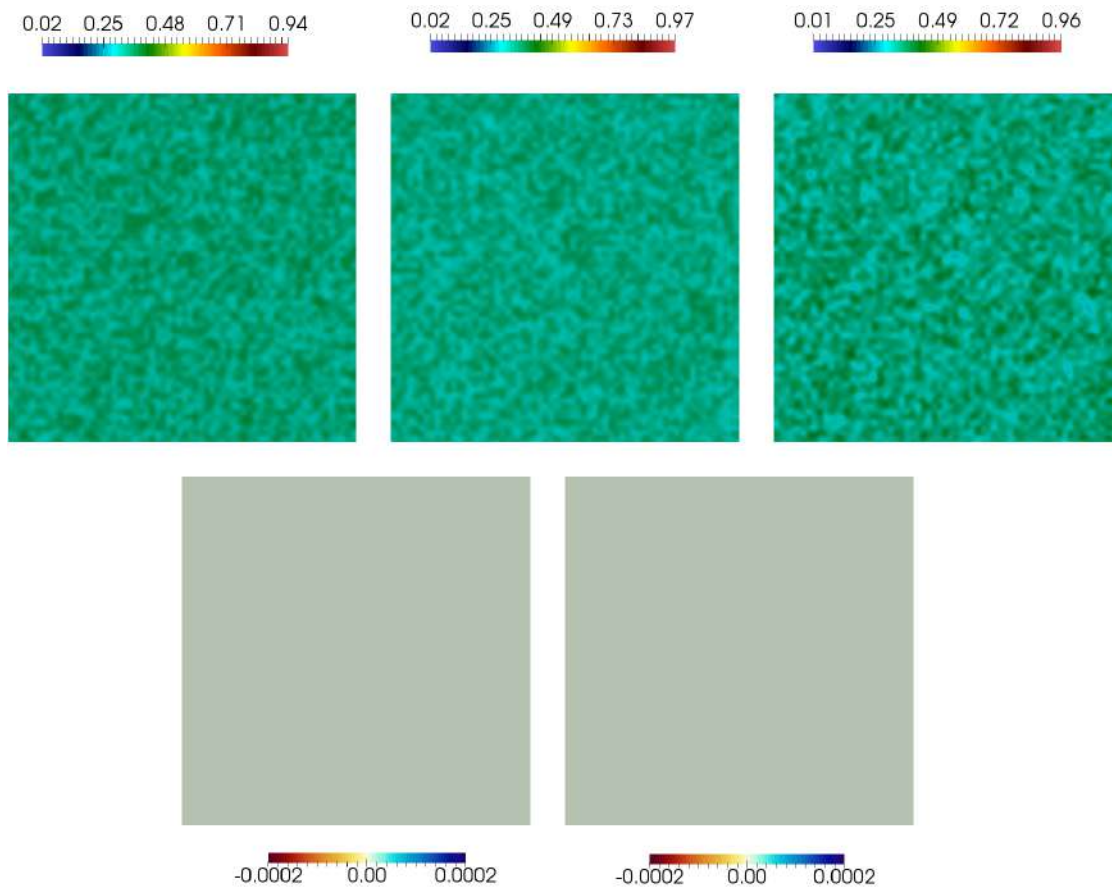


Figure 6.19 represents the spatial distribution of the initial concentrations for $\hat{\varphi}^1$, $\hat{\varphi}^2$, and $\hat{\varphi}^3$ together with the initial displacements. Top left: $\hat{\varphi}^1$; Top middle: $\hat{\varphi}^2$; Top right: $\hat{\varphi}^3$; Bottom left: u_x ; Bottom right: u_y . The phases $\hat{\varphi}^1$ and $\hat{\varphi}^2$ react to form $\hat{\varphi}^3$ which in turn decomposes into $\hat{\varphi}^1$, and $\hat{\varphi}^2$ as a result of the backward chemical reaction. The formation of $\hat{\varphi}^3$ and concomitant decomposition into $\hat{\varphi}^1$ and $\hat{\varphi}^2$ favour to generate volumetric stresses.

Table 6.3: Chemical and physical parameters that control the spinodal decomposition process

Physical parameter	Value	Name
ψ_0 [J m ⁻³]	1×10^5	Energy density
L_0 [m]	10^{-6}	Domain length
u_0 [m]	10^{-6}	Reference displacement
ω^1 [-]	0.0383	Swelling parameter phase 1
ω^2 [-]	0.0334	Swelling parameter phase 2
ω^3 [-]	0.0165	Swelling parameter phase 3
G [GPa]	40	Shear modulus
β [-]	0.17	Poisson's ratio
ϑ [K]	727.0	Absolute temperature
ϑ_c^{12} [K]	800.0	Critical temperature between phases 1 and 2
ϑ_c^{13} [K]	800.0	Critical temperature between phases 1 and 3
ϑ_c^{23} [K]	800.0	Critical temperature between phases 2 and 3
D [m ² s ⁻¹]	10^{-20}	Diffusion coefficient (same for all phases)
k_+ [m ² s ⁻¹]	10^{-14}	Forward reaction rate
k_- [m ² s ⁻¹]	10^{-16}	Backward reaction rate
σ [J m ⁻²]	0.817	Interfacial energy
ℓ [m]	10^{-8}	Interface thickness
γ [-]	0	External microforce (same for all phases)
\mathbf{b} [ms ⁻²]	$\mathbf{0}$	Body force

eters used to build up the dimensionless numbers as outlined in (5.77). Hence, the dimensionless numbers are given by

$$\begin{aligned}
 \bar{D}^{\alpha\beta} &= 1 \times 10^4 \begin{bmatrix} 1 & 1 & 1 \\ 1 & 1 & 1 \\ 1 & 1 & 1 \end{bmatrix}, \quad \bar{\vartheta}_c^{\alpha\beta} = \begin{bmatrix} 0 & 1.100 & 1.100 \\ 1.100 & 0 & 1.100 \\ 1.100 & 1.100 & 0 \end{bmatrix}, \\
 \bar{\sigma}^{\alpha\beta} \bar{\ell}^{\alpha\beta} &= 10^{-2} \begin{bmatrix} 8.17 & 0 & 0 \\ 0 & 8.17 & 0 \\ 0 & 0 & 8.17 \end{bmatrix}, \quad v^{\alpha\beta} = \begin{bmatrix} 1 & 1 & 0 \end{bmatrix}, \\
 \varpi^{\alpha\beta} &= \begin{bmatrix} 0 & 0 & 2 \end{bmatrix}, \quad \bar{k}_+ = 0.01, \quad \bar{k}_- = 0.0001, \quad \bar{G} = 4 \times 10^5
 \end{aligned} \tag{6.18}$$

where we choose $D_0 = D$ and $\ell_0 = \ell$ as the reference diffusion coefficient and interface thickness of a reference phase, respectively.

The final system of coupled chemo-mechanical equations are given by

$$\dot{\varphi}^1 = -k_+ \varphi^1 \varphi^2 + k_- (\varphi^3)^2 - \text{Div} \mathbf{J}_{\mathbf{R}3}^1, \quad (6.19a)$$

$$\dot{\varphi}^2 = -k_+ \varphi^1 \varphi^2 + k_- (\varphi^3)^2 - \text{Div} \mathbf{J}_{\mathbf{R}3}^2, \quad (6.19b)$$

$$\text{Div} \mathbf{T}_R = \mathbf{0}. \quad (6.19c)$$

In (6.19), we use the Larché–Cahn derivative with $\dot{\varphi}^3$ as the reference phase. We solve the system of partial differential equation in its primal form (6.20) and (6.21). We state the problem as follows: find $\{\varphi, \mathbf{u}\} \in \mathcal{C}^2(\mathbf{P})$ such that (5.80) given (5.73) subject to periodic boundary conditions up to the second derivative of φ , and \mathbf{u} with respect to \mathbf{X} in a square open region $\mathbf{P} = (0, 1) \times (0, 1)$. We use the PetIGA [116] isogeometric analysis framework. We use 64×64 element mesh of a polynomial degree 2 and continuity 1.

We denote H^2 as the Sobolev space of square integrable functions with square integrable first and second derivatives and $(\cdot, \cdot)_{\mathbf{P}}$ as the L^2 inner product over the physical domain \mathbf{P} with boundary \mathbf{S} . We multiply the Lagrangian version of the phases mass balance (5.21) by a test function ϱ^α , which belongs to H^2 , using the definition for the material mass fluxes (5.70) and integrating by parts, the primal variational formulation can then be given by:

$$\begin{aligned} (\varrho^\alpha, \dot{\varphi}^\alpha)_{\mathbf{P}} &= (\varrho^\alpha, s^\alpha)_{\mathbf{P}} - (\varrho^\alpha, \mathbf{J}_{\mathbf{R}\sigma I, I}^\alpha)_{\mathbf{P}} \\ &= (\varrho^\alpha, s^\alpha)_{\mathbf{P}} + (\varrho^\alpha, \mathbf{J}_{\mathbf{R}\sigma I}^\alpha)_{\mathbf{P}} - (\varrho^\alpha, \mathbf{J}_{\mathbf{R}\sigma I}^\alpha \mathbf{N}_I)_{\mathbf{S}} \\ &= (\varrho^\alpha, s^\alpha)_{\mathbf{P}} + (\varrho^\alpha, -\mathbf{M}^{\alpha\beta} (\mu_\varphi^\beta + \mu_s^\beta + p_\varphi^\beta),_{,J} \mathbf{C}_{JI}^{-1} J)_{\mathbf{P}} \\ &\quad - (\varrho^\alpha, -\mathbf{M}^{\alpha\beta} (\mu_{,J}^\beta) \mathbf{C}_{JI}^{-1} J \mathbf{N}_I)_{\mathbf{S}} \\ &= (\varrho^\alpha, s^\alpha)_{\mathbf{P}} - (\varrho^\alpha, \mathbf{M}^{\alpha\beta} \mu_{\varphi, J}^\beta \mathbf{C}_{JI}^{-1} J)_{\mathbf{P}} - (\varrho^\alpha, (\mathbf{M}^{\alpha\beta} \mu_s^\beta),_{,J} \mathbf{C}_{JI}^{-1} J)_{\mathbf{P}} \\ &\quad + (\varrho^\alpha, (\mathbf{M}^{\alpha\beta})_{,J} \mu_s^\beta \mathbf{C}_{JI}^{-1} J)_{\mathbf{P}} - (\varrho^\alpha, \mathbf{M}^{\alpha\beta} p_{\varphi, J}^\beta \mathbf{C}_{JI}^{-1} J)_{\mathbf{P}} \\ &\quad + (\varrho^\alpha, \mathbf{M}^{\alpha\beta} (\mu_{,J}^\beta) \mathbf{C}_{JI}^{-1} J \mathbf{N}_I)_{\mathbf{S}} \\ &= (\varrho^\alpha, s^\alpha)_{\mathbf{P}} - (\varrho^\alpha, \mathbf{M}^{\alpha\beta} \mu_{\varphi, J}^\beta \mathbf{C}_{JI}^{-1} J)_{\mathbf{P}} + (\varrho^\alpha, \mathbf{C}_{JI}^{-1} J, \mathbf{M}^{\alpha\beta} \mu_s^\beta)_{\mathbf{P}} \\ &\quad + (\varrho^\alpha, (\mathbf{C}_{JI}^{-1} J),_{,J}, \mathbf{M}^{\alpha\beta} \mu_s^\beta)_{\mathbf{P}} + (\varrho^\alpha, (\mathbf{M}^{\alpha\beta})_{,J} \mu_s^\beta \mathbf{C}_{JI}^{-1} J)_{\mathbf{P}} \\ &\quad - (\varrho^\alpha, \mathbf{M}^{\alpha\beta} p_{\varphi, J}^\beta \mathbf{C}_{JI}^{-1} J)_{\mathbf{P}} + (\varrho^\alpha, \mathbf{M}^{\alpha\beta} (\mu_{,J}^\beta) \mathbf{N}_I \mathbf{C}_{JI}^{-1} J)_{\mathbf{S}} \\ &\quad - (\varrho^\alpha, \mathbf{N}_J \mathbf{C}_{JI}^{-1} J, \mathbf{M}^{\alpha\beta} \mu_s^\beta)_{\mathbf{S}} \end{aligned} \quad (6.20)$$

Furthermore, the weak formulation of the Lagrangian version of the linear momenta balance reads

$$(w_i, \mathbf{T}_{\mathbf{R}iI} \mathbf{N}_I)_{\mathbf{S}} - (w_{i,I}, \mathbf{T}_{\mathbf{R}iI})_{\mathbf{P}} = 0, \quad (6.21)$$

where we multiply (5.30) by a test function w_i .

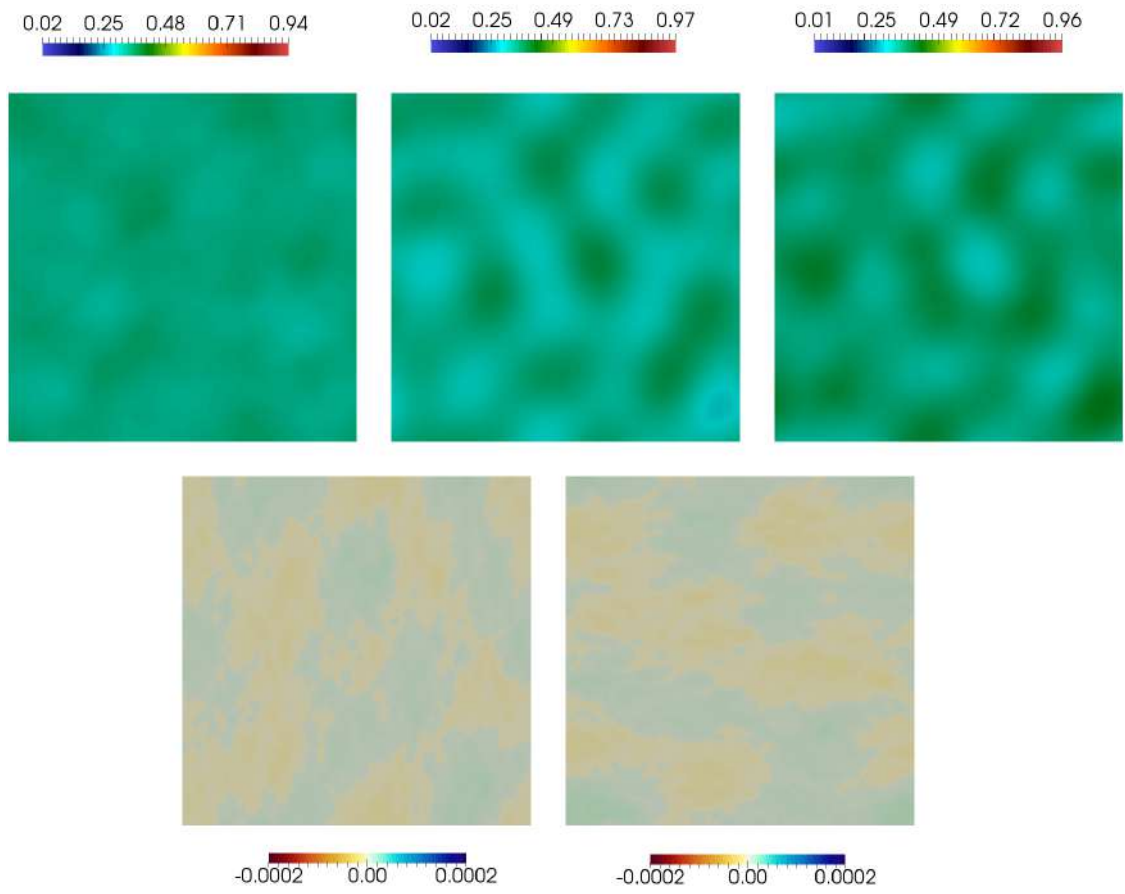


Figure 6.20 shows the beginning of the phase separation process. Top left: $\hat{\varphi}^1$; Top middle: $\hat{\varphi}^2$; Top right: $\hat{\varphi}^3$; Bottom left: u_x ; Bottom right: u_y .

At early stages Figure 6.20, $t < 4.04 \times 10^{-6}$, the solution goes through an initial spinodal decomposition. This spontaneous phase separation process occurs due to $\vartheta^{\alpha\beta} > \vartheta$. Otherwise, the mixture would only diffuse without unmixing. Due to the phases φ^1 , φ^2 , and φ^3 are diffusing as a result of their separation, the solid endures elastic deformation associated with the mass transport. Analogously, the pressure p_φ^α alters the rate at which the phases diffuse. The deformation arises solely from the mass transport since the reversible chemical reaction has no significant impact. From Figure 6.30, we verify that the phases masses do not change substantially in the range $0 < t < 4.04 \times 10^{-6}$. As a consequence, there is no nucleation and growth of phases. With regards of the interfacial energies, we notice that in the range $0 < t < 4.04 \times 10^{-6}$ the energies decrease gently up to a point, $t \simeq 1.0 \times 10^{-7}$, where the interfacial energies keep constant. A small change in the interfacial energies means that either the phase separation has not evolved significantly or there is no substantial coarsening. Furthermore, at early stages, the deformation is small as the displacements (see Figure 6.20) are not large since the phase separation has not evolved such that the phases are totally unmixed. As expected, the displacements u_x and u_y in the solid move following the mass transport.

Later on, in the range between $4.04 \times 10^{-6} < t < 9.03 \times 10^{-6}$, the phase separation becomes prominent as it allows to form spatial domains rich in each component (see Figure 6.21). In particular, the phase φ^1 remains partially unmixed as there are no rounded inclusions with large concentration (see Figure 6.21). On the contrary, for phases φ^2 and φ^3 , rounded inclusions with large concentration appear. The deformation results from the mass transport itself as there is no substantial influence of the reversible chemical reaction (see Figure 6.30). We notice the larger displacements are located where the larger inclusions for φ^2 and φ^3 are. This arises since there is mass flux towards these points which allows the inclusions to grow. The enlargement associated with the inclusions growth induces deformation. This behaviour is captured by \mathbf{F}^φ . With respect to the interfacial energies, they remain roughly constant. This implies that there is a balance between both the creating and disassemble of phases interfaces. As expected, in the time interval between $0 < t < 9.03 \times 10^{-6}$, the tendency of the global free energy is monotonically decreasing as the system goes to a steady state of maximum entropy (see Figure 6.31). This free energy encompasses the contribution from both the chemical and the mechanical energies. At the early stages, as the evolution towards a steady state goes on, the system favours phase

separation.

For instance, Figure 6.22 shows the evolution of microscopic φ^1 inclusions in the range between $9.03 \times 10^{-6} < t < 1.26 \times 10^{-5}$. As suggested before, there is mass flux towards these points that allows the inclusion growth. Consequently, there must be deformation associated with the mass transport. Figure 6.22 also shows the larger displacements in the regions where the inclusions are. On the other hand, φ^3 inclusions are large and close enough to start merging. This phenomena is associated with the minimisation of the global free energy as the system reduces its interfacial energies. Nevertheless, when considering system undergoing chemical reactions, the interfacial energies evolve according to the chemical reaction which in this modelling example corresponds to a reversible chemical reaction. The emerging of more φ^3 phase as a result of the reversible chemical reaction creates more φ^3 interface. Figure 6.30 shows an increase in φ^3 interfacial energy as well as its mass. On the other hand, the decomposition of φ^3 into φ^1 and φ^2 following (6.16) must increase φ^1 and φ^2 masses, and their interfacial energies. However, this behaviour is not prolonged since the rate of creation of φ^3 is faster than the decomposition into φ^1 and φ^2 . This is due to $k_+ \gg k_-$.

From $t = 5.64 \times 10^{-5}$, the system shows the merging of large inclusions and the action of the reversible chemical reaction (see Figure 6.23). At this stage, the creation of φ^3 predominates. One can verify such an assertion by checking the masses. However, there is no interfacial energy growth since the larger inclusions are merging. Therefore, the interfacial energies decrease. Moreover, the φ^1 , φ^2 , and φ^3 inclusions pass from rounded to square-like structures. Such behaviour results from the dependency of the chemical potential upon the pressure p_φ^α caused by deformation and the Gibbs-Thomson effect associated with the curvature $\Delta\varphi_R^\alpha$. Along the boundaries of the inclusions the driving force of the mass transport changes which may generate inclusions of asymmetric morphologies. Moreover, the creation of φ^1 , φ^2 , and φ^3 following (6.16) engenders mechanical pressure associated with nucleation and growth. Figure 6.23 also shows the large displacements at the phases boundaries which account for the influence of the chemical reaction towards stress generation (pressure).

Figure 6.24 shows the evolution at $t = 4.26 \times 10^{-4}$. The system forms a chain-like structure composed of the phases φ^1 and φ^2 which is surrounded by the phase φ^3 . This structure emerges as a result of the merging processes and the reversible

chemical reaction. The reversible chemical reaction is still taking place at the boundary between phases φ^1 and φ^2 . Moreover, the phase φ^3 decomposes into φ^1 and φ^2 . At this point in the evolution, the phase φ^3 composes almost the whole solid due to $k_+ \gg k_-$. The masses and interfacial energies for phases φ^1 and φ^2 decrease (see Figure 6.30). However, for phase φ^3 the mass increase while reducing its interfacial energy (see Figure 6.30). The phases are totally unmixed, whereby their concentrations correspond to the concentrations at the well points in the triple-well function. The displacements u_x and u_y are in the range of previous stages. However, they move as the phases diffuse as a result of the relation between mass transport and deformation. Figure 6.24 depicts the larger displacements are in line with the chain-like structure.

Figure 6.25 portrays the evolution at $t = 5.72 \times 10^{-4}$. The minimisation of the global free energy as the system goes to the steady state reduces the thickness of the chain-like structure. Eventually, the chain is composed of interleaved inclusion of phases φ^1 and φ^2 . As the inclusions of φ^1 and φ^2 become smaller, the phase φ^3 encloses φ^1 and φ^2 . The interfacial energies and masses keep decreasing since the action of the reversible chemical reaction has not ceased (see Figure 6.30). Moreover, the displacements show an interleaved behaviour where the smaller displacements are located inside the chain-like structure and the larger ones outside.

In the time interval between $5.72 \times 10^{-4} < t < 1.84 \times 10^{-3}$, the inclusions of phases φ^1 and φ^2 become smaller progressively as the reversible reaction takes place at their boundaries (see Figures 6.26, 6.27, and 6.28). When the reversible chemical reaction ceases, the structure of the inclusions is rounded. The action of the chemical reaction is in the range between $1 \times 10^{-5} < t < 1 \times 10^{-2}$. The larger and smaller displacements, on the other hand, are located along the inclusion of phases φ^1 and φ^2 . These phases are partially consumed while the phase φ^3 gains mass. Finally, rounded structures composed of the three phases diffuse along the solid which generate displacements associated with mass transport. Figure 6.29 portrays such a behaviour. Along with the whole evolution, free energy always behaves monotonically decreasing (see Figure 6.31).

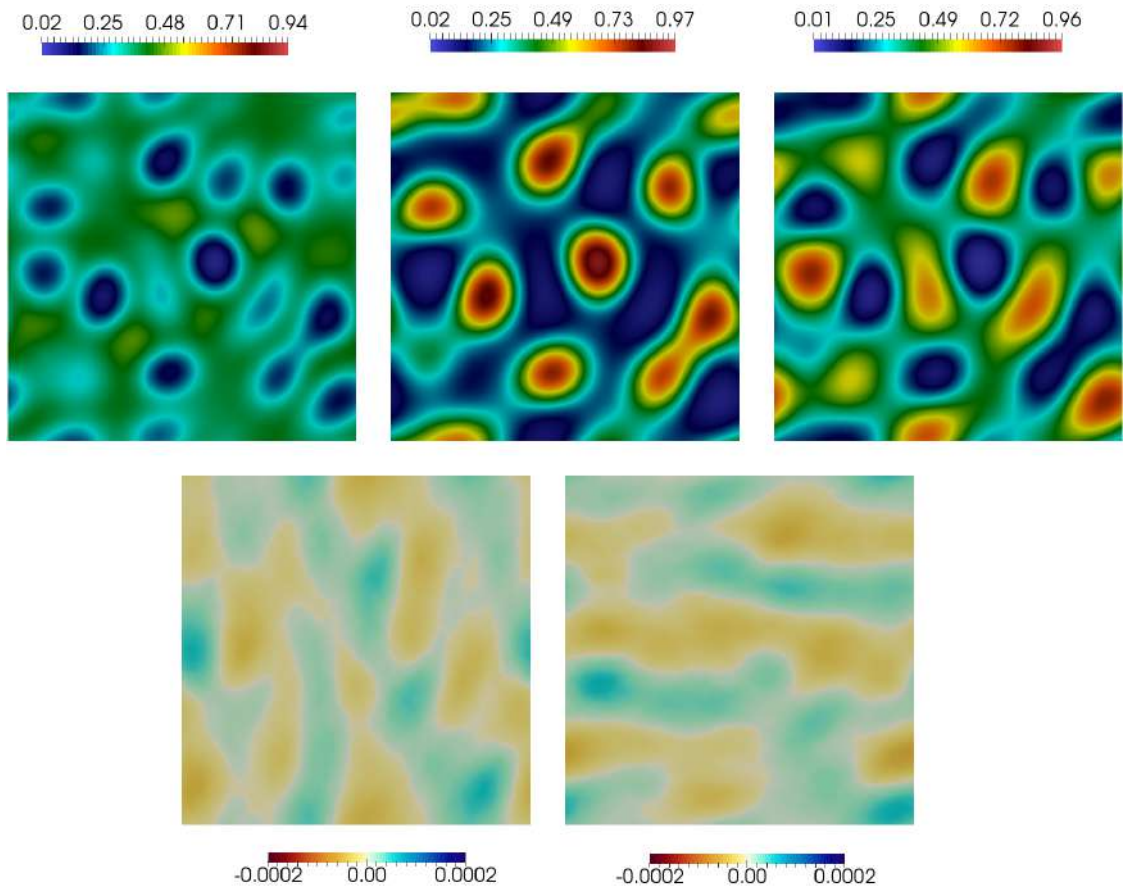


Figure 6.21 shows the evolution at $t = 9.03 \times 10^{-6}$. Top left: $\dot{\varphi}^1$; Top middle: $\dot{\varphi}^2$; Top right: $\dot{\varphi}^3$; Bottom left: u_x ; Bottom right: u_y .

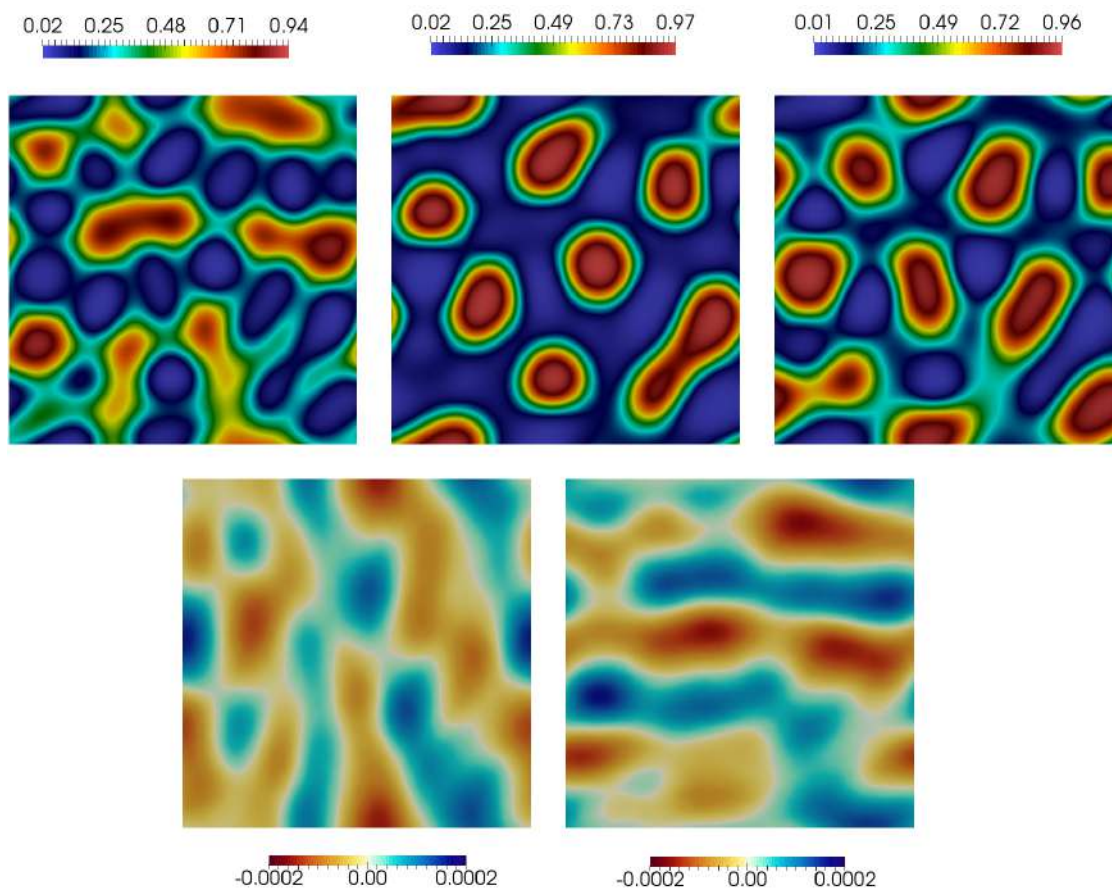


Figure 6.22 shows the evolution at $t = 1.26 \times 10^{-5}$. Top left: $\hat{\varphi}^1$; Top middle: $\hat{\varphi}^2$; Top right: $\hat{\varphi}^3$; Bottom left: u_x ; Bottom right: u_y .

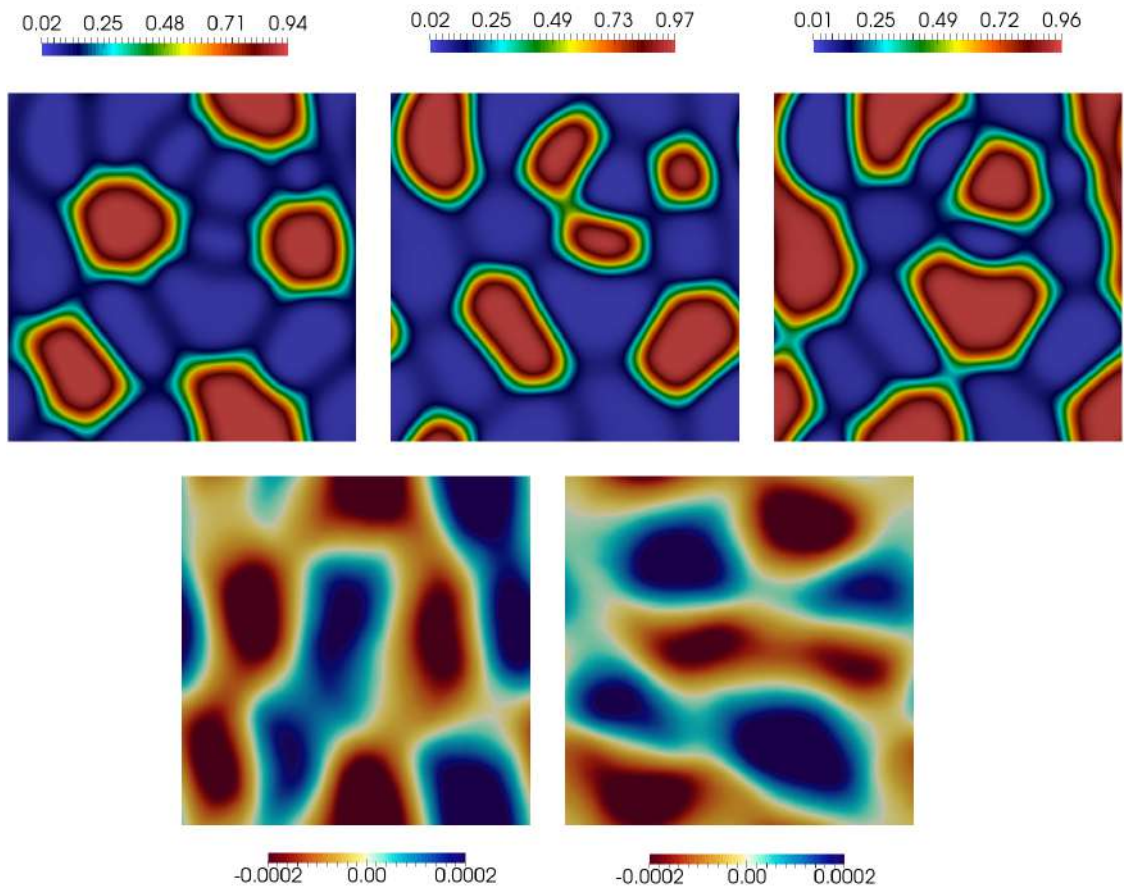


Figure 6.23 shows the evolution at $t = 5.64 \times 10^{-5}$. Top left: $\hat{\varphi}^1$; Top middle: $\hat{\varphi}^2$; Top right: $\hat{\varphi}^3$; Bottom left: u_x ; Bottom right: u_y .

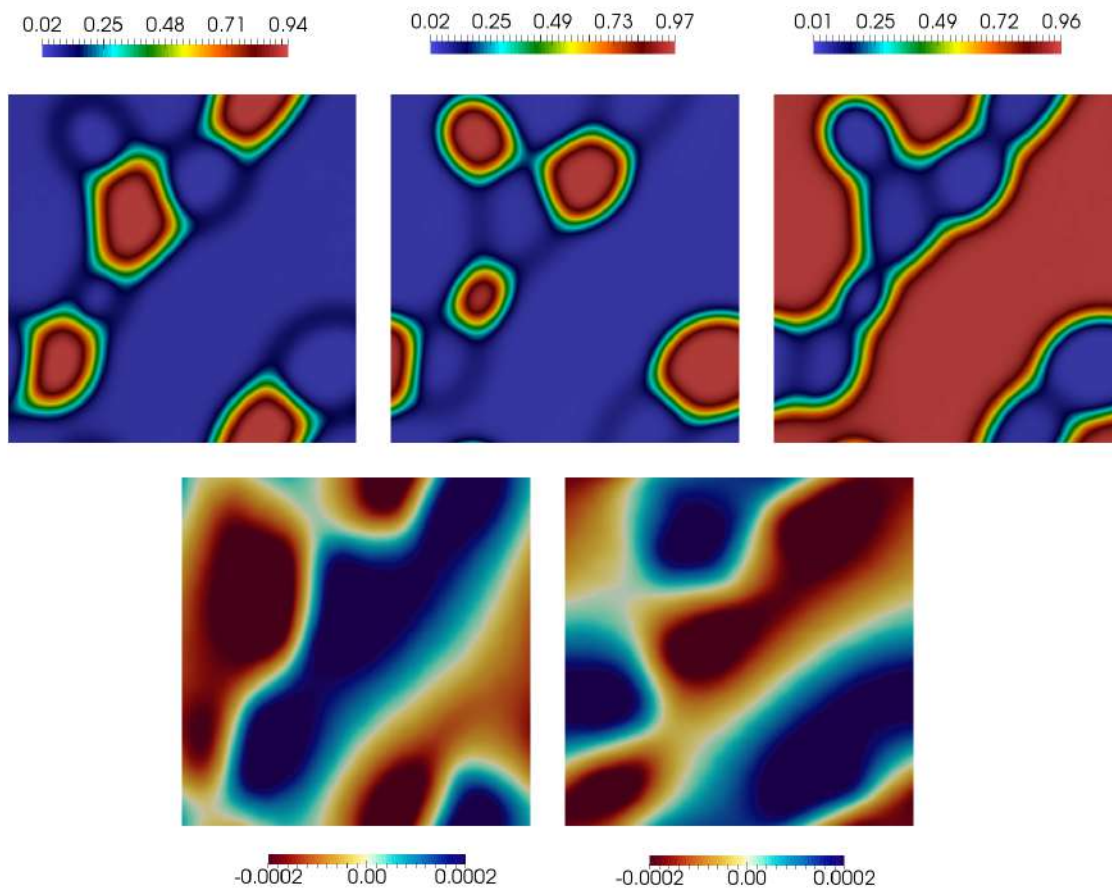


Figure 6.24 shows the evolution at $t = 4.26 \times 10^{-4}$. Top left: $\hat{\varphi}^1$; Top middle: $\hat{\varphi}^2$; Top right: $\hat{\varphi}^3$; Bottom left: u_x ; Bottom right: u_y .

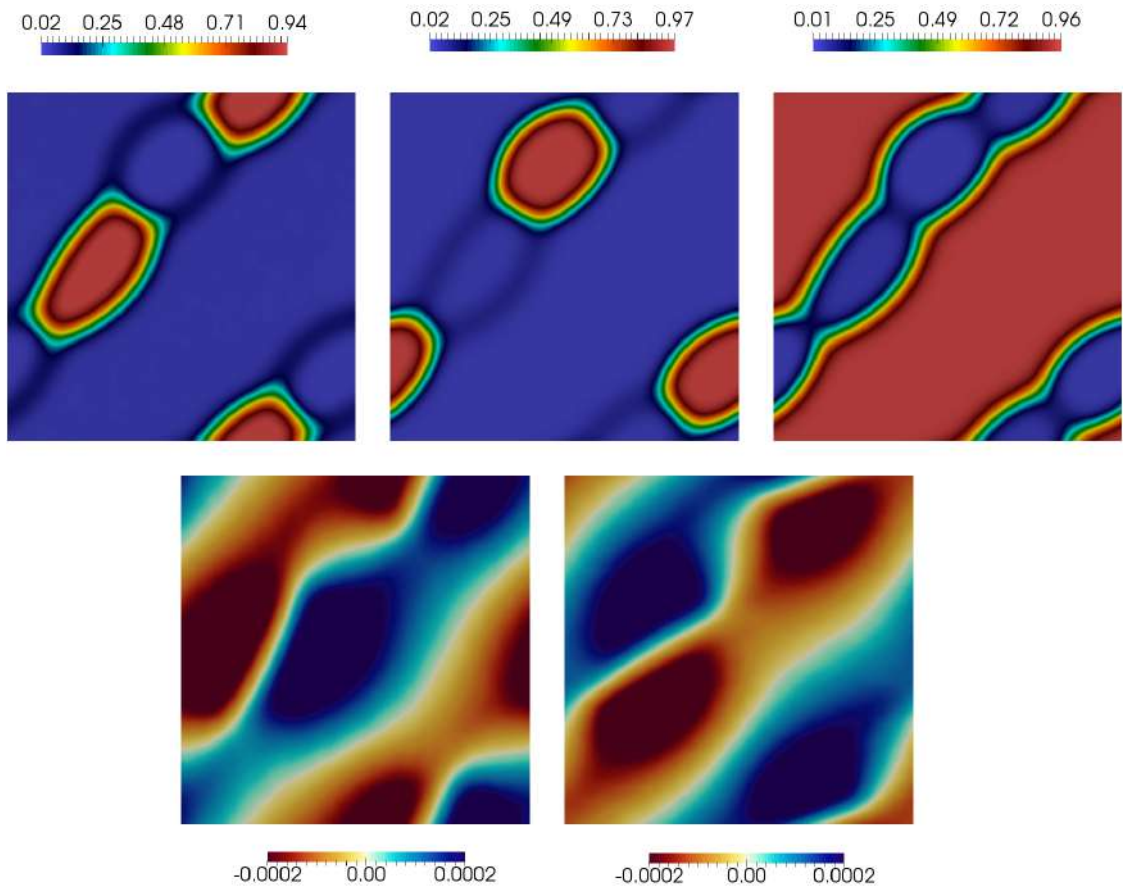


Figure 6.25 shows the evolution at $t = 5.72 \times 10^{-4}$. Top left: $\dot{\varphi}^1$; Top middle: $\dot{\varphi}^2$; Top right: $\dot{\varphi}^3$; Bottom left: u_x ; Bottom right: u_y .

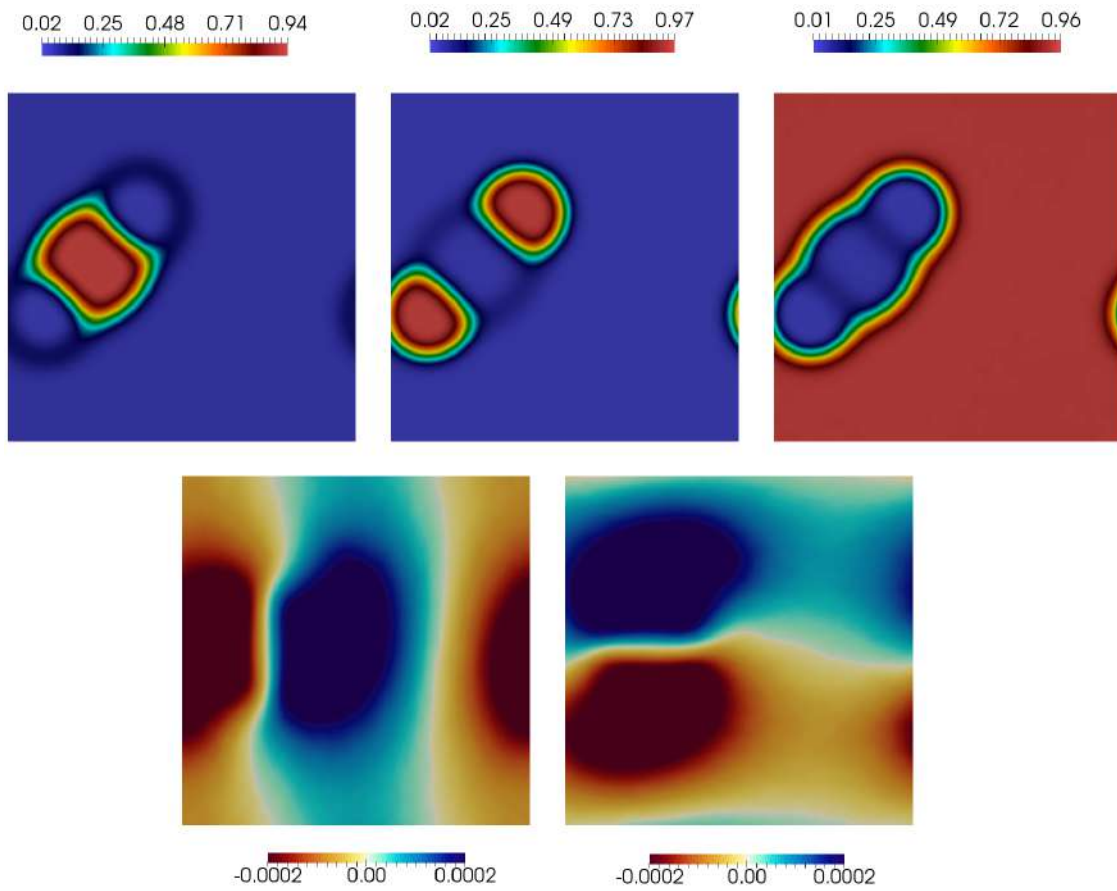


Figure 6.26 shows the evolution at $t = 1.28 \times 10^{-3}$. Top left: $\hat{\varphi}^1$; Top middle: $\hat{\varphi}^2$; Top right: $\hat{\varphi}^3$; Bottom left: u_x ; Bottom right: u_y .

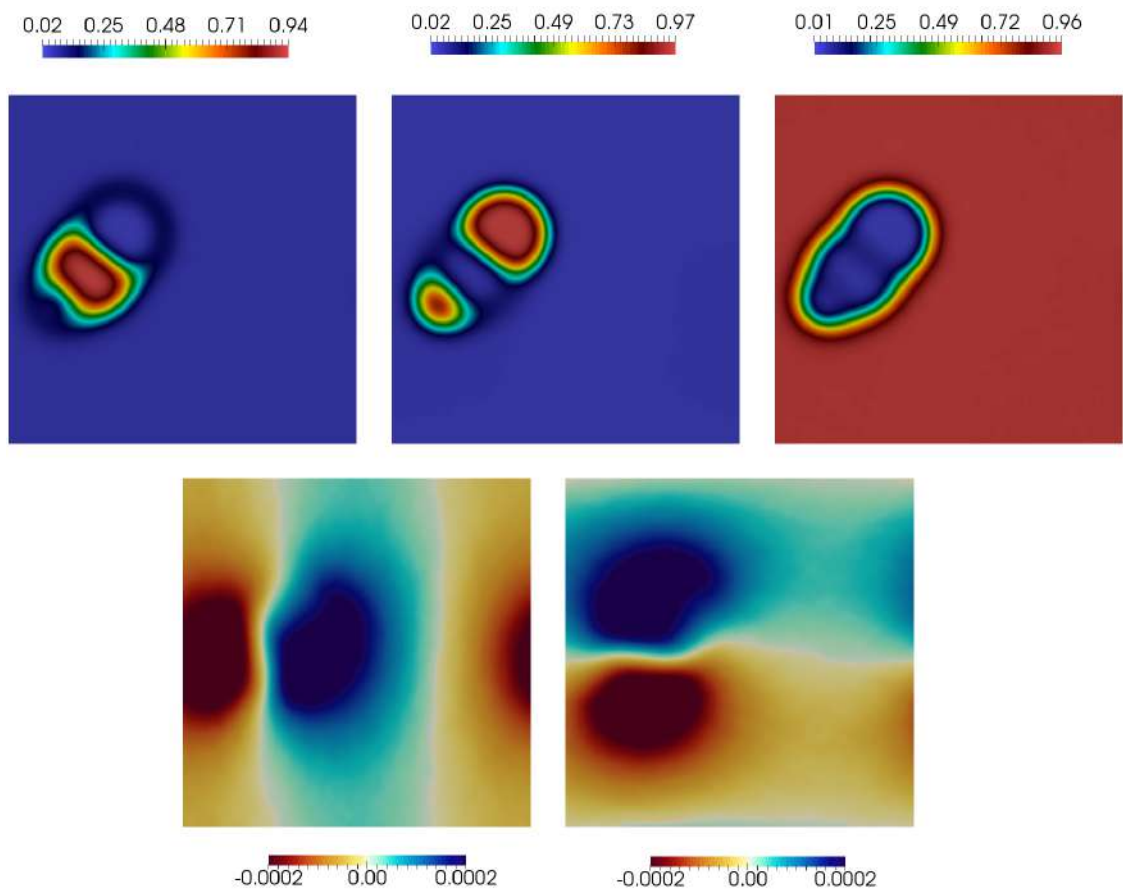


Figure 6.27 shows the evolution at $t = 1.84 \times 10^{-3}$. Top left: $\hat{\varphi}^1$; Top middle: $\hat{\varphi}^2$; Top right: $\hat{\varphi}^3$; Bottom left: u_x ; Bottom right: u_y .

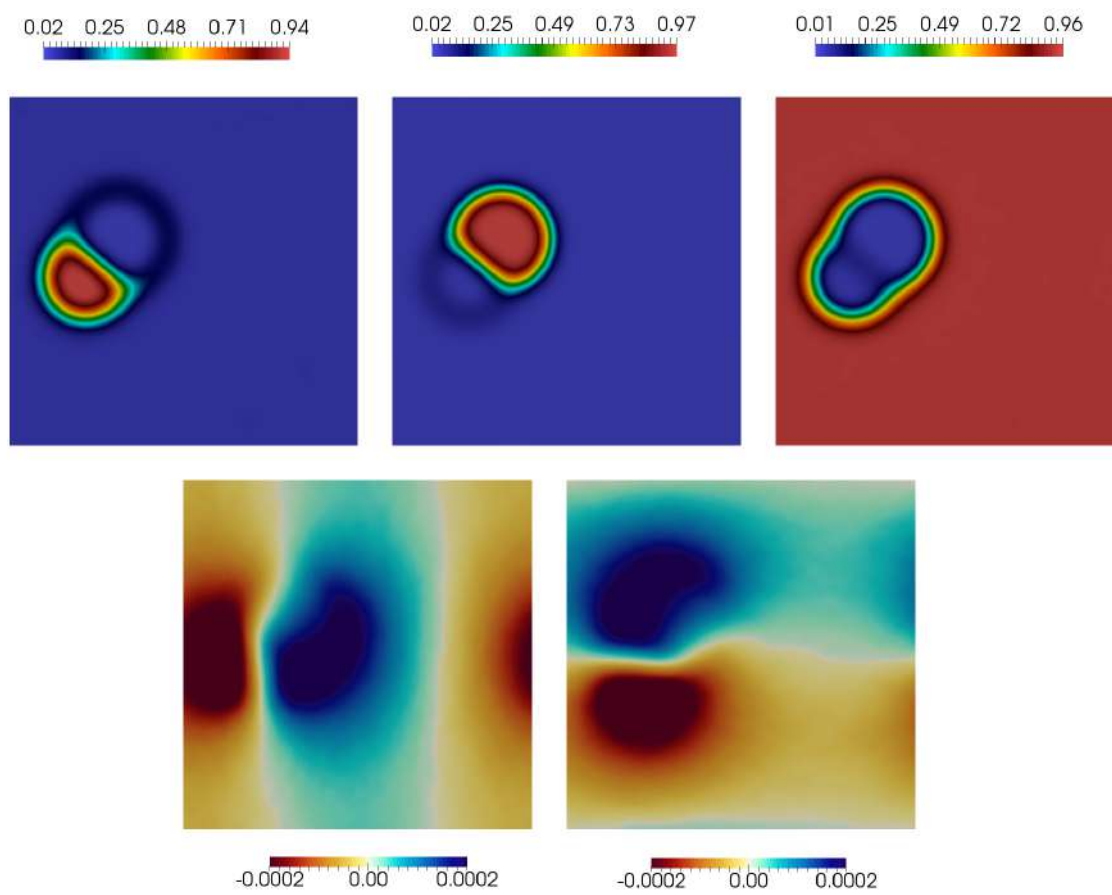


Figure 6.28 shows the evolution at $t = 2.17 \times 10^{-3}$. Top left: $\hat{\varphi}^1$; Top middle: $\hat{\varphi}^2$; Top right: $\hat{\varphi}^3$; Bottom left: u_x ; Bottom right: u_y .

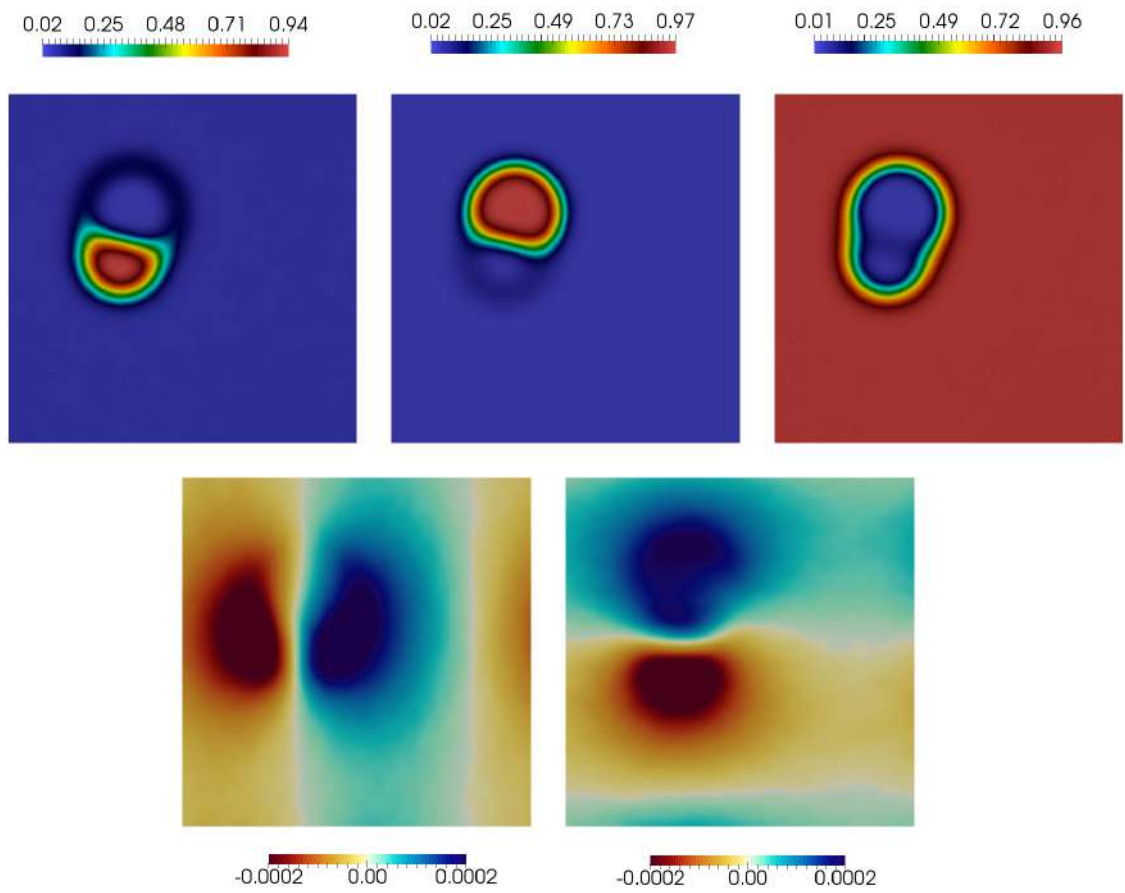


Figure 6.29 shows the steady state reached at $t = 1.74 \times 10^{-1}$. Top left: φ^1 ; Top middle: φ^2 ; Top right: φ^3 ; Bottom left: u_x ; Bottom right: u_y .

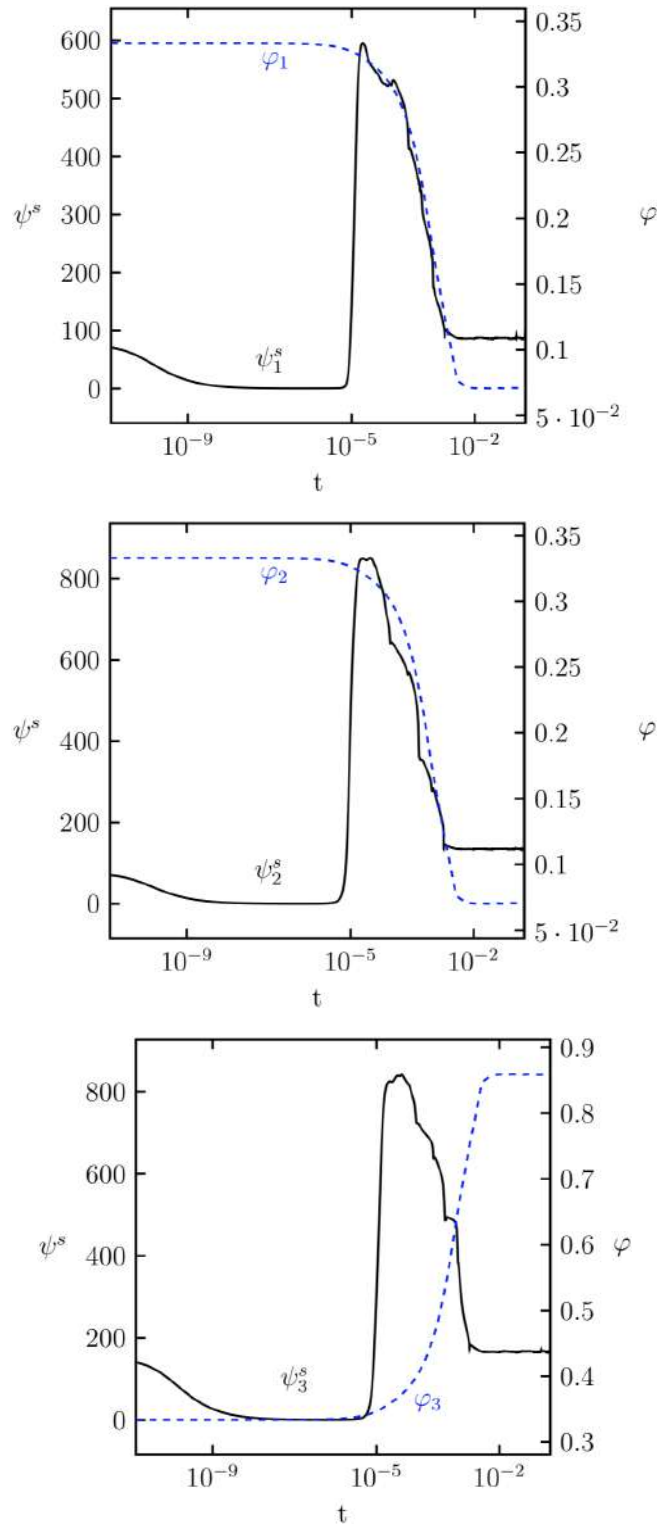


Figure 6.30 Interfacial energies for phases ϕ^1 , ϕ^2 , and ϕ^3 along with their masses

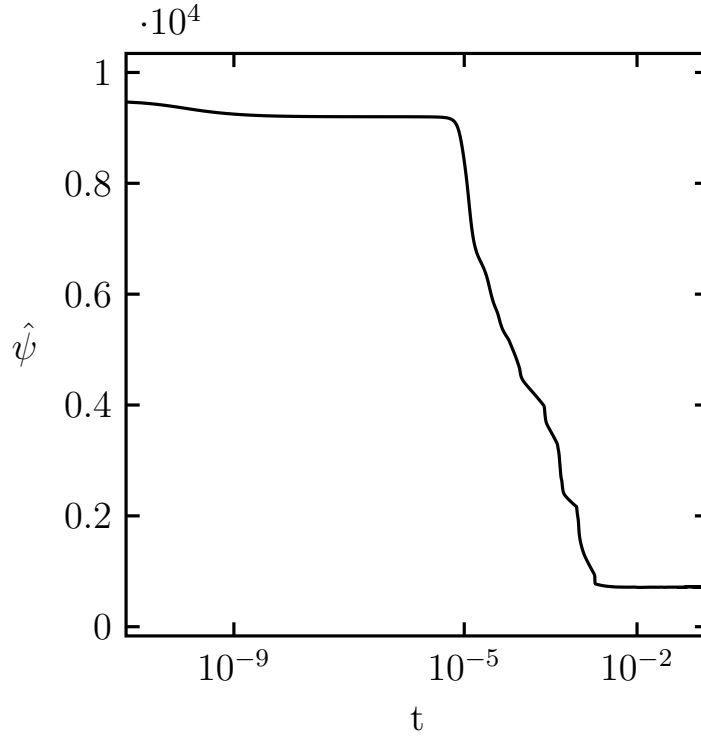


Figure 6.31 depicts the free energy evolution. During the whole evolution, the free energy is monotonically-decreasing.

6.4.2 Ripening of spherical inclusions

We carry out a numerical simulation of a 3D configuration of three spherical inclusions. The spherical inclusions are composed of phases $\hat{\varphi}^1$ and $\hat{\varphi}^2$ while phase $\hat{\varphi}^3$ serves as an interstitial phase. We study the stress-assisted volume changes mechanism triggered by the mass transport of the spherical inclusions associated with interfacial effects. We expect Ostwald ripening as a result of the differences in the inclusions size. We do not consider external contributions from body forces and external microforces. Consequently, we set $\mathbf{b} = \mathbf{0}$ and $\gamma^\alpha = 0$. Regarding the kinematics of the motion, we set $\mathbf{v} = \mathbf{0}$ as we do not take into account inertial effects. We do not allow for chemical reactions between the phases, and therefore, the reactions rates k_+ and k_- are zero. The latter entails that $s^\alpha = 0.0$. Hence, the stresses emerge solely from the mass transport associated with the interfacial interactions between the phases. Without loss of generality, the initial condition serves as the reference configuration. We choose this reference state as an underformed configuration of the body. The initial and

boundary conditions are given by

$$\begin{aligned}
S_1 &= (x - 0.25)^2 + (y - 0.25)^2 + (z - 0.25)^2 - 0.2^2 \\
S_2 &= (x - 0.75)^2 + (y - 0.75)^2 + (z - 0.75)^2 - 0.1^2 \\
S_3 &= (x - 0.75)^2 + (y - 0.75)^2 + (z - 0.3)^2 - 0.08^2 \\
h &= 0.2 \\
\delta^1 &= 0.31 - 0.8 \left(0.5 \tanh \left(\frac{S_1}{0.01h(h + 2.0)} \right) + 0.5 \right) \\
\delta^2 &= 0.31 - 0.8 \left(0.5 \tanh \left(\frac{S_2}{0.01h(h + 1.0)} \right) + 0.5 \right) \\
\delta^3 &= 0.31 - 0.8 \left(0.5 \tanh \left(\frac{S_3}{0.01h(h + 0.8)} \right) + 0.5 \right) \\
\varphi_0^1 &= 1 + \delta_1 + \delta_2, \\
\varphi_0^2 &= \delta_3, \\
\varphi_0^3 &= 1 - \varphi_0^1 - \varphi_0^2, \\
\mathbf{u} &= \mathbf{0}
\end{aligned} \tag{6.22}$$

in \mathbf{P} , subject to periodic boundary conditions on $\partial\mathbf{P} \times (0, T)$.

As in previous simulation examples, the range of the chemical and physical parameters are in the range of common processes in geosciences. We use the same parameters as in §6.4.1. The three phases diffuse with the same diffusion coefficient. Furthermore, the dimensionless numbers correspond to (6.18). As mentioned before, the phase $\hat{\varphi}^3$ serves as an interstitial phase following the mass constraint given by (5.24). Figures 6.32 and 6.33 show the initial condition for the phases distribution and displacements, respectively. The system of equations to solve is given by

$$\dot{\varphi}^1 = -\text{Div} \mathbf{J}_{\mathbf{R}^3}^1, \tag{6.23a}$$

$$\dot{\varphi}^2 = -\text{Div} \mathbf{J}_{\mathbf{R}^3}^2, \tag{6.23b}$$

$$\text{Div} \mathbf{T}_{\mathbf{R}} = \mathbf{0}. \tag{6.23c}$$

where we use the phase $\hat{\varphi}^3$ as the reference species. We solve the system of partial differential equation (6.23) in its primal form (6.20) and (6.21). We state the problem as follows: find $\{\varphi, \mathbf{u}\} \in \mathcal{C}^2(\mathbf{P})$ such that (5.80) given (5.73) subject to periodic boundary conditions up to the second derivative of φ , and \mathbf{u} with respect to \mathbf{X} in a square open region $\mathbf{P} = (0, 1) \times (0, 1)$. We use the PetIGA [116] isogeometric analysis framework. We use $64 \times 64 \times 64$ element mesh of a polynomial degree 2 and continuity 1.

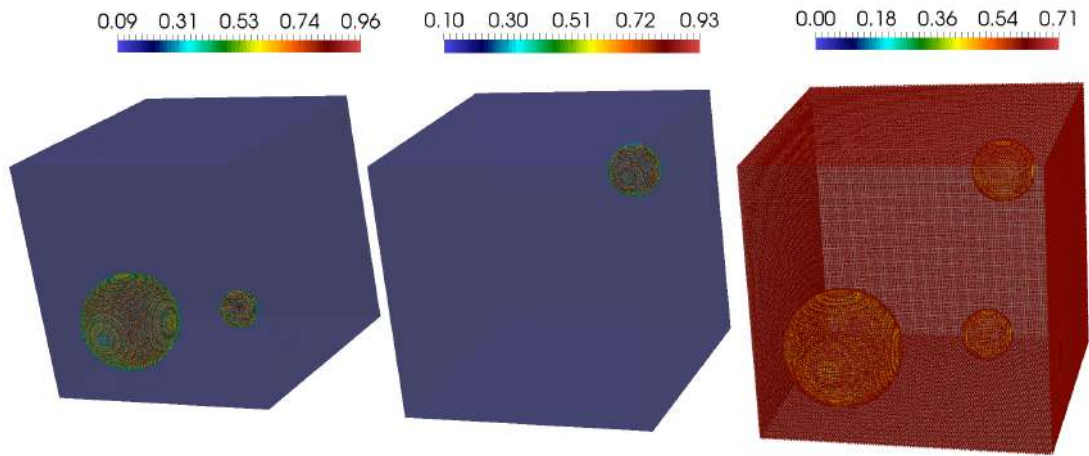


Figure 6.32 represents the spatial distribution of the initial concentrations for φ^1 , φ^2 , and φ^3 . Left: φ^1 ; Middle: φ^2 ; Right: φ^3 . The inclusions differ in size which drives the ripening process.

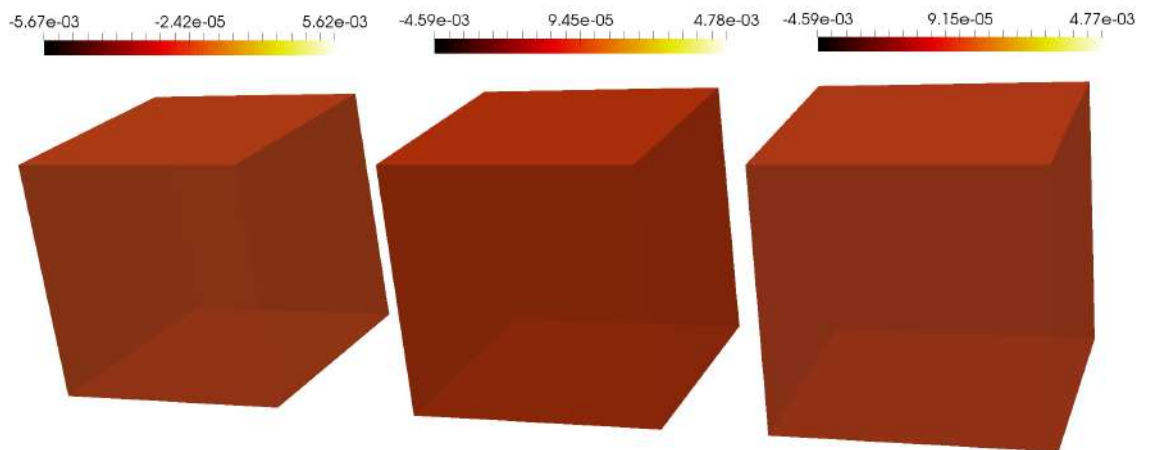


Figure 6.33 portrays the initial displacements in the solid. The initial state corresponds to a undeformed solid, therefore the displacements are zero. The deformation will result from the mass transport of the phases as the smaller inclusions go into the solution and deposit in the surface of the larger inclusions. Left: u_x ; Middle: u_y ; Right: u_z

At early stages Figures 6.32 and 6.33, $t < 1.182 \times 10^{-6}$, part of the phase φ^1 deposits on the surface of the inclusion φ^2 due to a new spherical inclusion φ^1 of same radius appears. As the evolution proceeds, between the time range $1.182 \times 10^{-6} < t < 2.79 \times 10^{-6}$, the inclusion of phase φ^2 becomes smaller as its mass goes into the solution. There is no deposition of phase φ^2 at this point in the evolution. Regarding the deformation, the stresses associated with the volume changes are small since the displacements do not change substantially (see Figure 6.35). Nevertheless, after $t > 5.476 \times 10^{-6}$, rings composed of phases φ^1 and φ^2 appear around φ^1 . This occurs due to the solution gets supersaturated and the mass of phases φ^1 and φ^2 migrate at the surface of the more energetically stable structures in the system, which in this case correspond to the spherical inclusions (see Figure 6.36). Such mass transport induces volumetric stresses and concomitant displacements around the spherical inclusions (see Figure 6.37). As the system tries to minimise its free energy, the masses of phases φ^1 , φ^2 , and φ^3 in the solution separate and merge to form new spherical structures (see Figure 6.38). The phase φ^2 locates around the spherical inclusions of φ^1 . As mentioned before, the fact that the phases are diffusing must induce volumetric stresses. Consequently, we see displacements where the phases are separating and merging (see Figure 6.39). Later on, $t > 5.626 \times 10^{-3}$, the spherical inclusions composed of phase φ^1 and φ^2 merge to form a more energetically stable distribution of elongated structure (see Figure 6.40). Finally, the phase φ^2 wraps the phase φ^1 , and φ^3 acts as an interstitial phase. The structure at steady state emerges as a result of the coupled chemo-mechanical interactions of the three-component system where the source of stress generation solely results from the mass transport of the phases (see Figure 6.41).

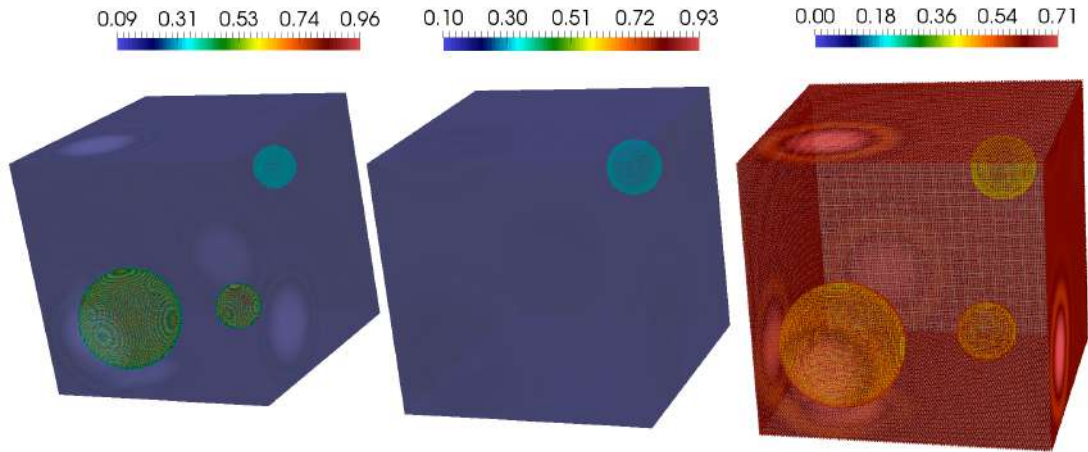


Figure 6.34 represents the spatial distribution of the concentrations for φ^1 , φ^2 , and φ^3 at $t = 2.79 \times 10^{-6}$. Left: φ^1 ; Middle: φ^2 ; Right: φ^3 .

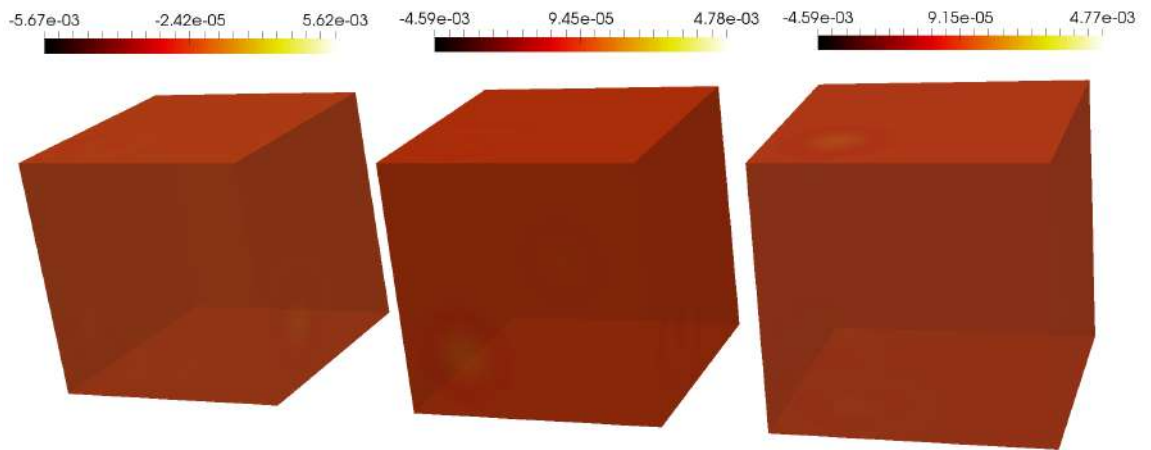


Figure 6.35 portrays the displacements in the solid at $t = 2.79 \times 10^{-6}$. Left: u_x ; Middle: u_y ; Right: u_z .

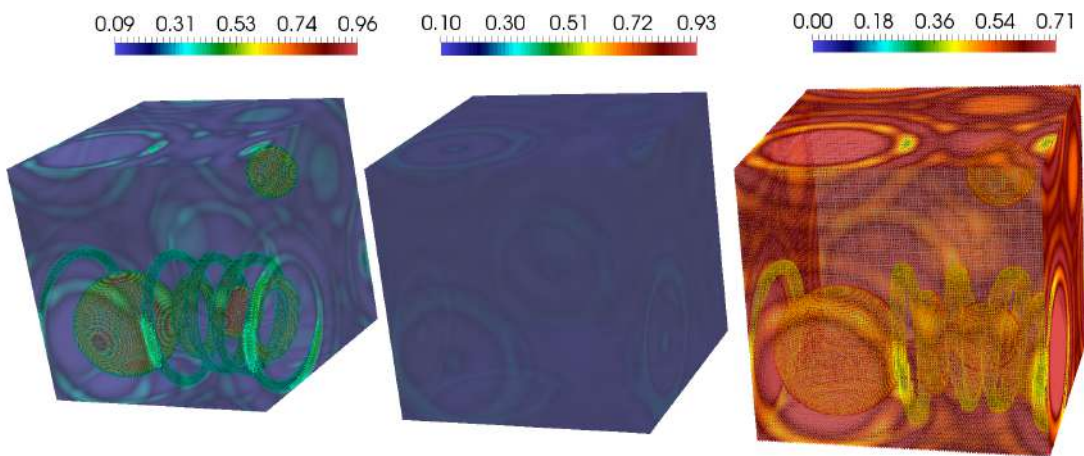


Figure 6.36 represents the spatial distribution of the concentrations for φ^1 , φ^2 , and φ^3 at $t = 5.476 \times 10^{-6}$. Left: φ^1 ; Middle: φ^2 ; Right: φ^3 .

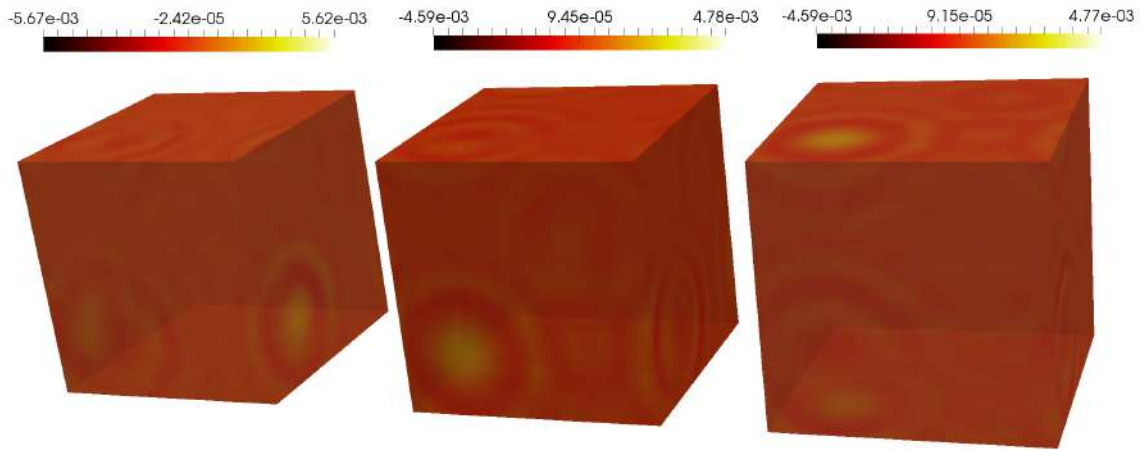


Figure 6.37 portraits the displacements in the solid at $t = 5.476 \times 10^{-6}$. Left: u_x ; Middle: u_y ; Right: u_z .

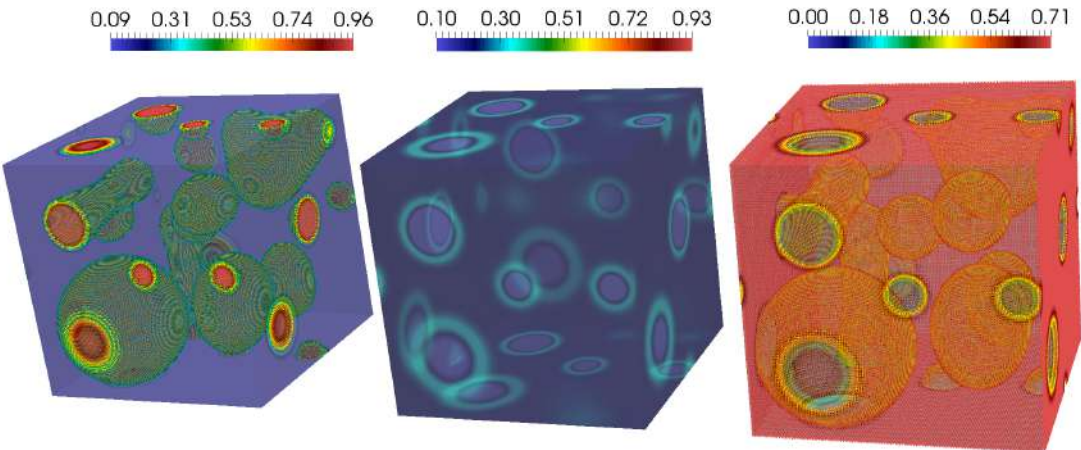


Figure 6.38 represents the spatial distribution of the concentrations for $\hat{\varphi}^1$, $\hat{\varphi}^2$, and $\hat{\varphi}^3$ at $t = 5.626 \times 10^{-3}$. Left: $\hat{\varphi}^1$; Middle: $\hat{\varphi}^2$; Right: $\hat{\varphi}^3$.

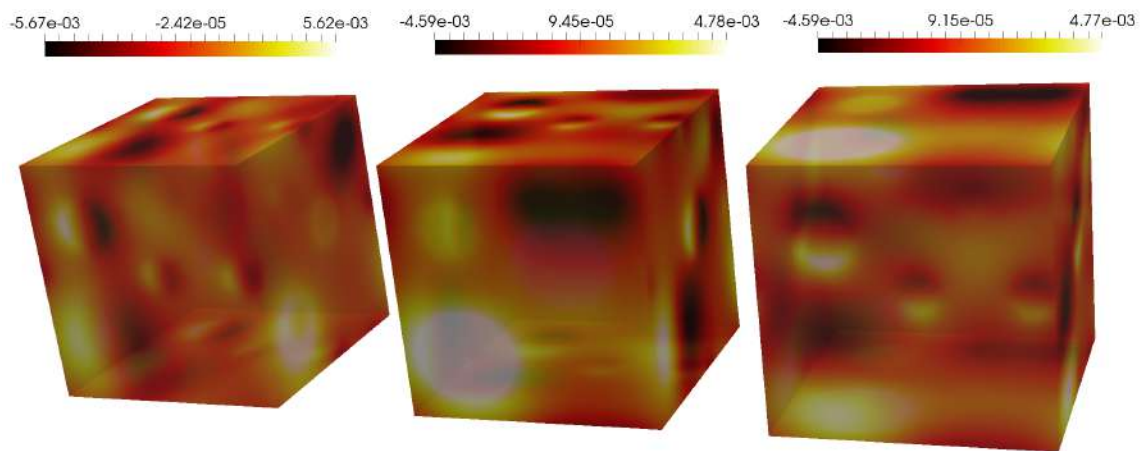


Figure 6.39 portraits the displacements in the solid at $t = 5.626 \times 10^{-3}$. Left: u_x ; Middle: u_y ; Right: u_z .

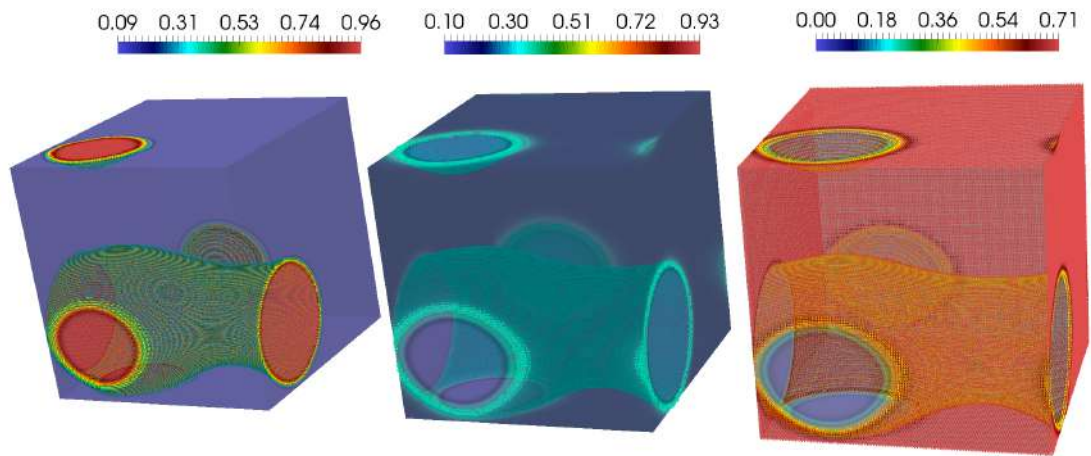


Figure 6.40 represents the spatial distribution of the concentrations for φ^1 , φ^2 , and φ^3 at steady state. Left: φ^1 ; Middle: φ^2 ; Right: φ^3 .

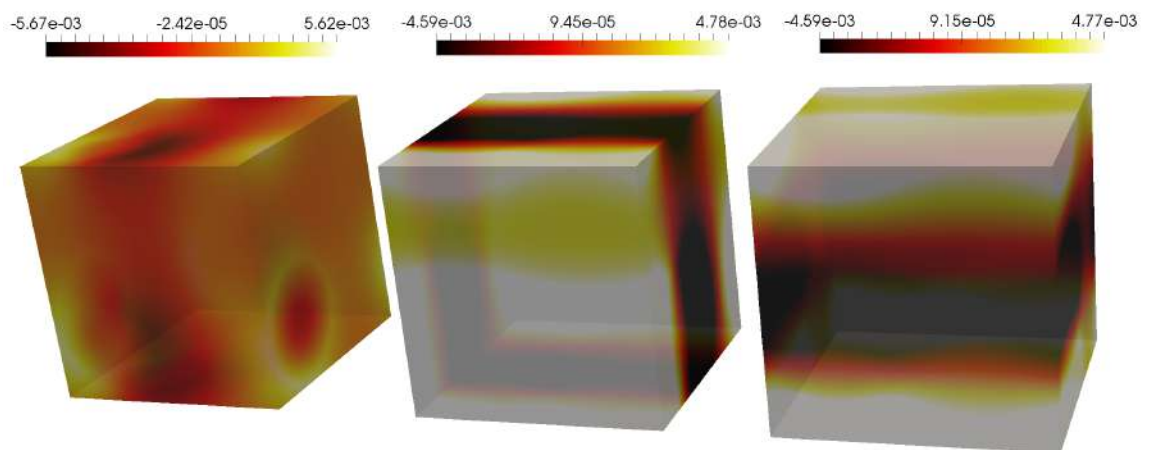


Figure 6.41 portrays the displacements in the solid at steady state. Left: u_x ; Middle: u_y ; Right: u_z .

Bibliography

- [1] L. Tajčmanová, J. Vrijmoed, E. Moulas, Grain-scale pressure variations in metamorphic rocks: implications for the interpretation of petrographic observations, *Lithos* 216 (2015) 338–351.
- [2] R. Milke, R. Abart, K. Kunze, M. KOCH-MÜLLER, D. Schmid, P. Ulmer, Matrix rheology effects on reaction rim growth i: evidence from orthopyroxene rim growth experiments, *Journal of Metamorphic Geology* 27 (1) (2009) 71–82.
- [3] B. E. Hobbs, A. Ord, Does non-hydrostatic stress influence the equilibrium of metamorphic reactions?, *Earth-Science Reviews* 163 (2016) 190–233.
- [4] E. Moulas, Y. Podladchikov, L. Y. Aranovich, D. Kostopoulos, The problem of depth in geology: When pressure does not translate into depth, *Petrology* 21 (6) (2013) 527–538.
- [5] J. C. Vrijmoed, Y. Y. Podladchikov, Thermodynamic equilibrium at heterogeneous pressure, *Contributions to Mineralogy and Petrology* 170 (1) (2015) 10.
- [6] J. Wheeler, Dramatic effects of stress on metamorphic reactions, *Geology* 42 (8) (2014) 647–650.
- [7] X. Zhong, J. Vrijmoed, E. Moulas, L. Tajčmanová, A coupled model for intragranular deformation and chemical diffusion, *Earth and Planetary Science Letters* 474 (2017) 387–396.
- [8] D. Howell, I. Wood, D. Dobson, A. Jones, L. Nasdala, J. Harris, Quantifying strain birefringence halos around inclusions in diamond, *Contributions to Mineralogy and Petrology* 160 (5) (2010) 705–717.

- [9] R. Powell, K. A. Evans, E. C. Green, R. W. White, On equilibrium in non-hydrostatic metamorphic systems, *Journal of Metamorphic Geology* 36 (4) (2018) 419–438.
- [10] F. Larché, J. W. Cahn, A linear theory of thermochemical equilibrium of solids under stress, *Acta metallurgica* 21 (8) (1973) 1051–1063.
- [11] M. E. Gurtin, An introduction to continuum mechanics, Vol. 158, Academic press, 1982.
- [12] F. Larché, J. W. Cahn, A nonlinear theory of thermochemical equilibrium of solids under stress, *Acta Metallurgica* 26 (1) (1978) 53–60.
- [13] L. Tajčmanová, Y. Podladchikov, R. Powell, E. Moulas, J. Vrijmoed, J. Connolly, Grain-scale pressure variations and chemical equilibrium in high-grade metamorphic rocks, *Journal of Metamorphic Geology* 32 (2) (2014) 195–207.
- [14] B. E. Hobbs, A. Ord, Coupling of fluid flow to permeability development in mid-to upper crustal environments: a tale of three pressures, Geological Society, London, Special Publications 453 (2017) SP453–9.
- [15] L. S. Bennethum, T. Weinstein, Three pressures in porous media, *Transport in Porous Media* 54 (1) (2004) 1–34.
- [16] R. Yund, A. McLaren, B. Hobbs, Coarsening kinetics of the exsolution microstructure in alkali feldspar, *Contributions to mineralogy and petrology* 48 (1) (1974) 45–55.
- [17] E. Petrishcheva, R. Abart, Exsolution by spinodal decomposition in multi-component mineral solutions, *Acta materialia* 60 (15) (2012) 5481–5493.
- [18] K. Miyazaki, Ostwald ripening of garnet in high p/t metamorphic rocks, *Contributions to Mineralogy and Petrology* 108 (1-2) (1991) 118–128.
- [19] D. D. Eberl, J. Środoń, M. Kralik, B. E. Taylor, Z. E. Peterman, Ostwald ripening of clays and metamorphic minerals, *Science* 248 (4954) (1990) 474–477.
- [20] A. Nemchin, L. Giannini, S. Bodorkos, N. Oliver, Ostwald ripening as a possible mechanism for zircon overgrowth formation during anatexis: theoretical constraints, a numerical model, and its application to pelitic migmatites

- of the tickalara metamorphics, northwestern australia, *Geochimica et Cosmochimica Acta* 65 (16) (2001) 2771–2788.
- [21] E. Petrishcheva, R. Abart, Exsolution by spinodal decomposition i: Evolution equation for binary mineral solutions with anisotropic interfacial energy, *American Journal of Science* 309 (6) (2009) 431–449.
- [22] F. Amiri, D. Millán, Y. Shen, T. Rabczuk, M. Arroyo, Phase-field modeling of fracture in linear thin shells, *Theoretical and Applied Fracture Mechanics* 69 (2014) 102–109.
- [23] M. J. Borden, C. V. Verhoosel, M. A. Scott, T. J. Hughes, C. M. Landis, A phase-field description of dynamic brittle fracture, *Computer Methods in Applied Mechanics and Engineering* 217 (2012) 77–95.
- [24] A. Hernández-Machado, A. Lacasta, E. Mayoral, E. C. Poiré, Phase-field model of hele-shaw flows in the high-viscosity contrast regime, *Physical Review E* 68 (4) (2003) 046310.
- [25] S.-L. Wang, R. Sekerka, A. Wheeler, B. Murray, S. Coriell, R. Braun, G. McFadden, Thermodynamically-consistent phase-field models for solidification, *Physica D: Nonlinear Phenomena* 69 (1-2) (1993) 189–200.
- [26] J. D. Van der Waals, The thermodynamic theory of capillarity under the hypothesis of a continuous variation of density, *Journal of Statistical Physics* 20 (2) (1979) 200–244.
- [27] J. W. Cahn, J. E. Hilliard, Free energy of a nonuniform system. I. Interfacial free energy, *The Journal of Chemical Physics* 28 (2) (1958) 258–267.
- [28] E. Khain, L. M. Sander, Generalized Cahn-Hilliard equation for biological applications, *Physical Review E* 77 (5) (2008) 051129.
- [29] X. Wu, G. Zwieter, K. Zee, Stabilized second-order convex splitting schemes for Cahn-Hilliard models with application to diffuse-interface tumor-growth models, *International journal for numerical methods in biomedical engineering* 30 (2) (2014) 180–203.
- [30] Z. Bi, R. F. Sekerka, Phase-field model of solidification of a binary alloy, *Physica A: Statistical Mechanics and its Applications* 261 (1-2) (1998) 95–106.

- [31] C. P. Grant, Spinodal decomposition for the cahn-hilliard equation, *Communications in Partial Differential Equations* 18 (3-4) (1993) 453–490.
- [32] J. W. Cahn, J. E. Hilliard, Free energy of a nonuniform system. i. interfacial free energy, *The Journal of chemical physics* 28 (2) (1958) 258–267.
- [33] M. E. Gurtin, E. Fried, L. Anand, *The Mechanics and Thermodynamics of Continua*, Cambridge University Press, 2010.
- [34] H. Dal, C. Miehe, Computational electro-chemo-mechanics of lithium-ion battery electrodes at finite strains, *Computational Mechanics* 55 (2) (2015) 303–325.
- [35] C. Miehe, H. Dal, L.-M. Schänzel, A. Raina, A phase-field model for chemo-mechanical induced fracture in lithium-ion battery electrode particles, *International Journal for Numerical Methods in Engineering* 106 (9) (2016) 683–711.
- [36] I. Tsagrakis, E. C. Aifantis, Thermodynamic coupling between gradient elasticity and a Cahn-Hilliard type of diffusion: size-dependent spinodal gaps, *Continuum Mechanics and Thermodynamics* (2017) 1–14.
- [37] F. Larche, J. Cahn, The interactions of composition and stress in crystalline solids, *J. Res. Nat. Bur. Stand.* 89 (6) (1984) 467.
- [38] F. Larché, J. Cahn, Thermochemical equilibrium of multiphase solids under stress, *Acta Metallurgica* 26 (10) (1978) 1579–1589.
- [39] K. Miyazaki, A numerical simulation of textural evolution due to ostwald ripening in metamorphic rocks: A case for small amount of volume of dispersed crystals, *Geochimica et cosmochimica acta* 60 (2) (1996) 277–290.
- [40] J. W. Gibbs, On the equilibrium of heterogeneous substances, *American Journal of Science* (96) (1878) 441–458.
- [41] R. F. Sekerka, J. W. Cahn, Solid–liquid equilibrium for non-hydrostatic stress, *Acta materialia* 52 (6) (2004) 1663–1668.
- [42] M. A. Carpenter, A “conditional spinodal” within the peristerite miscibility gap of plagioclase feldspars, *American Mineralogist* 66 (5-6) (1981) 553–560.
- [43] D. H. Lindsley, Some experiments pertaining to the magnetite–ulvöspinel miscibility gap, *American Mineralogist* 66 (7-8) (1981) 759–762.

- [44] T. C. Droubay, C. I. Pearce, E. S. Ilton, M. H. Engelhard, W. Jiang, S. M. Heald, E. Arenholz, V. Shutthanandan, K. M. Rosso, Epitaxial Fe_3O_4 films from magnetite to ulvöspinel by pulsed laser deposition, *Physical Review B* 84 (12) (2011) 125443.
- [45] S. Clavijo, A. Sarmiento, L. Espath, L. Dalcin, A. Cortes, V. Calo, Reactive n -species cahn–hilliard system: A thermodynamically-consistent model for reversible chemical reactions, *Journal of Computational and Applied Mathematics* 350 (2019) 143–154.
- [46] C. M. Elliott, H. Garcke, Diffusional phase transitions in multicomponent systems with a concentration dependent mobility matrix, *Physica D: Nonlinear Phenomena* 109 (3-4) (1997) 242–256.
- [47] B. D. Coleman, W. Noll, The thermodynamics of elastic materials with heat conduction and viscosity, *Archive for rational mechanics and analysis* 13 (1) (1963) 167–178.
- [48] E. Fried, M. Gurtin, Continuum theory of thermally induced phase transitions based on an order parameter, *Physica D: Nonlinear Phenomena* 68 (3-4) (1993) 326–343.
- [49] E. Fried, M. Gurtin, Dynamic solid-solid transitions with phase characterized by an order parameter, *Physica D: Nonlinear Phenomena* 72 (4) (1994) 287–308.
- [50] M. E. Gurtin, Generalized ginzburg-landau and cahn-hilliard equations based on a microforce balance, *Physica D: Nonlinear Phenomena* 92 (3-4) (1996) 178–192.
- [51] M. E. Gurtin, A. S. Vargas, On the classical theory of reacting fluid mixtures, *Archive for Rational Mechanics and Analysis* 43 (3) (1971) 179–197.
- [52] S. M. Wise, J. S. Lowengrub, H. B. Frieboes, V. Cristini, Three-dimensional multispecies nonlinear tumor growth—i: model and numerical method, *Journal of theoretical biology* 253 (3) (2008) 524–543.
- [53] H. Garcke, K. F. Lam, E. Sitka, V. Styles, A cahn-hilliard-darcy model for tumour growth with chemotaxis and active transport, *Mathematical Models and Methods in Applied Sciences* 26 (06) (2016) 1095–1148.
- [54] P. Colli, G. Gilardi, E. Rocca, J. Sprekels, Optimal distributed control of a diffuse interface model of tumor growth, *Nonlinearity* 30 (6) (2017) 2518.

- [55] X. Fu, L. Cueto-Felgueroso, R. Juanes, Thermodynamic coarsening arrested by viscous fingering in partially miscible binary mixtures, *Physical Review E* 94 (3) (2016) 033111.
- [56] M. Honjo, Y. Saito, Numerical simulation of phase separation in Fe-Cr binary and Fe-Cr-Mo ternary alloys with use of the Cahn-Hilliard equation, *ISIJ international* 40 (9) (2000) 914–919.
- [57] A. Bertozzi, S. Esedoğlu, A. Gillette, Analysis of a two-scale cahn–hilliard model for binary image inpainting, *Multiscale Modeling & Simulation* 6 (3) (2007) 913–936.
- [58] F. U. Hartl, M. Hayer-Hartl, Molecular chaperones in the cytosol: from nascent chain to folded protein, *Science* 295 (5561) (2002) 1852–1858.
- [59] W. A. Deer, *Rock-forming minerals*, Geological Society of London, 2011.
- [60] H. Emmerich, *The diffuse interface approach in materials science: thermodynamic concepts and applications of phase-field models*, Vol. 73, Springer Science & Business Media, 2003.
- [61] T. Kimura, Y. Tomioka, R. Kumai, Y. Okimoto, Y. Tokura, Diffuse phase transition and phase separation in Cr-doped Nd^{1/2}Ca^{1/2}MnO₃: A relaxor ferromagnet, *Physical review letters* 83 (19) (1999) 3940.
- [62] B. Stinner, B. Nestler, H. Garcke, A diffuse interface model for alloys with multiple components and phases, *SIAM Journal on Applied Mathematics* 64 (3) (2004) 775–799.
- [63] P. Galenko, D. Jou, Diffuse-interface model for rapid phase transformations in nonequilibrium systems, *Physical Review E* 71 (4) (2005) 046125.
- [64] A. Lamorgese, R. Mauri, Diffuse-interface modeling of liquid-vapor phase separation in a van der Waals fluid, *Physics of Fluids* 21 (4) (2009) 044107.
- [65] J. Morral, J. Cahn, Spinodal decomposition in ternary systems, *Acta metallurgica* 19 (10) (1971) 1037–1045.
- [66] D. De Fontaine, An analysis of clustering and ordering in multicomponent solid solutions—i. stability criteria, *Journal of Physics and Chemistry of Solids* 33 (2) (1972) 297–310.

- [67] S. Maier-Paape, B. Stoth, T. Wanner, Spinodal decomposition for multi-component cahn–hilliard systems, *Journal of Statistical Physics* 98 (3-4) (2000) 871–896.
- [68] J. Hoyt, Spinodal decomposition in ternary alloys, *Acta metallurgica* 37 (9) (1989) 2489–2497.
- [69] J. F. Blowey, M. Copetti, C. M. Elliott, Numerical analysis of a model for phase separation of a multicomponent alloy, *IMA Journal of Numerical Analysis* 16 (1) (1996) 111–139.
- [70] P. Boyanova, M. Neytcheva, Efficient numerical solution of discrete multi-component cahn–hilliard systems, *Computers & Mathematics with Applications* 67 (1) (2014) 106–121.
- [71] M. Conti, S. Gatti, A. Miranville, Multi-component cahn–hilliard systems with dynamic boundary conditions, *Nonlinear Analysis: Real World Applications* 25 (2015) 137–166.
- [72] A. Miranville, G. Schimperna, *Generalized Cahn-Hilliard equations for multicomponent alloys*, Université de Poitiers, 2005.
- [73] A. Miranville, Consistent models of cahn–hilliard–gurtin equations with neumann boundary conditions, *Physica D: Nonlinear Phenomena* 158 (1) (2001) 233–257.
- [74] A. Bonfoh, A. Miranville, On cahn–hilliard–gurtin equations, *Nonlinear Analysis: Theory, Methods & Applications* 47 (5) (2001) 3455–3466.
- [75] L. Cherfils, A. Miranville, S. Zelik, The cahn–hilliard equation with logarithmic potentials, *Milan Journal of Mathematics* 79 (2) (2011) 561–596.
- [76] V. Cimmelli, A. Sellitto, V. Triani, A generalized Coleman–Noll procedure for the exploitation of the entropy principle, *Proceedings of the Royal Society A: Mathematical, Physical and Engineering Sciences* 466 (2115) (2009) 911–925.
- [77] M. E. Gurtin, On a nonequilibrium thermodynamics of capillarity and phase, *Quarterly of applied mathematics* 47 (1) (1989) 129–145.
- [78] R. M. Bowen, On the stoichiometry of chemically reacting materials, *Archive for Rational Mechanics and Analysis* 29 (2) (1968) 114–124.

- [79] J. Ganguly, Thermodynamic modelling of solid solutions, *EMU Notes in Mineralogy* 3 (3) (2001) 37–69.
- [80] E. Guggenheim, The theoretical basis of Raoult's law, *Transactions of the Faraday Society* 33 (1937) 151–156.
- [81] D. J. Goss, R. H. Petrucci, *General Chemistry Principles & Modern Applications*, Petrucci, Harwood, Herring, Madura: Study Guide, Pearson/Prentice Hall, 2007.
- [82] B. C. Eu, M. Al-Ghoul, *Chemical Thermodynamics: With Examples for Nonequilibrium Processes*, World Scientific, 2010.
- [83] G. N. Lewis, Outlines of a new system of thermodynamic chemistry, in: *Proceedings of the American Academy of Arts and Sciences*, Vol. 43, JSTOR, 1907, pp. 259–293.
- [84] I. Barclay, J. Butler, The entropy of solution, *Transactions of the Faraday Society* 34 (1938) 1445–1454.
- [85] M. Gurtin, *Configurational forces as basic concepts of continuum physics*, Vol. 137, Springer Science & Business Media, 2008.
- [86] E. Fried, On the relationship between supplemental balances in two theories for pure interface motion, *SIAM Journal on Applied Mathematics* 66 (4) (2006) 1130–1149.
- [87] V. Blickle, T. Speck, C. Lutz, U. Seifert, C. Bechinger, Einstein relation generalized to nonequilibrium, *Physical review letters* 98 (21) (2007) 210601.
- [88] A. Einstein, Über die von der molekularkinetischen theorie der wärme geforderte bewegung von in ruhenden flüssigkeiten suspendierten teilchen, *Annalen der physik* 322 (8) (1905) 549–560.
- [89] H. P. Langtangen, G. K. Pedersen, *Scaling of differential equations*, Springer International Publishing, 2016.
- [90] H. Gómez, V. M. Calo, Y. Bazilevs, T. J. Hughes, Isogeometric analysis of the Cahn–Hilliard phase-field model, *Computer methods in applied mechanics and engineering* 197 (49–50) (2008) 4333–4352.
- [91] J. W. Gibbs, Art. lii.—on the equilibrium of heterogeneous substances, *American Journal of Science and Arts (1820-1879)* 16 (96) (1878) 441.

- [92] P. Leo, J. Lowengrub, H.-J. Jou, A diffuse interface model for microstructural evolution in elastically stressed solids, *Acta materialia* 46 (6) (1998) 2113–2130.
- [93] Z. Cui, F. Gao, J. Qu, A finite deformation stress-dependent chemical potential and its applications to lithium ion batteries, *Journal of the Mechanics and Physics of Solids* 60 (7) (2012) 1280–1295.
- [94] W. Hong, X. Wang, A phase-field model for systems with coupled large deformation and mass transport, *Journal of the Mechanics and Physics of Solids* 61 (6) (2013) 1281–1294.
- [95] Y. Zhao, B.-X. Xu, P. Stein, D. Gross, Phase-field study of electrochemical reactions at exterior and interior interfaces in li-ion battery electrode particles, *Computer Methods in Applied Mechanics and Engineering* 312 (2016) 428–446.
- [96] T. N’guyen, S. Lejeunes, D. Eyheramendy, A. Boukamel, A thermodynamical framework for the thermo-chemo-mechanical couplings in soft materials at finite strain, *Mechanics of Materials* 95 (2016) 158–171.
- [97] S. Zhang, Chemomechanical modeling of lithiation-induced failure in high-volume-change electrode materials for lithium ion batteries, *npj Computational Materials* 3 (1) (2017) 7.
- [98] G. Bucci, Y.-M. Chiang, W. C. Carter, Formulation of the coupled electrochemical–mechanical boundary-value problem, with applications to transport of multiple charged species, *Acta Materialia* 104 (2016) 33–51.
- [99] T. Zohdi, Modeling and simulation of a class of coupled thermo-chemo-mechanical processes in multiphase solids, *Computer methods in applied mechanics and engineering* 193 (6-8) (2004) 679–699.
- [100] H. Garcke, M. Lenz, B. Niethammer, M. Rumpf, U. Weikard, Multiple scales in phase separating systems with elastic misfit, in: *Analysis, Modeling and Simulation of Multiscale Problems*, Springer, 2006, pp. 153–178.
- [101] S. Rudraraju, A. Van der Ven, K. Garikipati, Mechanochemical spinodal decomposition: a phenomenological theory of phase transformations in multi-component, crystalline solids, *npj Computational Materials* 2 (2016) 16012.
- [102] O. Gonzalez, A. M. Stuart, *A First Course in Continuum Mechanics*, Cambridge University Press, 2008.

- [103] L. I. Sedov, *A Course in Continuum Mechanics: Fluids, gases and the generation of thrust*, Vol. 3, Wolters-Noordhoff, 1972.
- [104] V. Cimmelli, A. Sellitto, V. Triani, A generalized coleman-noll procedure for the exploitation of the entropy principle, in: *Proceedings of the Royal Society of London A: mathematical, physical and engineering sciences*, Vol. 466, The Royal Society, 2010, pp. 911–925.
- [105] L. Dalcin, N. Collier, P. Vignal, A. Côrtes, V. M. Calo, Petiga: A framework for high-performance isogeometric analysis, *Computer Methods in Applied Mechanics and Engineering*.
- [106] P. Vignal, L. Dalcin, D. L. Brown, N. Collier, V. M. Calo, An energy-stable convex splitting for the phase-field crystal equation, *Computers & Structures* 158 (2015) 355–368.
- [107] A. M. Côrtes, A. L. Coutinho, L. Dalcin, V. M. Calo, Performance evaluation of block-diagonal preconditioners for the divergence-conforming b-spline discretization of the stokes system, *Journal of Computational Science* 11 (2015) 123–136.
- [108] P. Vignal, A. Sarmiento, A. M. Côrtes, L. Dalcin, V. M. Calo, Coupling navier-stokes and Cahn-Hilliard equations in a two-dimensional annular flow configuration, *Procedia Computer Science* 51 (2015) 934–943.
- [109] A. F. Sarmiento, A. M. Côrtes, D. Garcia, L. Dalcin, N. Collier, V. M. Calo, Petiga-mf: a multi-field high-performance toolbox for structure-preserving b-splines spaces, *Journal of Computational Science* 18 (2017) 117–131.
- [110] L. Espath, A. Sarmiento, P. Vignal, B. Varga, A. Cortes, L. Dalcin, V. Calo, Energy exchange analysis in droplet dynamics via the Navier-Stokes-Cahn-Hilliard model, *Journal of Fluid Mechanics* 797 (2016) 389–430.
- [111] A. M. Côrtes, P. Vignal, A. Sarmiento, D. García, N. Collier, L. Dalcin, V. M. Calo, Solving nonlinear, high-order partial differential equations using a high-performance isogeometric analysis framework, in: *Latin American High Performance Computing Conference*, Springer, 2014, pp. 236–247.
- [112] P. Vignal, L. Dalcin, N. O. Collier, V. M. Calo, Modeling phase-transitions using a high-performance, isogeometric analysis framework, *Procedia Computer Science* 29 (2014) 980–990.

- [113] A. Sarmiento, D. Garcia, L. Dalcin, N. Collier, V. Calo, Micropolar fluids using b-spline divergence conforming spaces, *Procedia Computer Science* 29 (2014) 991–1001.
- [114] L. Espath, A. Sarmiento, L. Dalcin, V. Calo, On the thermodynamics of the Swift-Hohenberg theory, *Continuum Mechanics and Thermodynamics* (2017) 1–11.
- [115] P. Vignal, N. Collier, L. Dalcin, D. Brown, V. Calo, An energy-stable time-integrator for phase-field models, *Computer Methods in Applied Mechanics and Engineering* 316 (2017) 1179–1214.
- [116] L. Dalcin, N. Collier, P. Vignal, A. Cortes, V. Calo, Petiga: A framework for high-performance isogeometric analysis, *Computer Methods in Applied Mechanics and Engineering* 308 (2016) 151–181.
- [117] C. Truesdell, *Rational thermodynamics*, Springer, 1984.
- [118] R. Milke, R. Dohmen, H.-W. Becker, R. Wirth, Growth kinetics of enstatite reaction rims studied on nano-scale, part i: Methodology, microscopic observations and the role of water, *Contributions to Mineralogy and Petrology* 154 (5) (2007) 519–533.
- [119] M. Perez, Gibbs–thomson effects in phase transformations, *Scripta materialia* 52 (8) (2005) 709–712.
- [120] C. A. Johnson, Generalization of the gibbs-thomson equation, *Surface Science* 3 (5) (1965) 429–444.
- [121] F. Almgren, L. Wang, Mathematical existence of crystal growth with gibbs-thomson curvature effects, *The Journal of Geometric Analysis* 10 (1) (2000) 1.
- [122] L. Keller, Mineral growth in metamorphic rocks: relationships between chemical patterns, mineral microstructure and reaction kinetics, in: *AGU Fall Meeting Abstracts*, 2008.
- [123] V. Kitaeva, E. Zharikov, I. Chisty, The properties of crystals with garnet structure, *physica status solidi (a)* 92 (2) (1985) 475–488.

Appendix A

Copyright clearance "Reactive
 n -species Cahn–Hilliard system:
A thermodynamically-consistent
model for reversible chemical
reaction"



Title: Reactive n -species Cahn–Hilliard system: A thermodynamically-consistent model for reversible chemical reactions
Author: S.P. Clavijo, A.F. Sarmiento, L.F.R. Espath, L. Dalcin, A.M.A. Cortes, V.M. Calo
Publication: Journal of Computational and Applied Mathematics
Publisher: Elsevier
Date: April 2019

Logged in as:
 SANTIAGO PENA CLAVIJO
 Account #:
 3001504575
 LOGOUT

© 2018 Elsevier B.V. All rights reserved.

Quick Price Estimate

I would like to... ?

reuse in a thesis/dissertation

I would like to use... ?

full article

Circulation

1

My format is... ?

both print and electronic

I am the author of this Elsevier article... ?

Yes

I will be translating... ?

No

My currency is...

AUD - \$

Quick Price

Click Quick Price

QUICK PRICE CONTINUE

This service provides permission for reuse only. If you do not have a copy of the content, you may be able to purchase a copy using RightsLink as an additional transaction. Simply select 'I would like to....' 'Purchase this content'.

Unclear about [who you are?](#)

Exchange rates under license from [XE.com](#). To request permission for a type of use not listed, please contact [Elsevier](#) Global Rights Department.

Are you the [author](#) of this Elsevier journal article?

Copyright © 2019 [Copyright Clearance Center, Inc.](#) All Rights Reserved. [Privacy statement](#). [Terms and Conditions](#). Comments? We would like to hear from you. E-mail us at customer@copyright.com

Figure A.1 Copyright clearance from Journal of Computational and Applied Mathematics



Title: Reactive n -species Cahn–Hilliard system: A thermodynamically-consistent model for reversible chemical reactions
Author: S. P. Clavijo, A.F. Sarmiento, L.F.R. Espath, L. Dalcin, A.M.A. Cortes, V.M. Calo
Publication: Journal of Computational and Applied Mathematics
Publisher: Elsevier
Date: April 2019
 © 2018 Elsevier B.V. All rights reserved.

Logged in as:
 SANTIAGO PENA CLAVIJO
 Account #:
 3001504575
 LOGOUT

Please note that, as the author of this Elsevier article, you retain the right to include it in a thesis or dissertation, provided it is not published commercially. Permission is not required, but please ensure that you reference the journal as the original source. For more information on this and on your other retained rights, please visit: <https://www.elsevier.com/about/our-business/policies/copyright#Author-rights>

BACK CLOSE WINDOW

Copyright © 2019 Copyright Clearance Center, Inc. All Rights Reserved. [Privacy statement](#). [Terms and Conditions](#).
 Comments? We would like to hear from you. E-mail us at customer-care@copyright.com

Figure A.2 Copyright clearance from Journal of Computational and Applied Mathematics

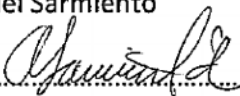
Reactive n-species Cahn–Hilliard system: A thermodynamically-consistent model for reversible chemical reactions Journal of Computational and Applied Mathematics	
Literature review	
Theoretical modelling	x
Numerical modelling	x
Interpretation and discussion	x
Paper drafting or revising	x
Final approval	x

Name: Dr Luis Espath
 Signature
 Date 23/AUG/2019

Figure A.3 Copyright clearance from Dr Luis Espath

Reactive n-species Cahn–Hilliard system: A thermodynamically-consistent model for reversible chemical reactions Journal of Computational and Applied Mathematics	
Literature review	
Theoretical modelling	
Numerical modelling	x
Interpretation and discussion	x
Paper drafting or revising	
Final approval	x

Name: Dr Adel Sarmiento

Signature 

Date 02/09/2019

Figure A.4 Copyright clearance from Dr Adel Sarmiento

Reactive n-species Cahn–Hilliard system: A thermodynamically-consistent model for reversible chemical reactions Journal of Computational and Applied Mathematics	
Literature review	
Theoretical modelling	
Numerical modelling	x
Interpretation and discussion	
Paper drafting or revising	
Final approval	x

Name: Dr Lisandro Dalcin


Signature 

Date 29-AUG-2019

Figure A.5 Copyright clearance from Dr Lisandro Dalcin

Reactive n-species Cahn–Hilliard system: A thermodynamically-consistent model for reversible chemical reactions	
Journal of Computational and Applied Mathematics	
Literature review	
Theoretical modelling	x
Numerical modelling	
Interpretation and discussion	
Paper drafting or revising	
Final approval	x

Name: Dr Adriano Cortes

Signature 

Date Rio de Janeiro, 29 August 2019

Figure A.6 Copyright clearance from Dr Adriano Cortes

Reactive n-species Cahn–Hilliard system: A thermodynamically-consistent model for reversible chemical reactions	
Journal of Computational and Applied Mathematics	
Literature review	
Theoretical modelling	x
Numerical modelling	x
Interpretation and discussion	x
Paper drafting or revising	x
Final approval	x

Name: Prof. Victor Calo

Signature 

Date 28/8/19

Figure A.7 Copyright clearance from Prof Victor Calo